

**Geological Evidence for Tsunamis Generated by
Intraplate Earthquakes in Beppu Bay**

January 2017

Masaki YAMADA

Geological Evidence for Tsunamis Generated by Intraplate Earthquakes in Beppu Bay

A Dissertation Submitted to
the Graduate School of Life and Environmental Sciences,
the University of Tsukuba
in Partial Fulfillment of the Requirements
for the Degree of Doctor of Philosophy in Science
(Doctoral Program in Earth Evolution Sciences)

Masaki YAMADA

Contents

ABSTRACT	iii
List of Figures	v
List of Tables	vi
CHAPTER 1. Introduction	1
1.1. Background	1
1.2. Previous studies	2
1.2.1. Earthquake and tsunami history of Beppu Bay	2
1.2.2. Previous studies on submarine active faults in Beppu Bay	3
1.2.3. Previous studies on tsunami deposits	5
1.3. Aim of this study	6
CHAPTER 2. Study area	12
2.1. Oh-enji marsh, Oita City	12
2.2. Nokinoi lowland, Hiji Town	12
CHAPTER 3. Methods	21
3.1. Field survey and sample collection	21
3.2. Sedimentological analyses	22
3.3. Tephra, geochemical, and diatom analyses	23
3.4. Radiocarbon dating	24
CHAPTER 4. Results	29
4.1. Oh-enji marsh	29
4.1.1. Stratigraphy, tephrochronology, and sedimentary characteristics	29
4.1.2. Magnetic susceptibility and geochemical signatures	32
4.1.3. Diatoms	33
4.1.4. Radiocarbon ages	34
4.2. Nokinoi lowland	68
4.2.1. Stratigraphy, sedimentary characteristics, and radiocarbon ages	68
4.2.2. Magnetic susceptibility and geochemical signatures	69
4.2.3. Diatoms	70
4.2.4. Boulder distribution.....	71

CHAPTER 5. Discussion.....	94
5.1. Depositional environments of the study sites	94
5.1.1. Oh-enji marsh	94
5.1.2. Nokinoi lowland	95
5.2. Identification of prehistoric tsunami deposits	96
5.2.1. Sand layers in the Oh-enji marsh	96
5.2.2. Sand layers in the Nokinoi lowland	98
5.2.3. Boulders in the Nokinoi lowland	99
5.3. Possible source and chronology of prehistporic tsunamis in Beppu Bay	100
5.4. Past faultings estimated from the sedimentary record	102
CHAPTER 6. Conclusion	104
Ackowlegments	105
References	106

ABSTRACT

Onshore sediment cores obtained from coastal lowlands around Beppu Bay were studied to establish a detailed chronology of tsunamigenic intraplate earthquakes that occurred in the bay in prehistoric age. The up to 880 cm sedimentary succession at the Oh-enji marsh, south coast of the bay, is mainly composed of non-marine organic-rich mud and marine silt. Three sand layers are observed in the organic-rich mud, while there is another sand layer D in the marine silt in the other sediment cores. At the Nokinoi lowland located north coast of the bay, there is a 12-cm-thick sand layer in organic-rich mud in the sediment core obtained at 700 m from the shoreline. All sand layers exhibit sharp upper and lower contacts with the surrounding muds, implying that they were deposited by a sudden event. They are characterized by higher magnetic susceptibility associated with higher counts of Ti and Fe, as well as Si, S, K, Ca, Mn, Sr, and Ba than in the overlying and underlying muds. This suggests that the sand grains were supplied from some environments other than freshwater marsh. Moreover, as the brackish-marine and marine diatoms characteristically occur in the sand layers, but not in the surrounding muds, the sand was sourced from sea bottom and/or shore.

The sediments above the K-Ah tephra at the Oh-enji marsh includes at least four probable prehistoric tsunami deposits in 3300–3450 cal. yr BP, 4230–4530 cal. yr BP, 5160–5290 cal. yr BP or later, and 6670–6790 cal. yr BP or later, while the sand layer observed in the Nokinoi lowland was formed before 1880–2000 cal. yr BP. The recurrence intervals of these five prehistoric tsunami deposits is estimated to be approximately 850–1500 years. Given that faulting in Beppu Bay have occurred repeatedly and the tsunami associated with the AD 1596 Keicho Bungo earthquake inundated extensive range of coastal area of the bay, the prehistoric tsunami deposits at the study sites were highly likely deposited by tsunamis associated

with intraplate earthquakes which occurred at the submarine active faults in the bay.

At the Oh-enji marsh, brackish–marine and marine species account for majority of the fossil diatom assemblages in the muddy sand layer above the organic-rich mud (~210 cm deep), implying that the muddy sand was deposited under an inner bay or tidal flat. As far as the facies change from non-marine to marine sediments is not able to be explained by the sea level change, the most likely interpretation is a local subsidence associated with faulting at south of the Oh-enji marsh. This interpretation is also supported by the present elevation of the organic-rich mud occurs between –3 and 0 m.a.s.l., indicating that the Oh-enji marsh has secularly subsided, because non-marine organic-rich mud is generally deposited on a freshwater marsh of more than 0 m.a.s.l. Though the accurate timing and single amount of faulting are not revealed, the Oh-enji marsh must have repeatedly subsided over the long term.

Keywords: Tsunami deposit, Intraplate earthquake, Submarine active fault, Beppu Bay, Grain size, Diatom, Geochemistry, Radiocarbon dating

List of Figures

Fig. 1-1. Location map of the study sites and distribution of active faults in Beppu Bay	7
Fig. 1-2. Reconstructed tsunami heights of the historical tsunamis	8
Fig. 1-3. Location of the representative coring sites by the seabed studies.....	9
Fig. 1-4. Result of the acoustic survey and the location of coring sites.....	10
Fig. 2-1. Aerial photographs and digital elevation model of the Oh-enji marsh.....	14
Fig. 2-2. Locations of studied transect, coring sites, and sampling site of beach sand.....	15
Fig. 2-3. Photograph of the Oh-enji marsh.....	16
Fig. 2-4. Aerial photograph of the Nokinoi lowland showing the studied transects, coring sites, and sampling sites of sand	17
Fig. 2-5. Geologic map around the Nokinoi lowland showing the area of studied boulders.....	18
Fig. 2-6. Digital elevation model of the Nokinoi lowland	19
Fig. 2-7. Photograph of the Nokinoi lowland	20
Fig. 3. Photographs of field survey.....	26
Fig. 4-1. Cross-section of sedimentary columns along the transect A–A' in the Oh-enji marsh.....	36
Fig. 4-2. Photograph and CT image of the sediment core at OEJ-a in the Oh-enji marsh	37
Fig. 4-3. Photograph and CT image of the sediment core at OEJ-b in the Oh-enji marsh.....	40
Fig. 4-4. Photograph and CT image of the sediment core at OEJ-c in the Oh-enji marsh	45
Fig. 4-5. Enlarged photographs of typical layers in the core OEJ-a	50
Fig. 4-6. Enlarged photographs of typical layers in the core OEJ-b.....	51
Fig. 4-7. Enlarged photographs of typical layers in the core OEJ-c	52
Fig. 4-8. Micrographs of volcanic glass shards and orthopyroxene grains of the tephra layers	53
Fig. 4-9. Refractive index of volcanic glass shards and orthopyroxene grains of the tephra layers	54
Fig. 4-10. Grain size distribution of the sand/gravel layers at the Oh-enji marsh.....	55
Fig. 4-11. Vertical variation in grain size distribution of the sand layer D.....	56
Fig. 4-12. Vertical variation in grain size distribution of the sand layer E	57
Fig. 4-13. Magnetic susceptibility and ITRAX data of the core OEJ-b.....	58
Fig. 4-14. Scores and loading of the PCA from 362–367 cm deep in the core OEJ-b.....	59
Fig. 4-15. Fossil diatom assemblages in the core OEJ-b.....	60
Fig. 4-16. Abundance of diatoms in the core OEJ-b.....	61
Fig. 4-17. Micrographs of typical diatoms in the core OEJ-b.....	62
Fig. 4-18. Radiocarbon ages obtained from the cores in the Oh-enji marsh	63

Fig. 4-19. Cross-sections of sedimentary columns along the transect A–A' and B–B' in the Nokinoi lowland	72
Fig. 4-20. Photograph and CT image of the sediment cores obtained from the Nokinoi lowland	73
Fig. 4-21. Enlarged photograph and CT image of the sediments occur at 100–120 cm deep in the core HJ-4	75
Fig. 4-22. Vertical variation in grain size distribution of the sand layer evident in 104–116 cm deep in the core HJ-4	76
Fig. 4-23. Grain size distribution of the sand grains obtained from tidal flat and beach	77
Fig. 4-24. Magnetic susceptibility and ITRAX data of the depth of 101–167 cm in the core HJ-4'	78
Fig. 4-25. Scores and loading of the PCA from 101–167 cm deep in the core HJ-4'	79
Fig. 4-26. Fossil diatom assemblages in the core HJ-4.....	80
Fig. 4-27. Abundance of diatoms in the core HJ-4.....	81
Fig. 4-28. Micrographs of typical diatoms in the core HJ-4.....	82
Fig. 4-29. Locations, sizes, and types of the boulders in the study area	83
Fig. 4-30. Photograph showing boulders at the shore of the Nokinoi lowland.....	84
Fig. 4-31. Photomicrographs of the andesite boulder named HJ-B2.....	85
Fig. 5. Comparison of the age of prehistoric tsunami deposits with the faulting history of the submarine active faults in the bay	103

List of Tables

Table 1. List of major tsunamis that struck the east coast of Kyushu.....	11
Table 3-1. Location, distance from shoreline, length, and sampling method of each core collected in the Oh-enji marsh	27
Table 3-2. Location, distance from shoreline, length, and sampling method of each core collected in the Nokinoi lowland.....	28
Table 4-1. Main mineral and range of refractive index of the volcanic glass shards and orthopyroxene grains of the tephra layers	64
Table 4-2. Mud content, mean grain size, and sorting of the sand/gravel layers and beach sand at the Oh-enji marsh.....	65
Table 4-3. Mineral composition of the sand layers A–E and beach sand at the Oh-enji marsh.....	66

Table 4-4. Radiocarbon ages of leaves, seeds, insect remains, and shell fragments obtained from the cores in the Oh-enji marsh.....	67
Table 4-5. Mud content, mean grain size, and sorting of the sand layer in the core HJ-4, tidal flat sand, and beach sand at the Nokinoi lowland	86
Table 4-6. Mineral composition of the sand layer in the core HJ-4, tidal flat sand, and beach sand at the Nokinoi lowland.....	87
Table 4-7. Radiocarbon ages of leaves and seeds obtained from the cores in Nokinoi lowland.....	88
Table 4-8. Location, sizes, weight, and rock type of boulders.	89

CHAPTER 1. Introduction

1.1. Background

Large tsunamis are typically generated by plate-boundary ruptures at subduction zones (e.g. AD 1707 Hoi megathrust earthquake tsunami; 2004 Indian Ocean tsunami; 2010 Chile tsunami; 2011 Tohoku-oki tsunami), but also by vertical displacements of submarine intraplate fault ruptures. Numerous active faults are developed in the world, and taking adjacent seas in Japan for instance, previous acoustic studies revealed distributions of submarine active faults in such as Wakasa Bay (e.g. Inoue et al., 2014; Sugiyama et al., 2014), Ise Bay (e.g. Iwabuchi, 2000; Okada et al., 2000), Osaka Bay (e.g. Iwabuchi, 2000; Usami, 2002), Suo-nada (e.g. Kumaki et al., 1986; Headquarters for Earthquake Research Promotion (HERP), 2016), and Beppu Bay (e.g. Shimazaki et al., 1986; Yusa et al., 1992). Past fault ruptures are recorded in the sediments of seabeds along the Nosaka fault and Mikata fault zone in Wakasa Bay and Osaka Bay faults, but it is not known whether the fault ruptures were accompanied by tsunamis or not (Iwabuchi, 2000; Inoue et al., 2014; Sugiyama et al., 2014). This is because of limited information about the historic/prehistoric earthquakes.

One of the few examples of tsunamis associated with intraplate earthquakes is the AD 1596 Keicho Bungo tsunami, which occurred in association with an earthquake of $M=6.9$ in Beppu Bay, eastern Kyushu, Japan (Hatori, 1985a; Fig. 1-1 and Table 1). The wave height of the AD 1596 Keicho Bungo tsunami is well documented in several written records (Hatori, 1985a; see detail in subsection 1.2.1). Distribution and faulting history of the submarine active faults have been revealed by acoustic and coring studies in the bay (e.g. Shimazaki et al., 1986; see subsection 1.2.2).

Tsunami-generating earthquakes other than those of subduction-zone earthquakes have repeatedly occurred along North Anatolian Fault in Marmara Sea (e.g. Altinok et al., 1999, 2001; Awata et al., 2001;

Barka et al., 2002), where is the plate boundary between Anatolian and Eurasia plates. The Izmit earthquake ($M_w=7.4$; Altinok et al., 2001), which occurred on August 17, 1999, in Izmit Bay, Turkey, caused right-lateral strike-slip movement on the fault and up to 2.5 m-high tsunami in coastal area of the bay (e.g. Altinok et al., 1999, 2001; Barka et al., 2002).

As the 1999 Izmit earthquake and associated tsunami occurred in recent period with developed seismic observation network, the rupture zone of the earthquake, amount of displacement of the faults, and tsunami height were accurately revealed (e.g. Altinok et al., 1999, 2001; Awata et al., 2001; Barka et al., 2002). However, past intraplate earthquakes and their accompanying tsunamis in Japan remain unclear, since most of them occurred in prehistoric age. Beppu Bay is a suitable study area to unravel tsunami history associated with submarine intraplate earthquakes since there is a wealth of information on the tsunami height of historic earthquake and the rupture age of the submarine active faults.

1.2. Previous studies

1.2.1. Earthquake and tsunami history of Beppu Bay

The Keicho Bungo earthquake occurred on September 4th, 1596, and associated tsunami caused more than 700 casualties (Hatori, 1985a). These earthquake and tsunami are well documented in several historical records such as "A report by Luis Frois", "The Shibayama Kanbei Diary", "The Genyo Diary", and "The Kitsuki local history" (Hatori, 1985a). The water heights and inundation areas of the AD 1596 tsunami are reconstructed based on damage situations of temples, shrines, and other constructions that are described in historical records along with elevations of the buildings. Distributions of destroyed temples indicate that the tsunami height was about 4–5.5 m at Oita City on south coast of the bay. At Nata and Saganoseki, on north and south entrances of the bay, the shrines at approximately 6- and 4-m-high were destroyed by the

tsunami, suggesting that the tsunami heights reached 6–8 m (Fig. 1-2a; Hatori, 1985a). According to a local lore and historical documents, the Uryujima Island, where more than 1000 settlements and 5000 people located, disappeared after the tsunami (Hatori, 1985a). The island is considered as a sandbar island that had existed at 400–500 m offshore from Oita City (Fig. 1-2a; Hatori, 1985a). There was another intraplate earthquake in northern Shikoku Island east of Beppu Bay that occurred three days before the AD 1596 Keicho Bungo earthquake, but there is no description of tsunamis in ancient documents (Nakanishi, 2002).

The coast of the bay had been affected by tsunamis generated by plate boundary earthquakes along Nankai Trough and Hyuga-nada as well as the intraplate earthquake in the bay (Fig. 1-1 and Table 1). Tsunami height of the AD 1707 Hiei megathrust earthquake ($M_w \geq 9$; Hyodo and Hori, 2013), that is believed as one of the largest earthquakes along the Nankai Trough, was up to 10 m at Pacific coasts of Shikoku Island (Hatori, 1988), but it was less than 3 m in Beppu Bay (Fig. 1-2b; Hatori, 1985b). Magnitude 7 class earthquakes have repeatedly occurred at southeast of Kyushu named Hyuga-nada, but there was little or no influence on the coastal area of Beppu Bay (Table 1-1; Hatori, 1985b). It is noteworthy that the heights of tsunamis generated by plate-boundary earthquakes along Nankai Trough and Hyuga-nada did not exceed 3 m within the bay, whereas up to 8-m-high tsunami was recorded by the AD 1596 Keicho Bungo earthquake (Fig. 1-2 and Table 1; Hatori, 1985a, 1985b, 1988). This means that tsunamis associated with Nankai Trough and Hyuga-nada earthquakes did not cause significant damages on coastal area around Beppu Bay in historic ages.

1.2.2. Previous studies on submarine active faults in Beppu Bay

Beppu Bay, located in central Kyushu in southwest Japan, is placed at westernmost part of Median Tectonic Line (MTL) that is an arc-bisecting dextral fault greater than 1000 km in length (Fig. 1-1). This

fault is associated with a subduction along the Nankai Trough that conveys the Philippine Sea Plate beneath Shikoku and Kyushu at an average rate of 4–5 cm/yr (e.g. Seno et al., 1993; Loveless and Meade, 2010). The formation process of the bay is divided into following two stages: the older stage, 5–1.5 Ma, was dominated by a northward-inclined half-graben, while pull-apart stress due to the right-stepping of the MTL developed during the younger stage from 1.5 Ma to the present, particularly from 0.7 Ma to the present (Itoh et al., 1998; Itoh et al., 2014). As a result of these, active faults had been densely distributed within and around the bay. The faults belong to the Beppu Bay-Hijiya fault zone which is about 76-km-long west-east directed fault zone distributed from easternmost part of the bay (east part; Fig. 1-1) to internal regions of Oita Prefecture (west part).

Acoustic and coring surveys conducted in Beppu Bay revealed that east-west directed normal faults (west part; red line in Fig. 1-3) and right-lateral strike-slip faults (east part; blue line in Fig. 1-3) are distributed in the bay and suggest that the faults have been active five times in the past 7000 years (Fig. 1-3b and c; e.g. Shimazaki et al., 1986, 2000; Okamura et al., 1992; Yusa et al., 1992; Nakata and Shimazaki, 1993; Oita Prefecture, 2000, 2001, 2002; Headquarters for Earthquake Research Promotion (HERP), 2005; National Institute of Advanced Industrial Science and Technology (AIST), 2012). It is known that the foot wall which is relatively uplifted by earthquakes is mainly north side in the northern normal faults, while south side had been uplifted by past faulting at the southern right-lateral strike-slip faults (Figs. 1-3 and 1-4; Yusa et al., 1992; Shimazaki et al., 2000; Oita Prefecture, 2002; HERP, 2005; AIST, 2012). Average displacement rate is about 3 m/1000 yr and an average of single vertical displacement is estimated to be more than 4 m (Nakata and Shimazaki, 1993; Oita Prefecture, 2002; HERP, 2005).

In recent years, sediment cores were obtained from the deepest part of the bay to establish the stratigraphy and to identify turbidites formed by earthquake, tsunami, and flood events (BP09-3 in Fig. 1-

3a; Kuwae et al., 2013; Yamada et al., 2016b). These studies suggest that four turbidites with thicknesses of 11.0–50.8 cm among 16 sand/mud beds were most likely deposited by past earthquakes. According to the wiggle-matching-based ages by Kuwae et al. (2013) and Yamada et al. (2016b), their depositional ages were dated to 344, 617, 1685, and 1893 cal. yr BP. Though it is not certain whether the turbidite beds deposited in association with earthquakes or not, one of their ages well overlaps with the AD 1596 Keicho Bungo earthquake (Kuwae et al., 2013; Yamada et al., 2016b).

1.2.3. Previous studies on tsunami deposits

Tsunami deposit is generally defined as widely deposited sediments by tsunami inundation. Onshore tsunami deposits, that are composed of various grain size ranging from mud to boulder, have been preserved for a long time if they were formed under calm depositional environments such as coastal lakes, lagoons, marshes, and inter-ridge swales of strand plains. A sandy tsunami deposit has especially been used for paleotsunami researches (e.g. Nanayama et al., 2003; Sawai et al., 2004; Cisternas et al., 2005; Jankaew et al., 2008; Fujino et al., 2009; Goff et al., 2012; Sawai, 2012) since it is more easily identified from geologic strata than mud and gravel. Nonetheless, it is not easy to distinguish paleotsunami deposits from the other event deposits such as storm deposits (e.g. Goff et al., 2004; Morton et al., 2007) and flood deposits (e.g. Matsumoto et al., 2016; Yamada et al., 2016a) because of their similarities in sedimentary characteristics. Therefore, paleotsunami deposits should be identified on the basis of the sedimentological features such as thickness distribution, grain-size distribution, sedimentary structures (e.g. Minoura and Nakata, 1994; Nanayama et al., 2007; Sawai et al., 2009; Fujino et al., 2010), but also by diatom analysis (e.g. Sawai et al., 2004, 2008; Nanayama et al., 2003, 2007) and geochemical analysis (e.g. Minoura and Nakata, 1994; Minoura et al., 2001; Chagué-Goff et al., 2012, 2016, 2017).

1.3. Aim of this study

Previous studies suggest that the active faults of the bay have been active in the last 7000 years (e.g. Oita Prefecture, 2002; HERP, 2005). However, the accurate timing of these fault ruptures is yet to be determined. This is largely because of the technological limitations of the fault research as well as the lack of ancient documents of earthquakes and tsunamis before AD 1596. In fault researches, the ages of past faulting are estimated by the difference in thickness between the two reflecting layers evident in sediment cores collected at either side of a fault (e.g. Shimazaki et al., 1986). Therefore, they have a margin of error of plus or minus 1000 years in some cases, and there is a possibility that a single displacement of sediments includes more than two activities. In this study, tsunami history is revealed by geological records preserved in coastal lowlands, and the results of this study will probably contribute to gain better understandings about faulting pattern of the submarine active faults in Beppu Bay as well as in the other sites.

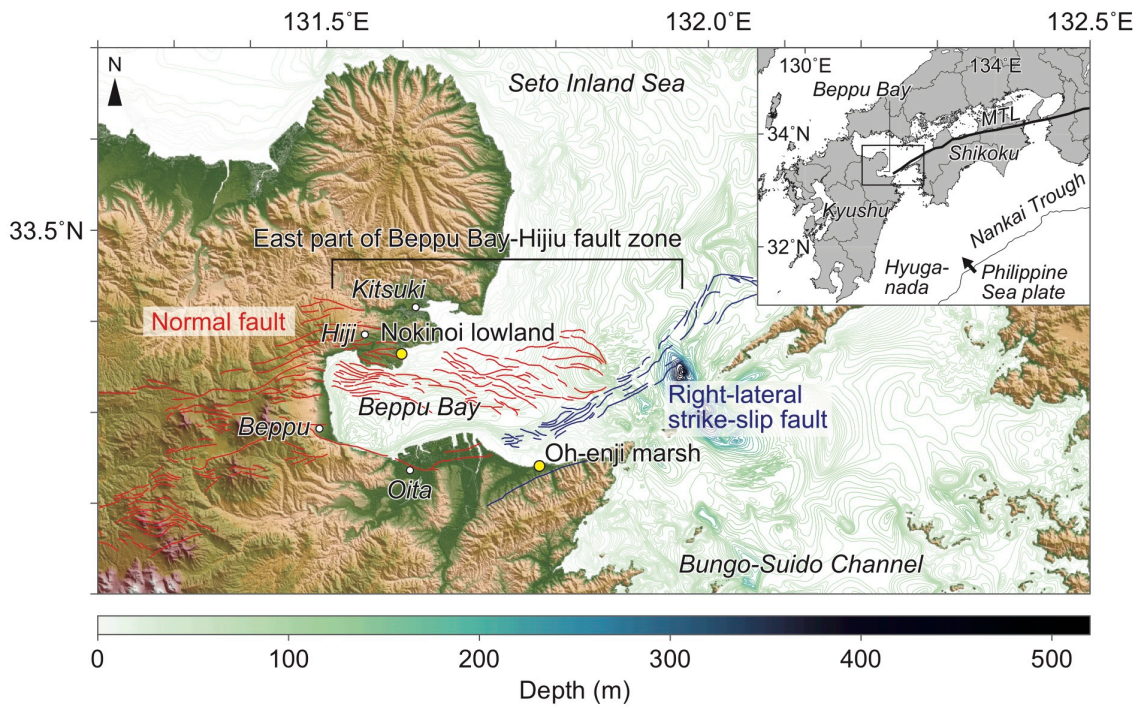
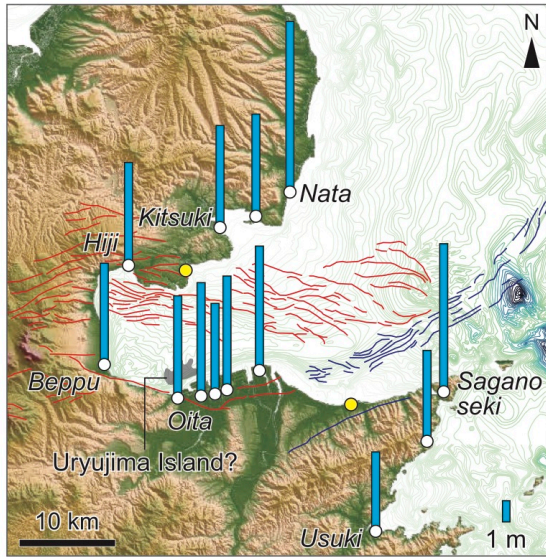


Fig. 1-1. Location map of the study sites and distribution of active faults in Beppu Bay (AIST, 2012). Digital elevation model of continental area and bathymetric data were provided by the Geospatial Information Authority of Japan (2015a) and the Japan Hydrographic Association (2015), respectively.

a AD 1596 Keicho Bungo earthquake



b AD 1707 Hiei earthquake

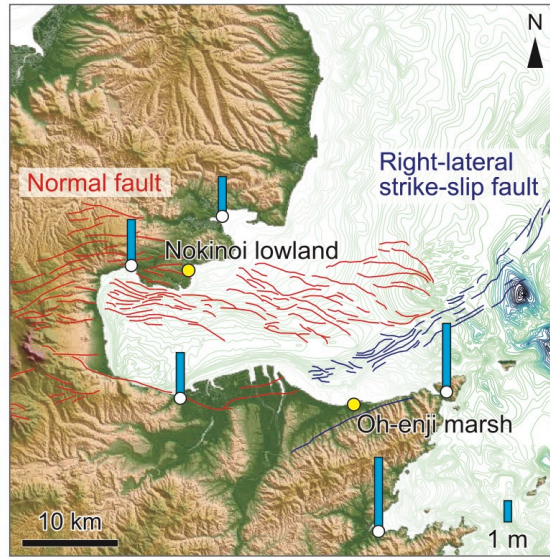


Fig. 1-2. Reconstructed tsunami heights of the historical tsunamis generated by (a) AD 1596 Keicho Bungo earthquake (Hatori, 1985a) and (b) AD 1707 Hiei megathrust earthquake (Hatori, 1985b).

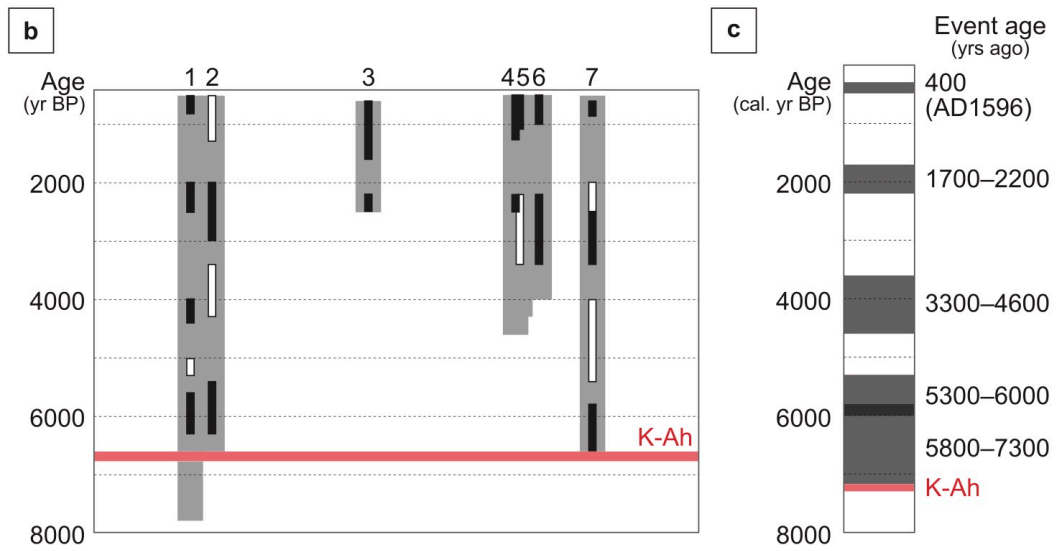
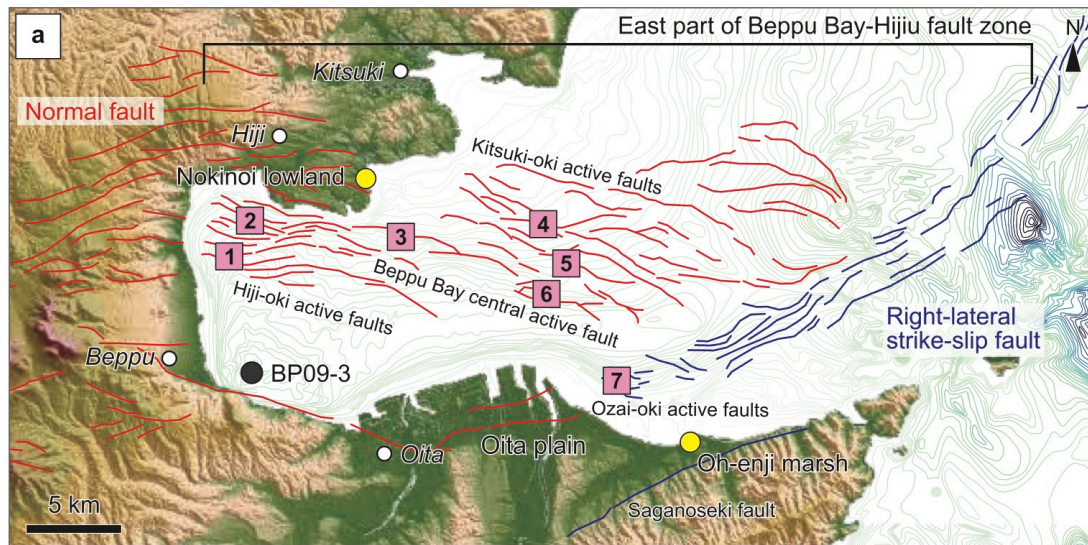


Fig. 1-3. (a) Location of the representative coring sites by the seabed studies (1: Kamegawa-oki fault (west), 2: Toyooka-oki fault, 3: Beppu Bay central fault (west), 4: Kitsuki-oki fault (north), 5: Kitsuki-oki fault (south), 6: Beppu Bay central fault (east), 7: Ozai-oki fault; Oita Prefecture, 2000, 2001, 2002; HERP, 2005). The seabed results in Fig. 5-2 is based on the sediment core collected at BP09-3 (Kuwae et al., 2013 and Yamada et al., 2016b). (b) The active history of the submarine active faults in Beppu Bay. Core length at each site (gray) with assumed event ages (black) (modified after Oita Prefecture 2000, 2001, 2002). (c) Calibrated event ages (HERP, 2005).

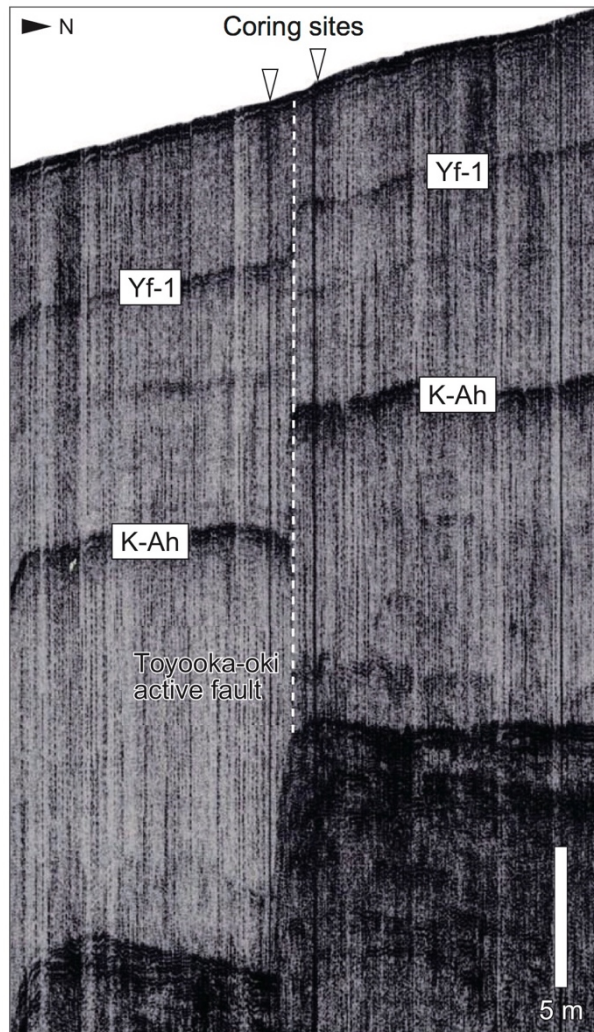


Fig. 1-4. Result of the acoustic survey at the Toyooka-oki active fault and the location of coring sites (No. 2 in Fig. 1-3; modified after Oita Prefecture, 2002). Two tephra layers, Yf-1 and K-Ah, are short of Yufudake-1 tephra (2.2 ka; Fujisawa et al., 2001) and Kikai-Akahoya tephra (7170–7300 cal. yr. BP; Smith et al., 2013).

Table 1. List of major tsunamis that struck the east coast of Kyushu (modified after Hatori 1985a, b).

Year	Japanese era	Source	Magnitude	Maximum tsunami height around Beppu Bay (m)
1596	Keicho	Beppu Bay	6.9	8
1605	Keicho	Nankai Trough	7.9	No data
1662	Kanbun	Hyuga-nada	7.6	0
1707	Hoei	Nankai Trough	8.4	3
1769	Meiwa	Hyuga-nada	7.4	2.5*
1854	Ansei	Nankai Trough	8.4	2.5*
1941	Showa	Hyuga-nada	7.4	0.5*
1946	Showa	Nankai Trough	8.1	1
1968	Showa	Hyuga-nada	7.5	1.5*

*Reconstructed tsunami height at Usuki located south of Beppu Bay (see Fig. 1-2).

CHAPTER 2. Study area

2.1. Oh-enji marsh, Oita City

The Oh-enji marsh, at the easternmost part of Oita plain (Figs. 1-1 and 2-1), is protected from the sea by sandy beach and Holocene beach ridge deposits (ar in Fig. 2-2). The approximately 100 m wide marsh is surrounded by the Early Pleistocene (Gelasian and Calabrian) Higashiwasada and Handa formations of the Sekinan Group (Sn) at the seaward side and by the Middle Pleistocene Upper Formation of the Oita Group (Oi) at the landward side (Fig. 2-2; Miyazaki and Yoshioka, 1994). The Sekinan Group consists of volcanic silt and sand layers intercalating gravel and pumice tuff layers. The Upper Formation of the Oita Group is mainly composed of non-marine angular gravel and volcanic silt layers, but a marine silt layer is evident in the upper part of this formation. Late Pleistocene coast terrace deposits (tm in Fig. 2-2), which overlie Sekinan and Oita Groups, are composed of rounded granules and pebbles with well sorted sand matrix (Miyazaki and Yoshioka, 1994).

The present elevation is approximately less than 3 m throughout the marsh, and a higher sandbar is located in front of the marsh (Fig. 2-1c). Reed grass grow naturally in a wide area in the present years although the marsh had been used for paddy fields in the past. A seaward side of the marsh had been excavated to make an artificial pond as a part of construction of a natural park, but most part of the marsh has been held in a half-natural state (Figs. 2-2 and 2-3). The water height of the AD 1596 Keicho Bungo tsunami is estimated to be about 5 m around this site (Hatori, 1985a).

2.2. Nokinoi lowland, Hiji Town

The Nokinoi lowland, Hiji Town, at the north coast of the bay (Fig. 2-4), is surrounded by non-marine sediments in Terukawa Formation and Middle Pleistocene pyroclastic flow deposits (Fig. 2-5; Ishizuka et

al., 2005). The non-marine sediments in Terukawa Formation (Tk) are composed of a sand and gravel layer as well as a reworked pyroclastic flow deposits and a pumiceous layer. The Yufugawa Pyroclastic Flow Deposits (Yu) are partly evident lower horizon of the Terukawa Formation around the lowland. The Akisada Pyroclastic Flow Deposits (As), that overlie the Terukawa Formation or Yufugawa Pyroclastic Flow Deposits, are composed of andesite lapilli tuff with volcanic rock. These deposits are overlain by the Hiji Pyroclastic Flow Deposits (Hj) which consist of fall pyroclastic deposits and pyroclastic surge deposits in addition to the pyroclastic flow deposits (Fig. 2-5; Ishizuka et al., 2005).

The present elevation of the lowland is approximately less than 10 m and get higher toward the inland (Fig. 2-6). Although the area from the shoreline to 250 m inland in the lowland have been artificially altered, a sandbar probably existed in front of the lowland before the human alternation. The area more than 250 m from the shoreline is used for paddy fields along three narrow valleys (Figs. 2-4 and 2-7). A small stream runs at the northern part of the lowland, and the 30–100 m wide valleys behind of a road extend further inland (Fig. 2-4). The coast of this study site is protected by stone steps, but there is a sandy beach outside of them. A position of the low tide line is about at most 200 m away from the high tide line, and broad tidal flat spreads in front of the sandy beach (Fig. 2-4). Although there is no record about a water height of the AD 1596 Keicho Bungo tsunami around this site, the water height is estimated to be 4–5 m at the coast of Kitsuki City located 5 km north-east from this site (Fig. 1-2a; Hatori, 1985a).



Fig. 2-1. (a) Aerial photograph of the Oh-enji marsh in 1947 (Geospatial Information Authority of Japan, 1947). Blue dots in the map at the upper right show the locations of preliminary study sites. (b) Aerial photograph of the Oh-enji marsh in 2007 (Geospatial Information Authority of Japan, 2007). (c) Digital elevation model of the Oh-enji marsh (Geospatial Information Authority of Japan, 2015a).

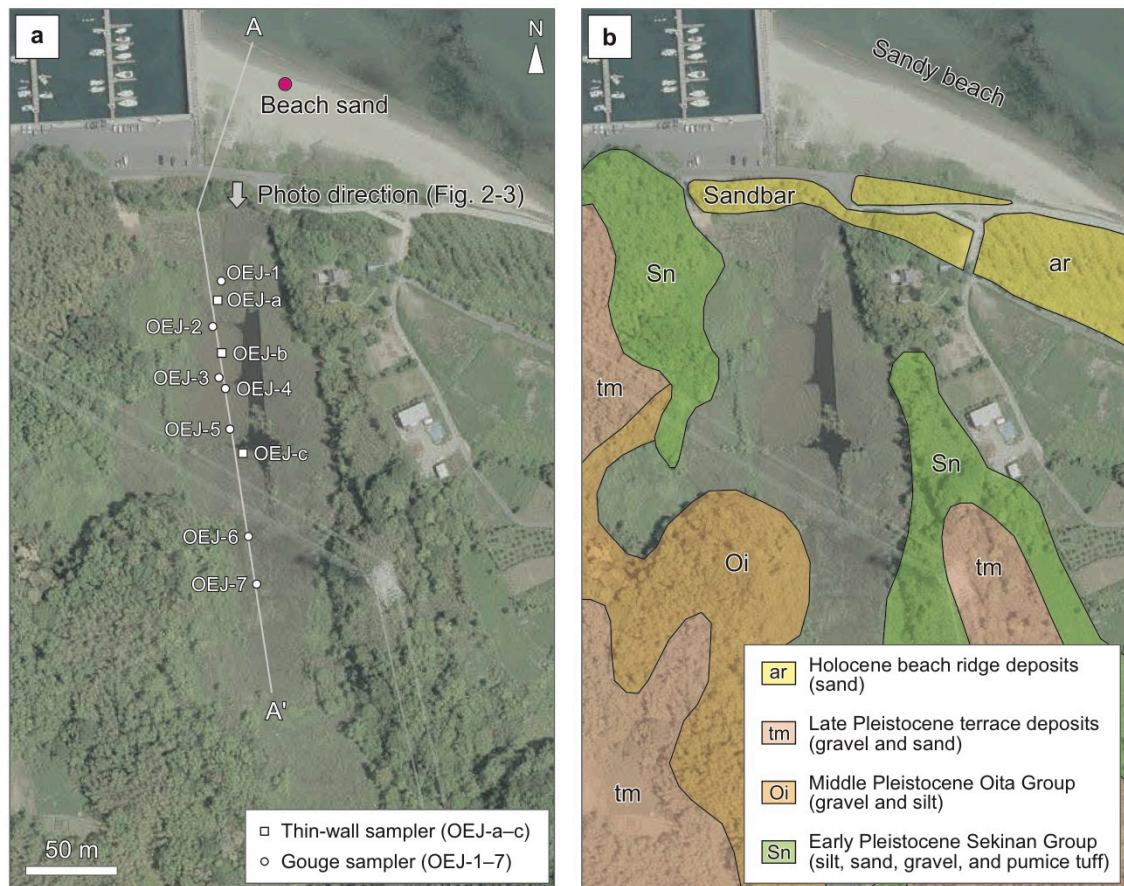


Fig. 2-2. (a) Locations of studied transect, coring sites, and sampling site of beach sand. Aerial photograph of the Oh-enji marsh was provided by the Geospatial Information Authority of Japan (2007). (b) Geologic map around the Oh-enji marsh (Miyazaki and Yoshioka, 1994).



Fig. 2-3. Photograph of the Oh-enji marsh. The photo direction is shown in Fig. 2-2.

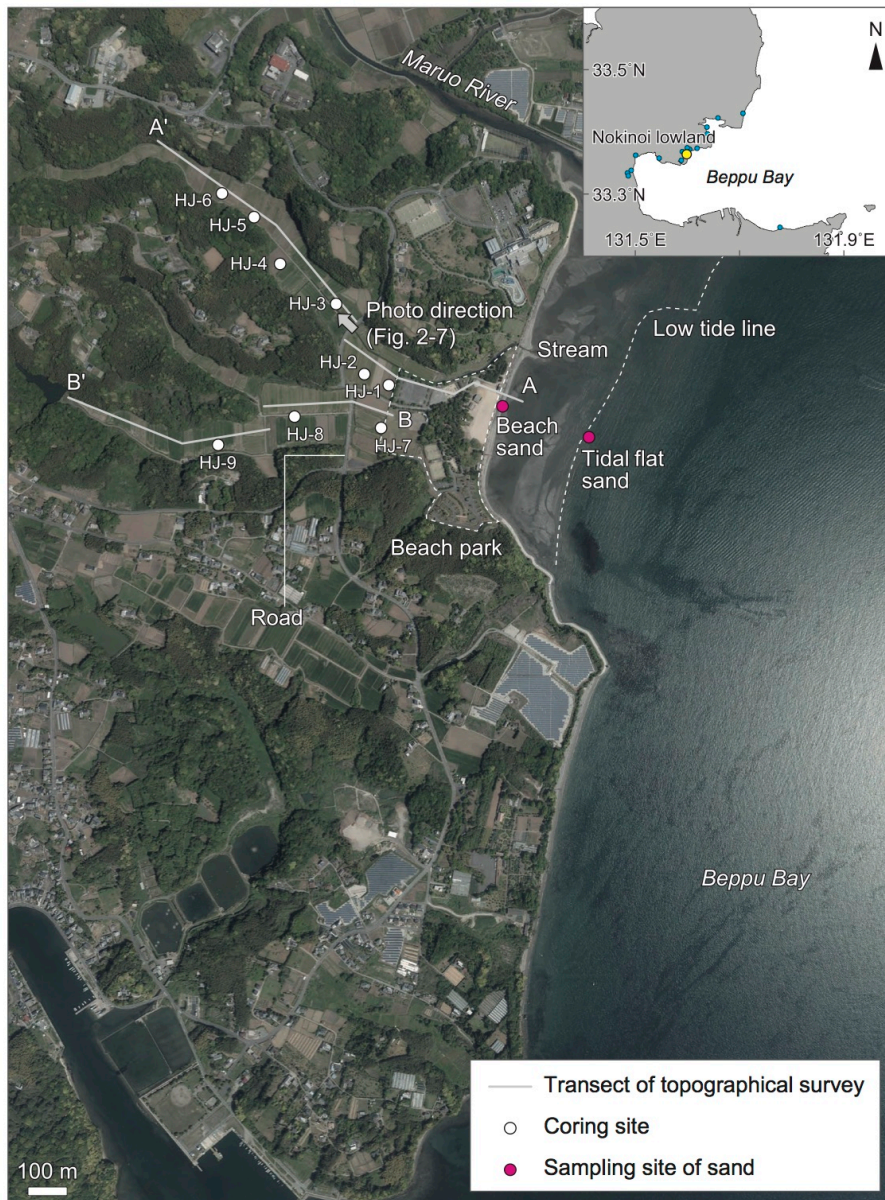


Fig. 2-4. Aerial photograph of the Nokinoi lowland, Hiji Town (provided by Geospatial Information Authority of Japan, 2015b) showing the studied transects, coring sites, and sampling sites of sand. Blue dots in the map at the upper right show the locations of preliminary study sites.

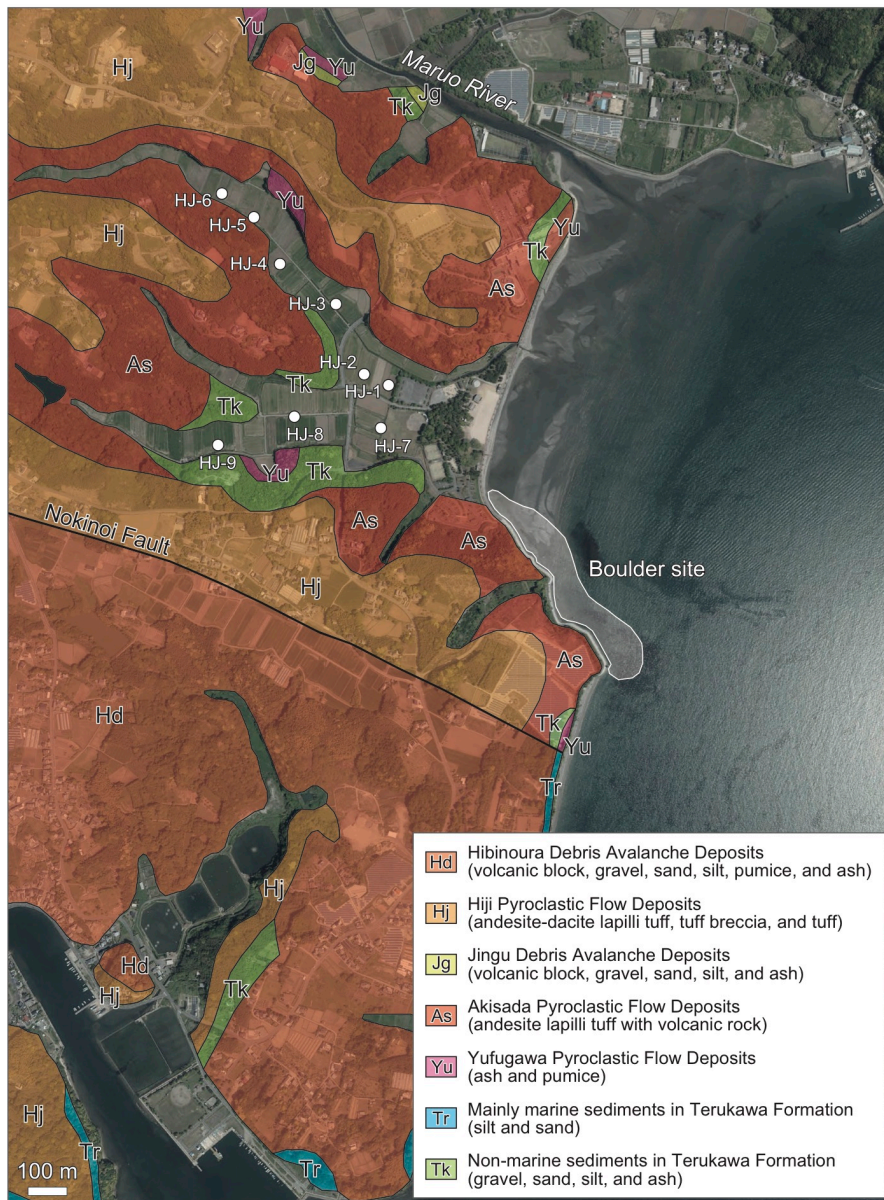


Fig. 2-5. Geologic map around the Nokinoi lowland (Ishizuka et al., 2005) showing the area of studied boulders.



Fig. 2-6. Digital elevation model of the Nokinoi lowland (Geospatial Information Authority of Japan, 2015a).



Fig. 2-7. Photograph of the Nokinoi lowland. The photo direction is shown in Fig. 2-4.

CHAPTER 3. Methods

3.1. Field survey and sample collection

The first thing that I did is to search out coastal lowlands and ponds that suitable for a paleotsunami study by using the Google Earth satellite image, and then exploratory field surveys had been conducted all over the coastal area of the bay since October 2014 (Figs. 2-1a and 2-4). I tried to collect sediment cores at more than 10 sites and described sedimentary facies, and finally, I selected the Oh-enji marsh and the Nokinoi lowland for this study since some sand layers existed in freshwater organic-rich mud layers (Figs. 2-1, 2-2, and 2-4).

Sediment cores were collected at ten sites in the Oh-enji marsh (OEJ-a–c and OEJ-1–7 in Fig. 2-2a) and at nine sites in the Nokinoi lowland (HJ-1–9 in Fig. 2-4). At the Oh-enji marsh, sediment cores were obtained using a mechanical thin-wall sampler (75 mm diameter) at the OEJ-a–c and a gouge sampler (30 mm diameter) at the OEJ-1–7 (Fig. 3a, b, and Table 3-1) along the shore-perpendicular transect (A–A' in Fig. 2-2). Sediment cores at the OEJ-a–c were collected in steps of 1 m deep and then were cut into halves for analyses and archival purpose. Geoslicers of 2 and 3 m long were used at the HJ-3, 4, 5, 8, and 9 to obtain sediment cores along two transects at the Nokinoi lowland (A–A' and B–B' in Fig. 2-4), while the other sediment cores were collected using the gouge sampler (Table 3-2). A sediment core HJ-4' was collected for geochemical analysis at the same location as the HJ-4. The geoslicer consists of a 120 mm wide sample tray and a shutter plate (Fig. 3c, d; Nakata and Shimazaki, 1997; Takada et al., 2002). The sediment cores obtained by a geoslicer were moved from a tray to 20 cm long plastic cases after description and photography to bring them back.

A hand-held Garmin GPS was used to record the positions of each coring site. A topographic profile along each transect was measured using an ProMark 100 global navigation satellite system receiver

(Ashtech, Santa Clara, USA) that records the latitude, longitude, and elevation with a measurement error of 5 mm + 1 ppm following static post-processing and 12 mm + 2 ppm with kinematic post-processing (Fig. 3e). The positions of boulders defined as clasts with long axes greater than 1 m were also recorded by a hand-held GPS at the shore of the Nokinoi lowland. Rounded boulders were approximated as rectangular blocks, and their three dimensions were determined. In order to measure density of the boulders and to make a thin section, a hand specimen was taken from a typical boulder (HJ-B2).

3.2. Sedimentological analyses

After the description of sedimentary facies by bare-eye observations, a computed tomography (CT) images of some sediment cores (OEJ-a–c, HJ-3, 4, 5, 8, and 9) were taken to verify sedimentary structures and extremely thin sand layers which is not observed by bare-eye, using the LightSpeed Ultra16 (GE Healthcare UK Ltd., Buckinghamshire, England) at the Kochi Core Center. Magnetic susceptibilities of the whole core at OEJ-b and HJ-4 were measured to check a relative change of magnetic minerals among each layer, by use of the MSCL-S (Geotek Ltd., Northamptonshire, England) at the Kochi Core Center.

In order to compare grain size distribution of each sand and/or gravel deposit, tidal flat sand, and beach sand, the grain size ranging from 0.063 mm to 3 cm in diameter was measured using a Retch Technology CAMSIZER (Haan, Germany), and then the grain size (ϕ) and sorting were calculated based on Folk (1966). Some thicker sand and/or gravel layers were collected in 1 cm (651–655 cm deep in the core OEJ-b and 104–116 cm deep in the core HJ-4) and 2 cm (420–440 cm deep in the core OEJ-a, 571–585 cm and 721–729 cm deeps in the core OEJ-c) vertical intervals to examine changes in the grain size distribution. Prior to analysis, the organic matter was removed using a 30% hydrogen peroxide solution for 24 hours, and each sample was then dried in a 60°C oven for 24 hours. Mud content (%) of each muddy sand layer

(420–440 cm deep in the core OEJ-a, 571–585 cm deep in the core OEJ-c, and 104–116 cm deep in the core HJ-4) was calculated by measuring the weights of total and sand amounts. A total of 100 grains of each sample taken from 257–259 cm, 315–316 cm, 363–366 cm, and 651–655 cm deeps in the core OEJ-b, 571–585 cm deep in the core OEJ-c, beach sand at the Oh-enji marsh, 104–116 cm deep in the core HJ-4, and tidal flat and beach sand at the Nokinoi lowland were divided into quartz, feldspar, pyroxene, hornblende, magnetite, rock fragment, and volcanic glass under a stereoscopic microscope.

The weight of each boulder was estimated from its volume and wet density. The wet density of boulder was measured in a water-filled measuring cylinder after it was soaked in water for 30 minutes.

3.3. Tephra, geochemical, and diatom analyses

Refractive index measurements of volcanic glass shards and orthopyroxenes for tephra layers were conducted on 0.063–0.125 mm sized particles with a Refractive Index Measuring System (RIMS) at Kyoto Fission-Track Co. Ltd. (Yokoyama et al., 1986; Danhara et al., 1992; Kamata et al., 1994). Up to 71 volcanic glass shards and orthopyroxenes were collected from two tephra layers in the core OEJ-b.

A whole-core geochemical composition was analyzed for the cores OEJ-b (Oh-enji marsh) and HJ-4' (Nokinoi lowland) in order to check a relative change of chemical components among each layer, with an ITRAX XRF core scanner at the Kochi Core Center. The core scanner provides a high resolution continuous semi-quantitative elemental profile, as well as an optical and radiograph images. The XRF scans were performed using a molybdenum tube set at 60 kV and 50 mA, with a scan resolution of 10 mm and a count time of 10 seconds. Though the ITRAX core scanner provides data as counts for 34 elements, ranging from Si to Pb, this study reports on elements of Si, S, K, Ca, Ti, V, Cr, Mn, Fe, Br, Rb, Sr, Zr, and Ba those which are of interest for this study by reference to Chagué-Goff et al. (2016). All elemental data were normalized

over kcps (thousand counts per seconds), in order to correct for matrix effects (e.g. Bouchard et al., 2011). Then, normalized data were processed by Dr. Catherine Chagué-Goff (University of New South Wales) using principal component analysis (PCA) to distinguish sediment sources (e.g. Sakuna et al., 2012; Kozak and Niedzielski, 2013; Nakamura et al., 2016; Chagué-Goff et al., 2016, 2017). In this study, the PCA was applied to the sediments evident in 362–367 cm deep of the core OEJ-b and in 101–167 cm deep of the core HJ-4'.

To reconstruct the depositional environments and find past seawater inundations at the study sites, at least 300 diatoms were identified and counted in each sample under the optical microscope at 1000× using oil immersion by Dr. Takashi Chiba (Hokkaido University). The 1-cm-thick samples were taken from the cores OEJ-b (Oh-enji marsh) and HJ-4 (Nokinoin lowland). The diatom identification was based on Krammer and Lange-Bertalot (1986, 1988, 1991a, b), Round et al. (1990), Krammer (2000), Witkowski et al. (2000), Nagumo (2003), Sawai and Nagumo (2003a), Sawai and Nagumo (2003b), Watanabe et al. (2005), Kobayashi et al. (2006), Idei et al. (2012), and Chiba and Sawai (2014).

3.4. Radiocarbon dating

In this study, I selected plant material, mainly seeds, leaves, and their fragments under a stereomicroscope, for radiocarbon dating from an organic-rich mud just beneath and/or above sand and tephra layers. In order to determine a sedimentation rate of the whole core, almost equally spaced dating materials were collected from the core OEJ-b. The radiocarbon analysis was made by accelerator mass spectrometry (AMS) at Beta Analytic Inc., USA. Then, the measured radiocarbon age was converted to calendar age (cal. yr BP) with the calibration program IntCal13 calibration curve (Reimer et al., 2013) and software (Calib 7.1). A sample of shell fragments in the core OEJ-b was collected in consideration of the

marine reservoir effect by using a local data studied at the Kikai Islands located south of Kyushu (Hirabayashi et al., 2017).

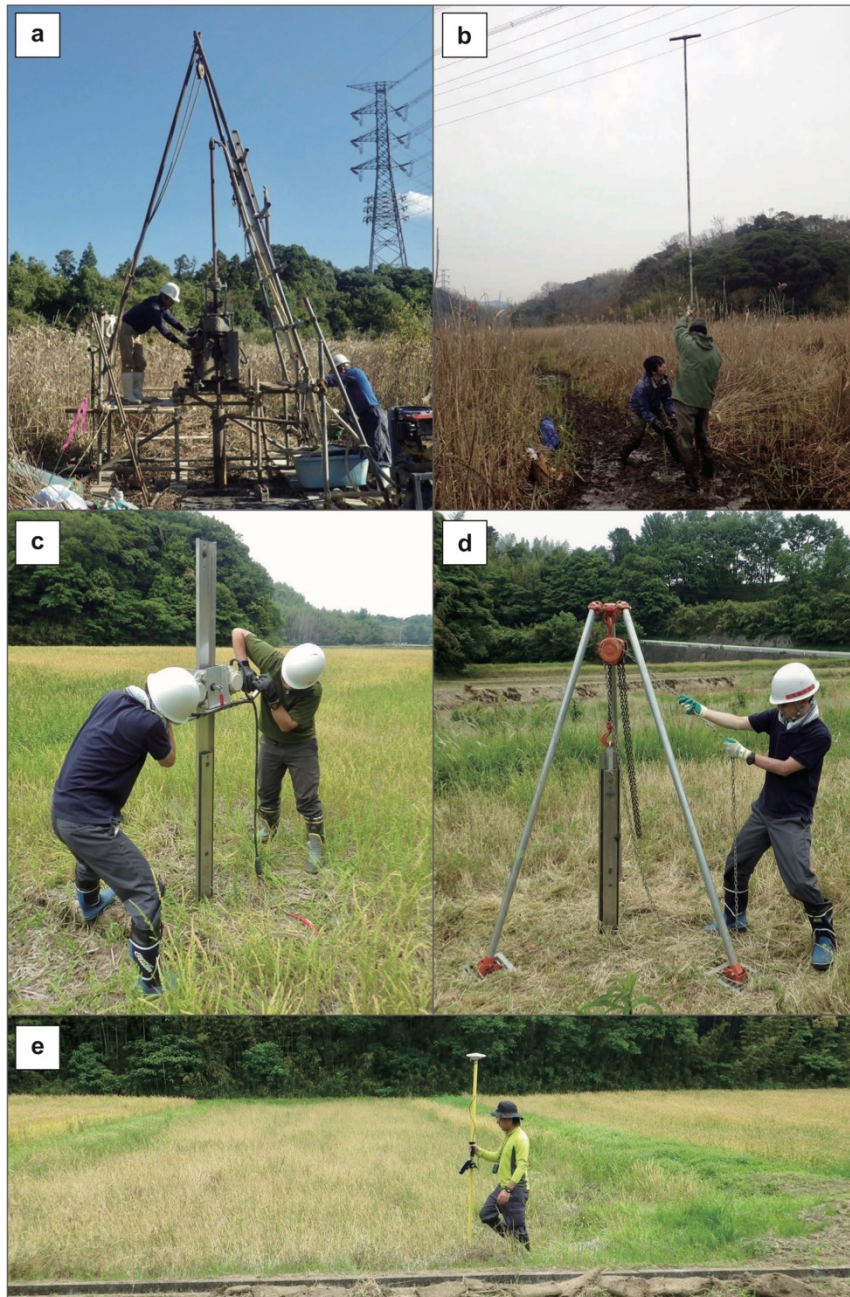


Fig. 3. Photographs of field survey. Sample collection with the use of (a) mechanical thin-wall sampler, (b) gouge sampler, and (c, d) geoslicer. (e) Topographic investigation with a ProMark 100.

Table 3-1. Location, distance from shoreline, length, and sampling method of each core collected in the Oh-enji marsh.

Name	Latitude	Longitude	Distance from shoreline (m)	Core length (cm)	Sampling method
OEJ-1	33.244939	131.779540	131	580	Gouge sampler
OEJ-2	33.244704	131.779491	157	590	Gouge sampler
OEJ-3	33.244442	131.779522	186	590	Gouge sampler
OEJ-4	33.244386	131.779557	193	590	Gouge sampler
OEJ-5	33.244181	131.779578	216	515	Gouge sampler
OEJ-6	33.243631	131.779672	277	500	Gouge sampler
OEJ-7	33.243389	131.779714	305	490	Gouge sampler
OEJ-a	33.244839	131.779524	142	600	Thin-wall sampler
OEJ-b	33.244568	131.779546	173	880	Thin-wall sampler
OEJ-c	33.244056	131.779653	230	840	Thin-wall sampler

Table 3-2. Location, distance from shoreline, length, and sampling method of each core collected in the Nokinoi lowland.

Name	Latitude	Longitude	Distance from shoreline (m)	Core length (cm)	Sampling method
HJ-1	33.366024	131.593026	284	43	Gouge sampler
HJ-2	33.366265	131.592376	350	30	Gouge sampler
HJ-3	33.367862	131.591605	504	180	Geoslicer
HJ-4	33.368788	131.590079	679	170	Geoslicer
HJ-5	33.369731	131.589348	799	200	Geoslicer
HJ-6	33.370222	131.588486	896	200	Gouge sampler
HJ-7	33.365046	131.592849	257	70	Gouge sampler
HJ-8	33.365314	131.590472	473	120	Geoslicer
HJ-9	33.364475	131.588396	677	200	Geoslicer

CHAPTER 4. Results

4.1. Oh-enji marsh

4.1.1. Stratigraphy, tephrochronology, and sedimentary characteristics

The up to 880 cm sedimentary succession is composed of units of lowermost dark-gray sandy mud with shell fragments, silt with alternations of sand and mud, dark brown organic-rich mud, gray muddy sand with gravel, and uppermost agricultural soil, in ascending order (Figs. 4-1, 4-2, 4-3, and 4-4). The sediments change gradually from the agricultural soil to the gray muddy sand layer with gravels, while the organic-rich mud layer is bounded by sharp contact by the upper muddy sand layer, and burrows are observed at this boundary in the cores OEJ-a and OEJ-b (Figs. 4-2, 4-3, and 4-4).

Two continuous tephra layers are evident in the organic-rich mud layer and the silt layer, respectively (Figs. 4-1, 4-2, 4-3, and 4-4). The upper scoria layer with 3–5 cm thickness occurs between 332 cm and 486 cm depths and is composed of light brown angular particles up to 8 mm diameter (Figs. 4-2, 4-3, 4-4, 4-5e, 4-6d, and 4-7c), and there is no trend in thickness and grain size of this layer throughout the all sediment cores (Fig. 4-1). This layer is bounded by sharp upper and lower contacts with surrounding organic-rich muds (Figs. 4-5e, 4-6d, and 4-7c). The scoriae collected from 429–433 cm deep in the core OEJ-b (Figs. 4-3 and 4-6d) consist of volcanic glass shards, light minerals, and heavy minerals such as orthopyroxene and clinopyroxene (Table 4-1). Most of the volcanic glass shards are composed of a porous scoriaceous glass (Fig. 4-8a). The refractive indexes of the volcanic glass shards range at 1.5042–1.5184, 1.5283–1.5400, and 1.5441 with the mode of 1.537–1.538 (Fig. 4-9a and Table 4-1), and this is consistent with the range of upper part of Danbaru Scoria (Kj-DS) (1.5351–1.5417; Table 4-1; Furusawa and Umeda, 2000). The Kj-DS tephra, sourced from Mt. Kuju located 50 km west-southwest of the Oh-enji marsh, comprises four fall units of coarse-grained subplinian scoria of orthopyroxene and clinopyroxene andesite

(Kamata and Kobayashi, 1997). The emplacement age of the Kj-DS is assumed to be 3700–5090 cal yr. BP based on the radiocarbon dating at underlying and overlying humic soils (Kamata and Kobayashi, 1997). The refractive index of the orthopyroxene mainly ranges at 1.704–1.708 and 1.709–1.714, and the mode of that is at 1.706–1.707 and 1.711–1.712 (Figs. 4-8b, 4-9b, and Table 4-1).

The lower volcanic ash layer is evident deeper than 458 cm at the cores OEJ-a, b, c, and 2, with the thickness in excess of 100 cm (Figs. 4-1, 4-2, 4-3, and 4-4). The layer takes on a light brown color and is composed of very fine particles showing a massive structure (Figs. 4-2, 4-3, and 4-4). The volcanic ash collected from 630–635 cm deep in the core OEJ-b is made up primarily of bubble-walled flat volcanic glass shards (Fig. 4-8c). The refractive indexes of the volcanic glass shards range mainly between 1.5103 and 1.5166 with the mode of 1.511 (Fig. 4-9c and Table 4-1), and this value is consistent with the range of Kikai Akahoya tephra (K-Ah) which fell 7170–7300 cal. yr BP associated with the eruption of the Kikai caldera located on the south of Kyushu Island (e.g. Machida and Arai, 1978; Smith et al., 2013).

Three up to 2-cm-thick sand layers are observed in sediment cores especially at the seaward sites (Fig. 4-1). Each sand layer is numbered from A to E beginning at the top with a central focus on the core OEJ-b. The intersite comparison of the sand layers A–C, occurring in the organic-rich mud, is carried out based on sedimentary facies, grain size distribution, mineral composition, and appearance depths as well as radiocarbon ages. Sand layer A occurs at 257–259 cm deep in the core OEJ-b and is composed of fine to very coarse sand with rounded granules and pebbles (Figs. 4-3, 4-6a, 4-10e, and Table 4-2). This sand layer consists mainly of feldspar, quartz, and rock fragments (Table 4-3). Sand layer B is also composed mainly of feldspar, quartz, and rock fragments and is characterized by a sub-layer structure of fine to medium sand (Figs. 4-2, 4-3, 4-4, 4-10b, f, i, Tables 4-2, and 4-3). It is visible in the cores OEJ-a and OEJ-b (Figs. 4-2, 4-3, 4-5b, and 4-6b), while it is invisible in the core OEJ-c without an observation of the CT image (Figs.

4-4 and 4-7b). Thin sand layers also occur in the cores obtained using the gouge sampler although it is difficult to observe sedimentary characteristics because of a smallness in diameter of the sampler. The cores OEJ-1–3 contain two thin or patchy sand layers, and just one sand layer is evident in the cores OEJ-4, 5, and 7, whereas there is no sand layer in the core OEJ-6 (Fig. 4-1). Sand layer C is subtle in the cores OEJ-a–c, due to its discontinuity in the cores and also minor difference in color from surrounding organic-rich mud, but obviously observed in the CT images (320–322 cm in the core OEJ-a; Figs. 4-2 and 4-5c, 363–366 cm deep in the core OEJ-b; Figs. 4-3 and 4-6c, and 450–452 cm deep in the core OEJ-c; Fig. 4-4). This layer consists mostly of fine- to coarse-sized rock fragments (Fig. 4-10c, g, j, Tables 4-2, and 4-3). Several sand layers of the alternations are light gray in color and usually less than 2 cm thick, but there are relatively thick sand layer D in the core OEJ-a (20 cm thick with 82.6% mud content) and OEJ-c (14 cm thick with 39.0% mud content) (Figs. 4-1, 4-2, 4-4, and Table 4-2). The sand layer D is composed mainly of very fine- to fine-sized rock fragments and feldspar, and the upper part of the layer is poorly sorted (Fig. 4-11, Tables 4-2, and 4-3). This layer shows inland thinning trend although it is observed only at two cores.

In addition to the sand layers A–D, two gravel layers are observed in the core OEJ-a (Figs. 4-1, 4-2, and 4-5a, d). They are composed of rounded granules which are similar to those in the sand layer A in the core OEJ-b (Figs. 4-3, 4-6a, and 4-10a, d, e), but such a gravel layer is not observed at any other cores, including the cores collected using the gouge sampler (OEJ-1–7; Figs. 2-2, 4-1, and Table 3-1). There is a poorly sorted sand layer at 314–317 cm deep in the OEJ-c which consists of fine to very coarse sand with granules and pebbles, and the sedimentary facies of this layer looks like no other layers (Figs. 4-7a, 4-10h, and Table 4-2).

It is also noteworthy that up to 8 cm thick sand layer E occurs just beneath the K-Ah tephra layer in the cores OEJ-b and OEJ-c (Figs. 4-1, 4-3, and 4-4). This layer, bounded by sharp contacts with upper K-

Ah tephra and lower silt layer, is characterized by grains of very fine to very coarse sand with a gravel of 3 cm diameter (Figs. 4-6e, 4-7e, 4-12, and Table 4-2). The volcanic glass shards of K-Ah tephra make up the majority of this layer, but the coarser particles are composed of feldspar, rock fragments, quartz, and magnetite (Table 4-3). The sand layer E between 651–655 cm deep in the core OEJ-b shows a clear grading structure, whereas a subtle inverse grading structure is observed at the sand layer E between 721–729 cm deep in the core OEJ-c (Fig. 4-12 and Table 4-2).

The beach sand at the Oh-enji marsh is mainly composed of fine to medium sand (Figs. 2-2a, 4-10k, and Table 4-2). The mineral composition of the beach sand is rock fragments, feldspar, quartz, pyroxene, and hornblende (Table 4-3).

4.1.2. Magnetic susceptibility and geochemical signatures

The magnetic susceptibility in the core OEJ-b exhibits four major peaks at the layers of agricultural soil, muddy sand with gravels, upper part of K-Ah, and the sand layer E (Fig. 4-13). The Mo Inc/Mo Coh ratio, which is a proxy for an amount of organic content (e.g. Chagué-Goff et al., 2016), shows a distinct increase between 210 cm and 460 cm. The elemental profiles are divided mainly into three groups; silt with alternations of sand and mud (460–880 cm deep), organic-rich mud (210–460 cm deep), and agricultural soil and muddy sand (0–210 cm deep) (Fig. 4-13). A count/kcps of silicon (Si), potassium (K), calcium (Ca), titanium (Ti), vanadium (V), chromium (Cr), manganese (Mn), iron (Fe), rubidium (Rb), strontium (Sr), and barium (Ba) increase at 460–880 cm and 0–210 cm deeps, with a gradual decrease from 460 cm to 400 cm deeps. Bromine (Br) displays a different profile to the above mentioned elements.

Peaks in count/kcps occur at 257–259 cm deep (sand layer A) for Si, K, Ca, Ti, Fe, and Sr; 314–316 cm deep (sand layer B) for K, Ca, Ti, and Sr; 363–366 cm deep (sand layer C) for Si, K, Ca, Ti, Mn, and

Sr; 651–655 cm deep (sand layer E) for Si, Ca, Cr, and Sr (Fig. 4-13). There is a marked increase in counts/kcps of sulfur (S) at the bottom of the muddy sand layer in the depth of 180–210 cm (Fig. 4-13).

Principal component analysis (PCA) is applied with 1 mm interval to the sediment between 362 cm and 367 cm deeps in the core OEJ-b in order to verify the difference in component material between the subtle sand layer C and surrounding organic-rich muds (Figs. 4-3, 4-6c, and 4-14). The PCA result shows that two principal components can explain 59% of the variance (PC1: 50% and PC2: 9%) (Fig. 4-14). The plotted area of the subtle sand layer C (363–366 cm deep) is clearly different from the upper and lower organic-rich muds (362–363 cm and 366–367 cm deeps) that are plotted around Mo Inc/Mo Coh and Br (Fig. 4-14).

4.1.3. Diatoms

The fossil diatom assemblages indicate that the sediments at the marsh record an overall change from marine to freshwater environments (Figs. 4-15 and 4-16). The interval of 140–880 cm deep in the core OEJ-b is divided into four diatom zones on the basis of species dominance relative to total diatom valves counted, and records an overall change from marine to freshwater (Figs. 4-15 and 4-16). The major changes in fossil diatom assemblages are observed at depths of 210 cm (boundary between zones 1 and 2) and 460 cm (boundary between zones 2 and 3). Zone 1, the muddy sand layer at 140–210 cm deep, is characterized by species of freshwater–brackish and brackish–marine diatoms, but freshwater diatoms are not abundant. The brackish–marine diatoms such as *Biremis ambigua*, *Delphineis surirella* (No. 15 in Fig. 4-17), and *Planthidium delicatulum* (No. 16 in Fig. 4-17) occupy 76% of the total at 199–200 cm deep (Fig. 4-16). The fossil diatom assemblages in the organic-rich mud (zone 2) are mainly composed of freshwater species with less than 10% of freshwater–brackish species such as *Cyclotella meneghiniana* (No. 10 in Fig. 4-17).

In contrast to zone 2, the silt layer above the K-Ah (zone 3) is characterized by species of freshwater–brackish, brackish–marine, and marine environments along with less abundant freshwater species. In the zone 4, brackish–marine and marine diatoms are common, but freshwater species are rare (Fig. 4-15).

Fossil Diatom assemblages in the sand layers A–C in the organic-rich mud are characterized by freshwater–brackish diatoms such as *Pseudopodosira kosugii* (No. 12 in Fig. 4-17), *Rhopalodia gibberula*, and *Staurosira sopotensis*, brackish–marine diatoms such as *Adoneis pacifica*, *Delphineis surirella* (No. 15 in Fig. 4-17), *Diploneis suborbicularis*, *Melosira moniliformis*, *Planothidium delicatulum* (No. 16 in Fig. 4-17), and *Thalassiosira* spp.1 (Nos. 17 and 18 in Fig. 4-17), and marine diatoms such as *Chaetoceros* resting spore (No. 19 in Fig. 4-17) and *Thalassiosira* spp.2 that are not observed in the surrounding organic-rich muds (Fig. 4-15). The abundance of freshwater–brackish, brackish–marine, and marine diatoms is increased at these sand layers (Fig. 4-16).

4.1.4. Radiocarbon ages

Twenty-six radiocarbon ages are obtained by the AMS method on samples from the core OEJ-b as well as the cores OEJ-a, OEJ-c, and OEJ-7 (Fig. 4-18 and Table 4-4). Sell fragments obtained at 879–880 cm deep in the core OEJ-b are dated to 8050–8320 cal. yr BP (No. 24 in Table 4-4), and plant material and insect remains collected from the top of the organic-rich mud (215–217 cm deep) are dated to 2760–2860 cal. yr BP (No. 6 in Table 4-4), indicating that this sediment succession records a period of about 5500 years (Fig. 4-18).

The radiocarbon ages obtained within and below the K-Ah tephra layer in the core OEJ-b are dated to 7000–7180 cal. yr BP and 6990–7170 cal. yr BP (Nos. 20 and 21 in Table 4-4), and this almost coincided with the depositional age of the K-Ah tephra (7170–7300 cal. yr BP; Smith et al., 2013). The radiocarbon

ages of plant material just above and below the Kj-DS tephra in the core OEJ-b are 5740–5900 cal. yr BP and 5590–5660 cal. yr BP, respectively (Figs. 4-3, 4-18, and Nos. 16 and 17 in Table 4-4). The radiocarbon age of 5710–5890 cal. yr BP is also obtained just below the Kj-DS tephra in the core OEJ-a (Figs. 4-2, 4-18, and No. 4 in Table 4-4). However, the age of the Kj-DS tephra is dated to 3700–5090 cal yr. BP by Kamata and Kobayashi (1997). In this study, since I selected leaves and seeds from the organic-rich mud and the overall radiocarbon ages were determined with few inconsistencies, the depositional age of the Kj-DS tephra is more reliable (Fig. 4-18 and Table 4-4).

The radiocarbon ages of two thin gravel layers observed at the depths of 256 cm and 345 cm in the core OEJ-a are dated to 4080–4260 cal. yr BP and 5370–5460 cal. yr BP (Figs. 4-2, 4-18, and Nos. 1 and 3 in Table 4-4). The radiocarbon age of 4280–4430 cal. yr BP is obtained immediately below the sand layer B which occurs at 268–270 cm deep in the core OEJ-a (No. 2 in Table 4-4). Plant material collected just below the sand layer D in the core OEJ-a is dated to 6670–6790 cal. yr BP (No. 5 in Table 4-4). On the basis of radiocarbon ages obtained above and/or below the sand layers that occur in the core OEJ-b, the maximum range of each depositional age for the sand layers A–C is 3330–3450 cal. yr BP, 4230–4530 cal. yr BP, and 5160–5290 cal. yr BP or later (Figs. 4-3, 4-18, and Nos. 8, 9, 11, 12, and 14 in Table 4-4). The sand layer B characterized by a sub-layer structure evident at 389–394 cm deep in the core OEJ-c is dated to 4070–4160 cal. yr BP (Figs. 4-4, 4-18, and No. 25 in Table 4-4), and this age matches with the depositional ages of the sand layer B in the cores OEJ-a and OEJ-b (Fig. 4-18 and Nos. 2, 11, and 12 in Table 4-4). A radiocarbon age of 5050–5190 cal. yr BP is obtained from fragments of leaves and seeds collected immediately beneath a sand layer (281–285 cm deep) in the core OEJ-7 (Fig. 4-18 and No. 26 in Table 4-4). This age is overlap with the age of the sand layer C in the cores OEJ-a and OEJ-b (Figs. 4-2, 4-3, 4-18, and Nos. 3 and 14 in Table 4-4).

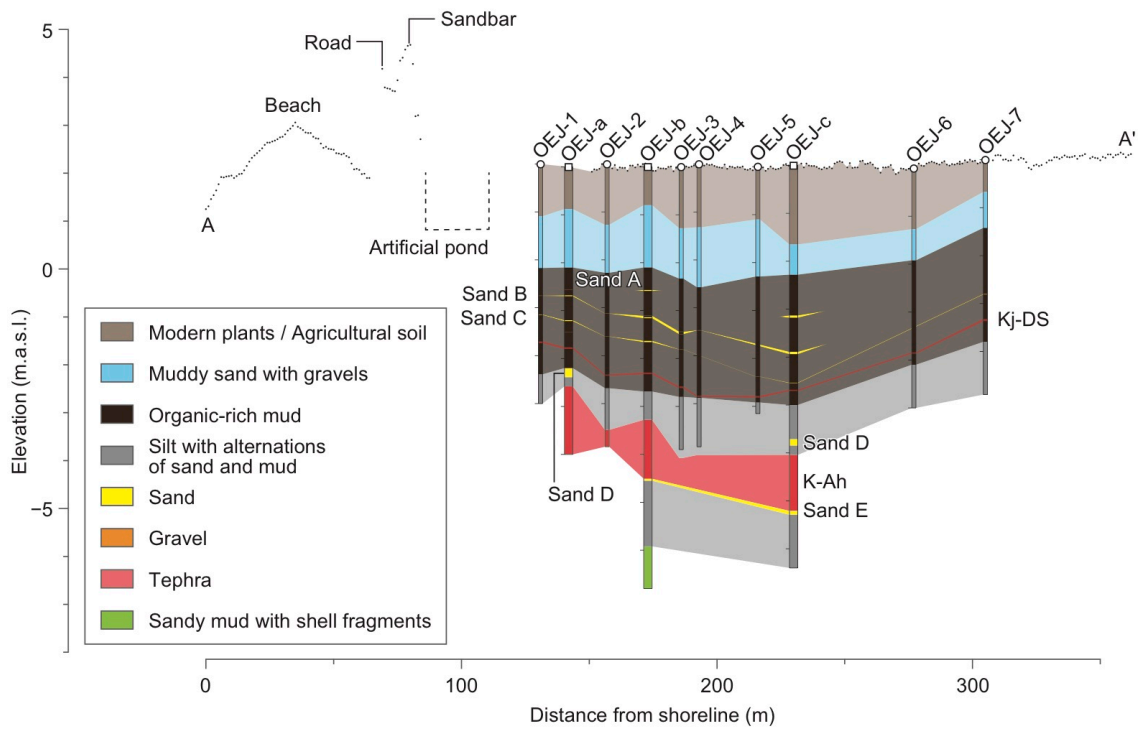


Fig. 4-1. Cross-section of sedimentary columns along the transect A–A' in the Oh-enji marsh.

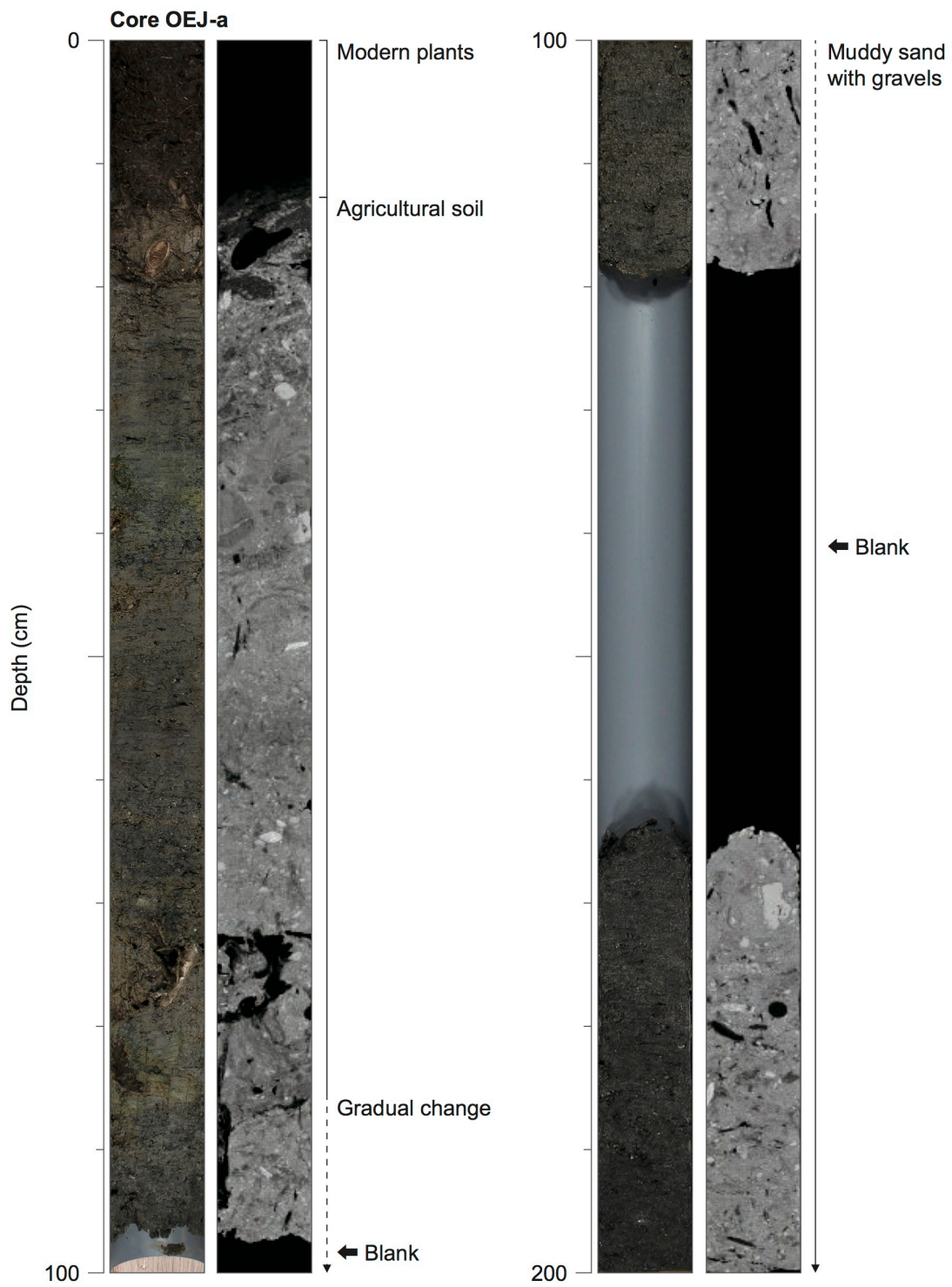


Fig. 4-2. Photograph and CT image of the sediment core at OEJ-a in the Oh-enji marsh. Sedimentary facies, sand layers, tephra layers, and radiocarbon ages are shown on the right side of the CT image.

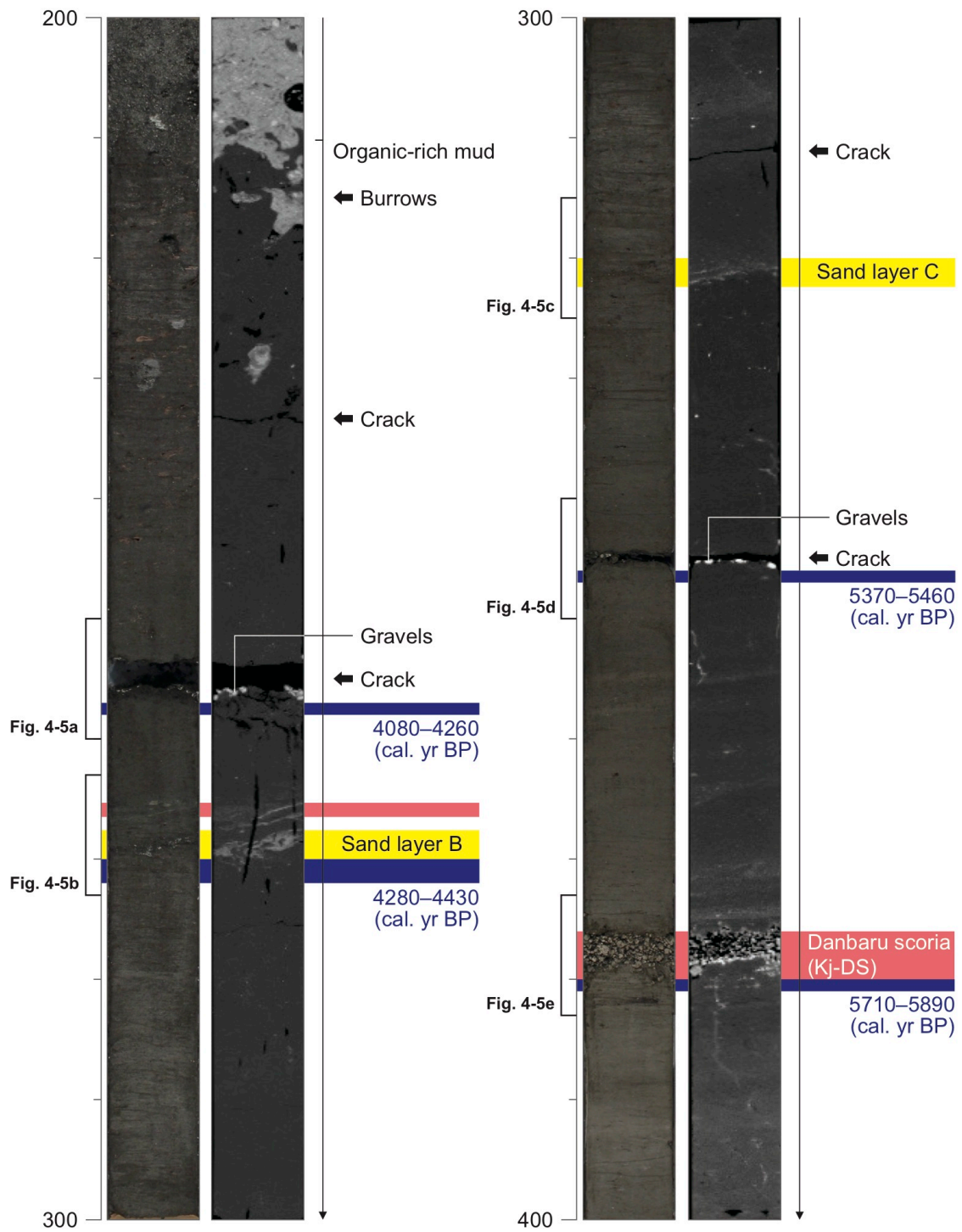


Fig. 4-2. (continued)

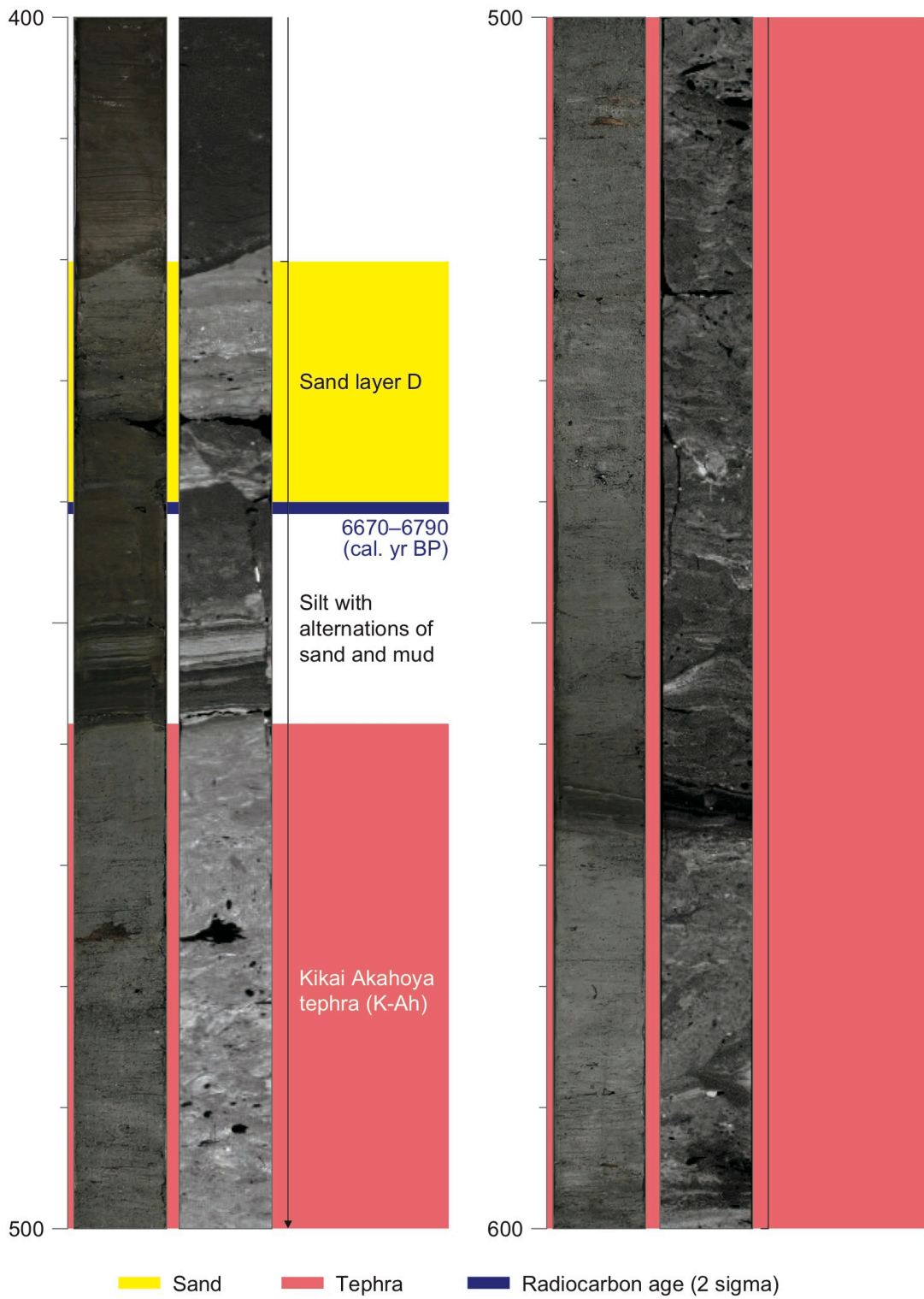


Fig. 4-2. (continued)

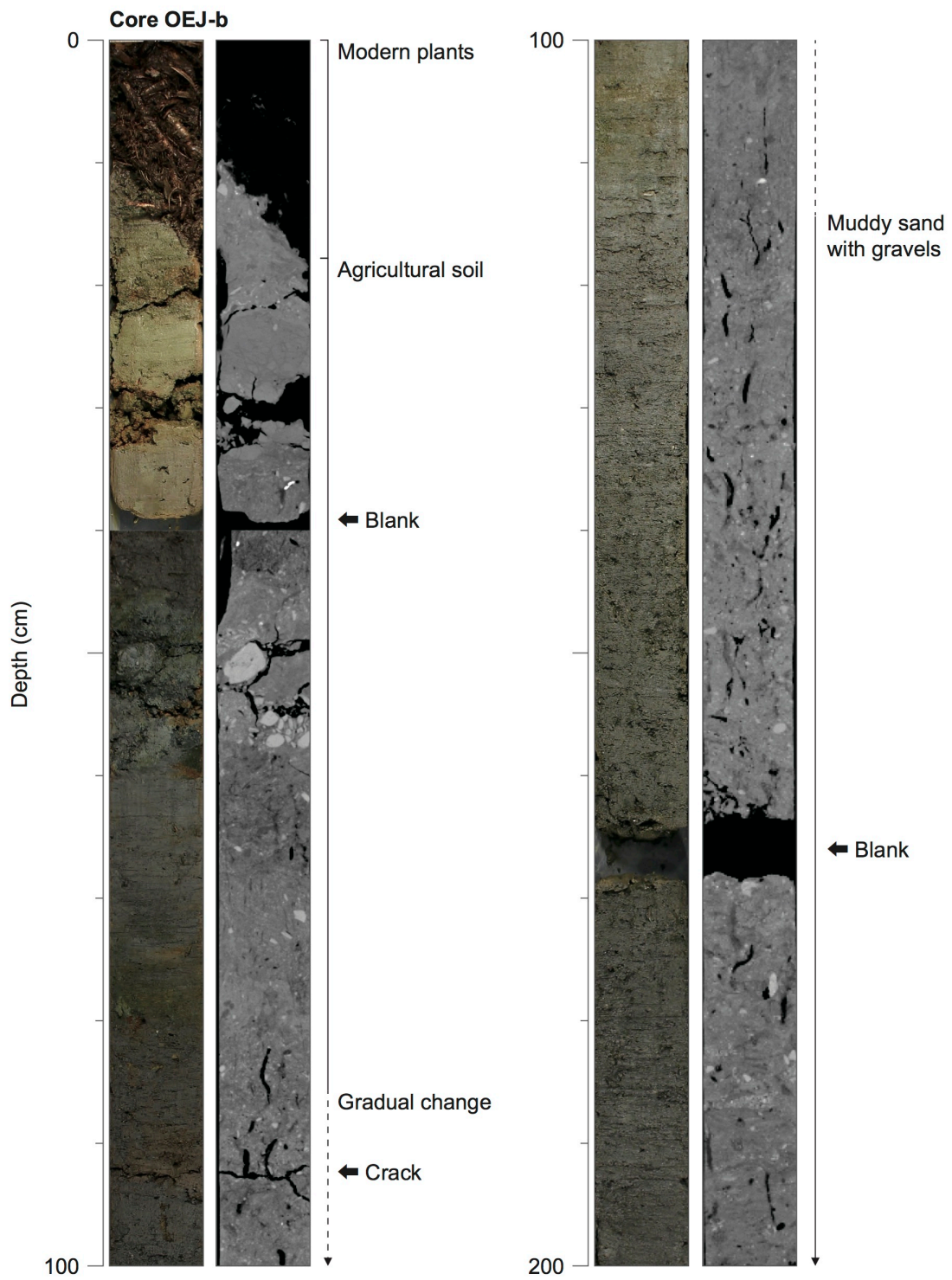


Fig. 4-3. Photograph and CT image of the sediment core at OEJ-b in the Oh-enji marsh. Sedimentary facies, sand layers, tephra layers, and radiocarbon ages are shown on the right side of the CT image.

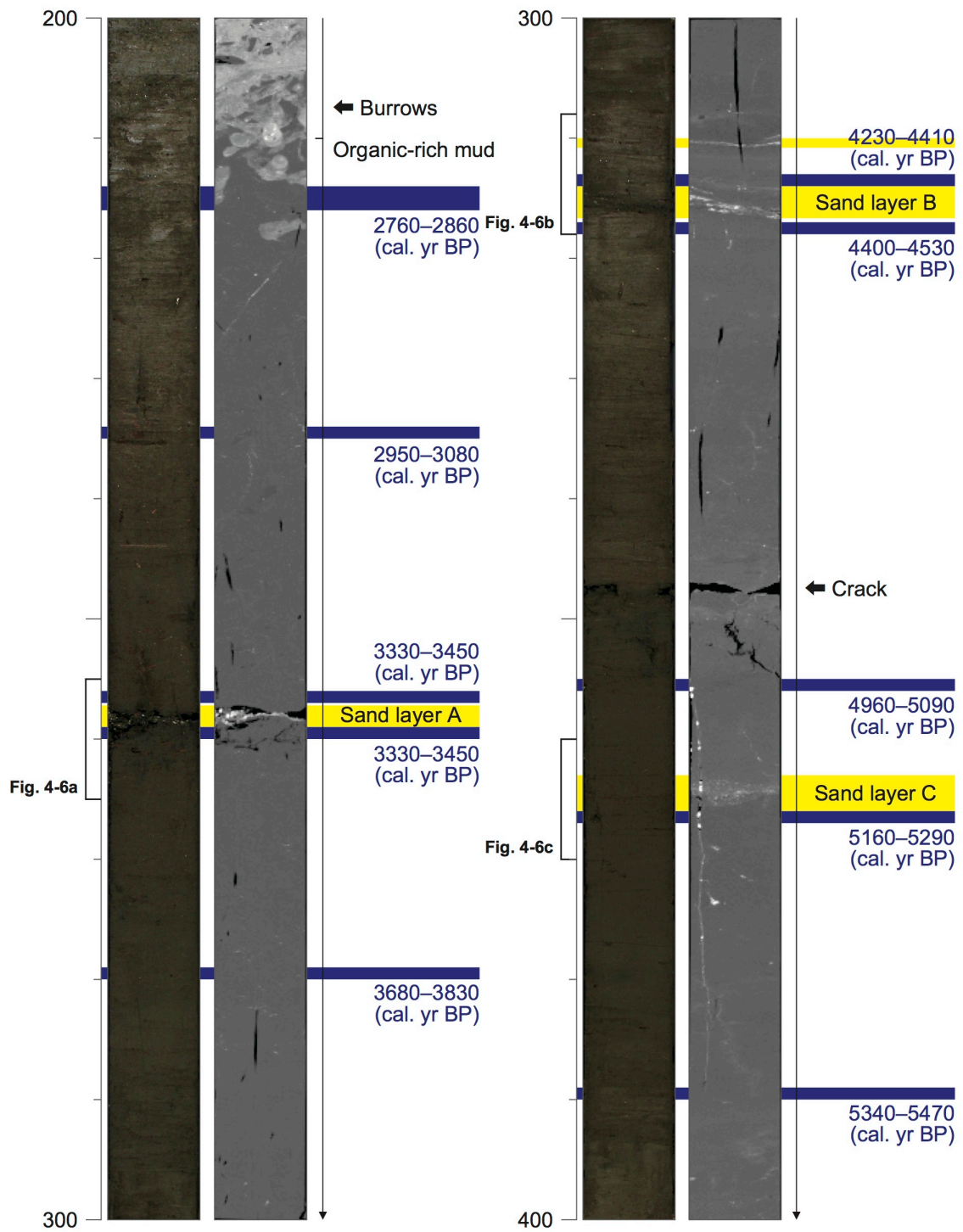


Fig. 4-3. (continued)

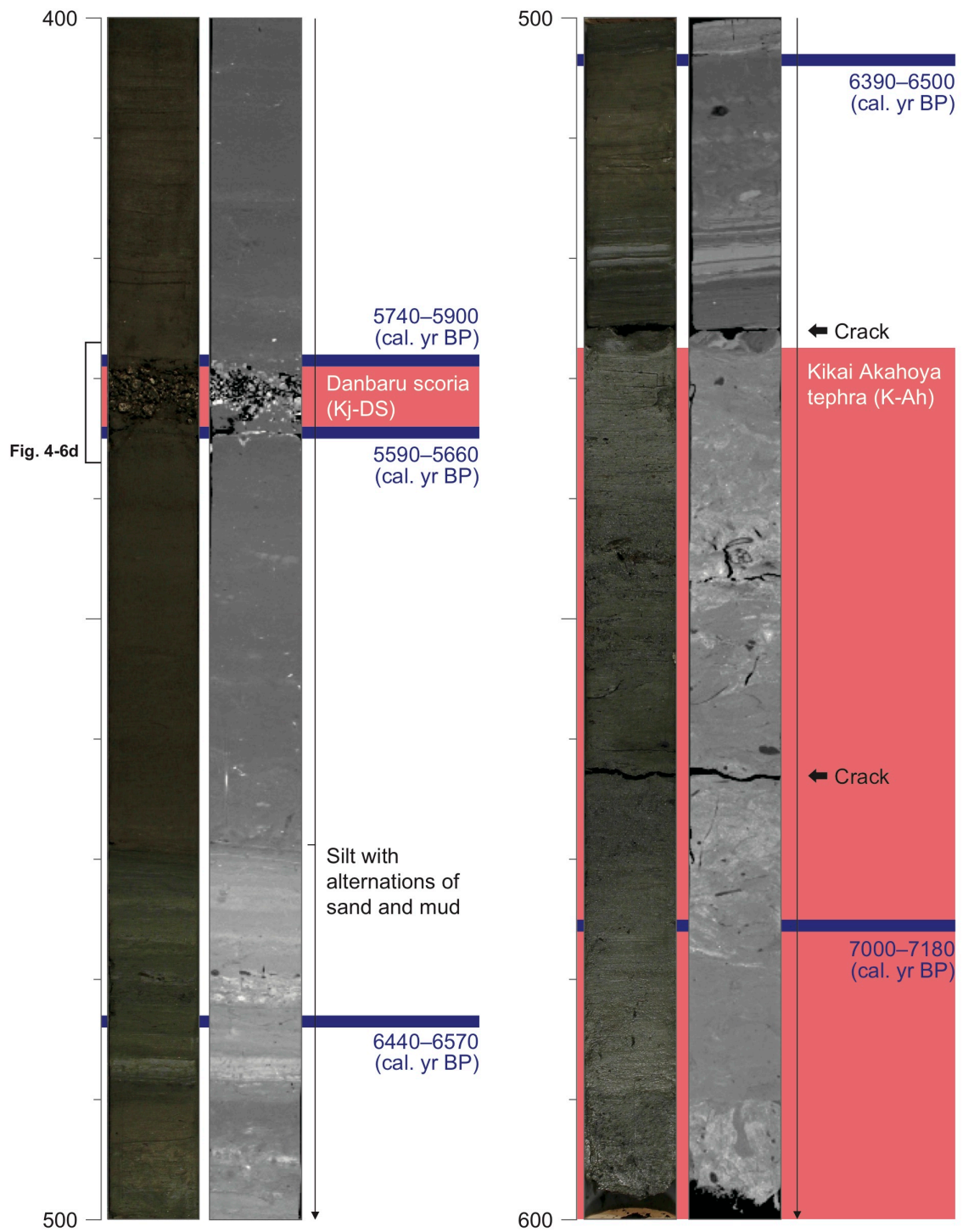


Fig. 4-3. (continued)

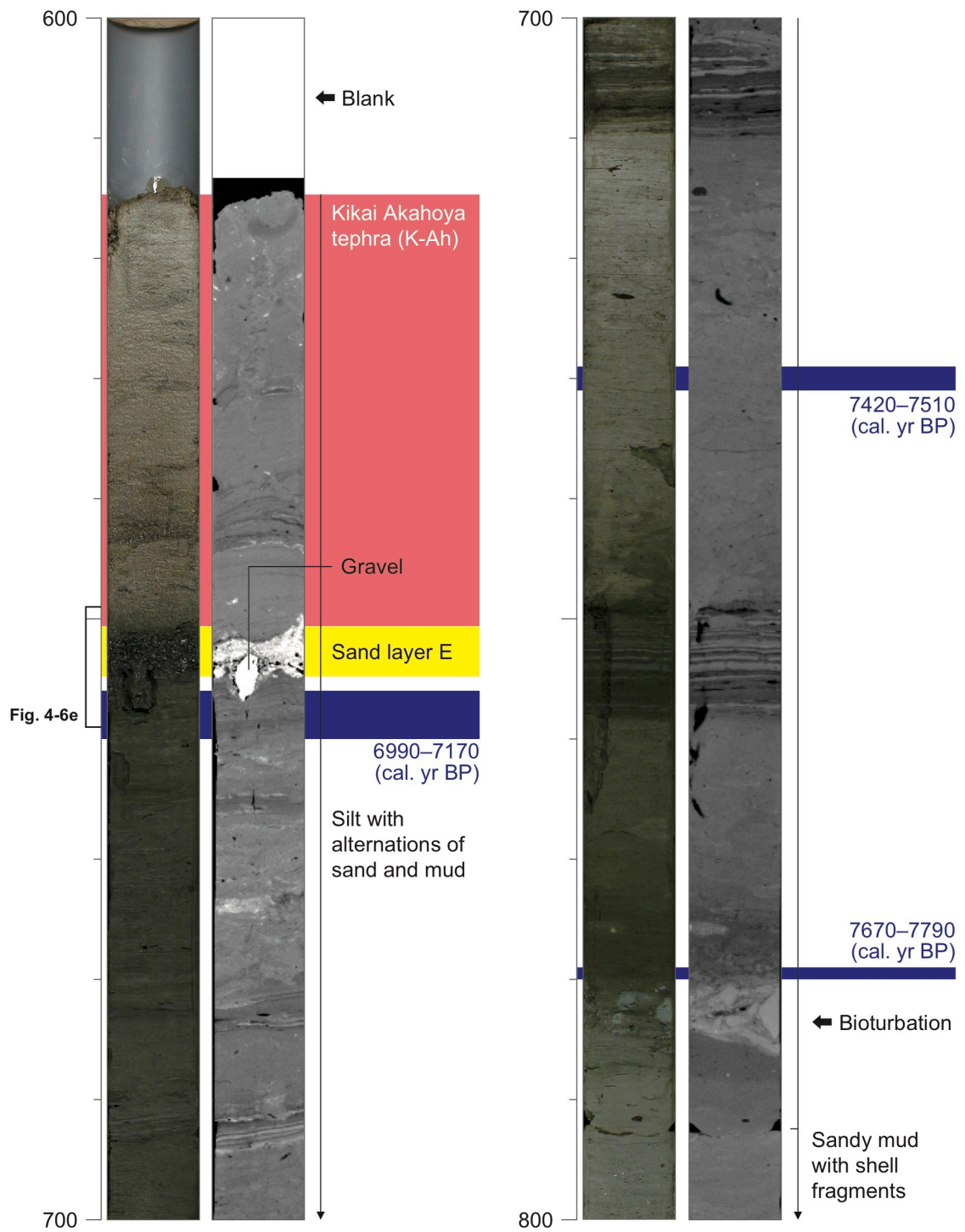


Fig. 4-3. (continued)

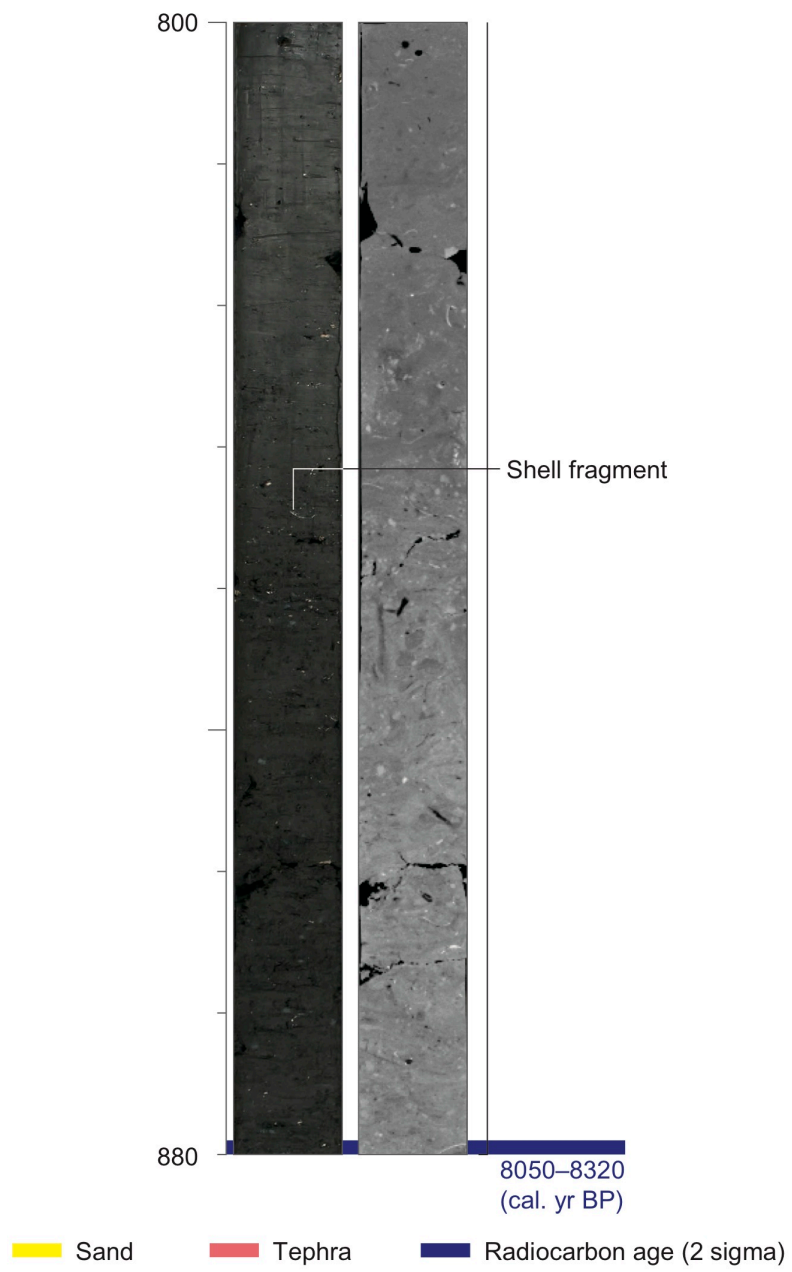


Fig. 4-3. (continued)

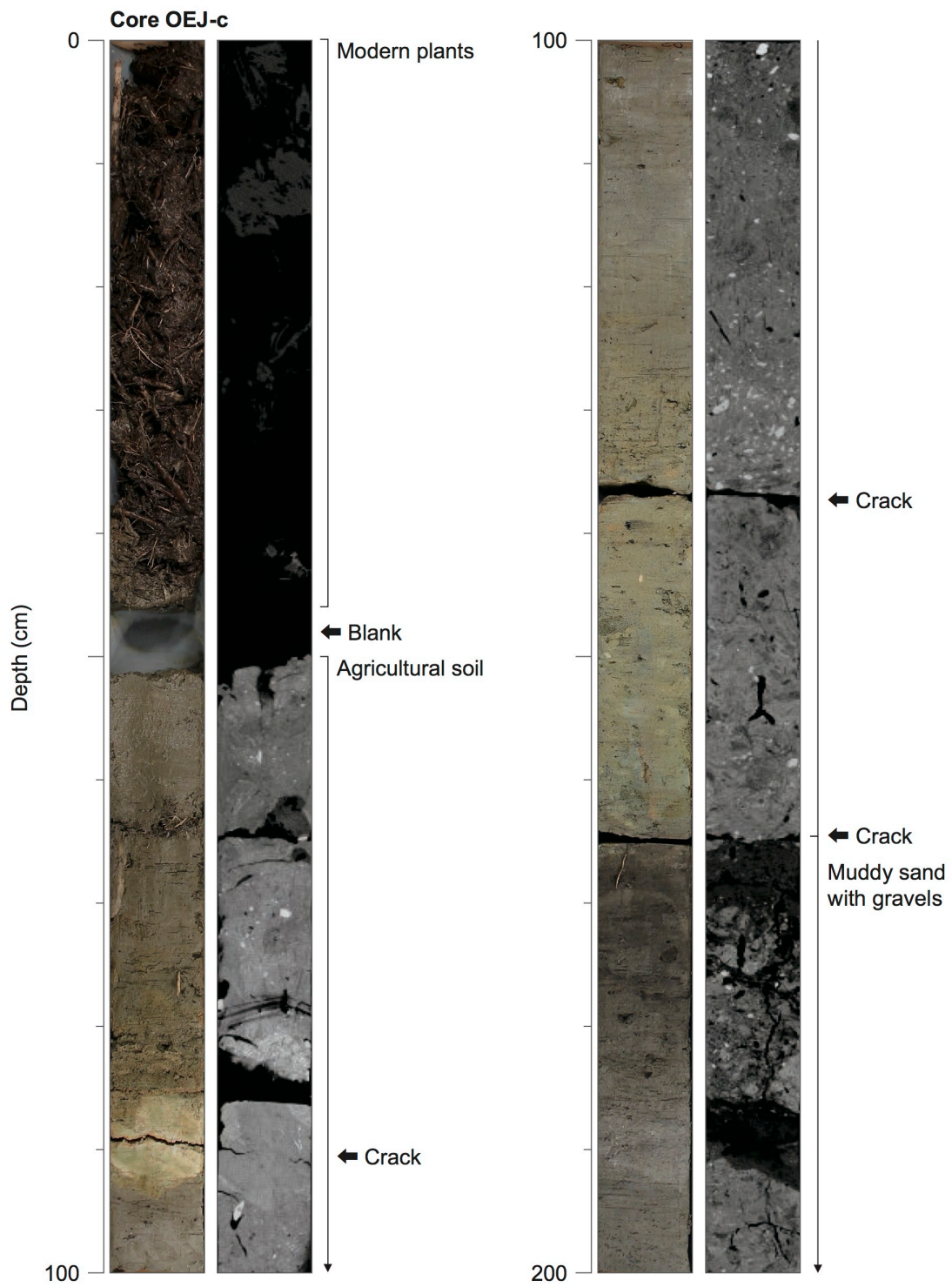


Fig. 4-4. Photograph and CT image of the sediment core at OEJ-c in the Oh-enji marsh. Sedimentary facies, sand layers, tephra layers, and radiocarbon ages are shown on the right side of the CT image.

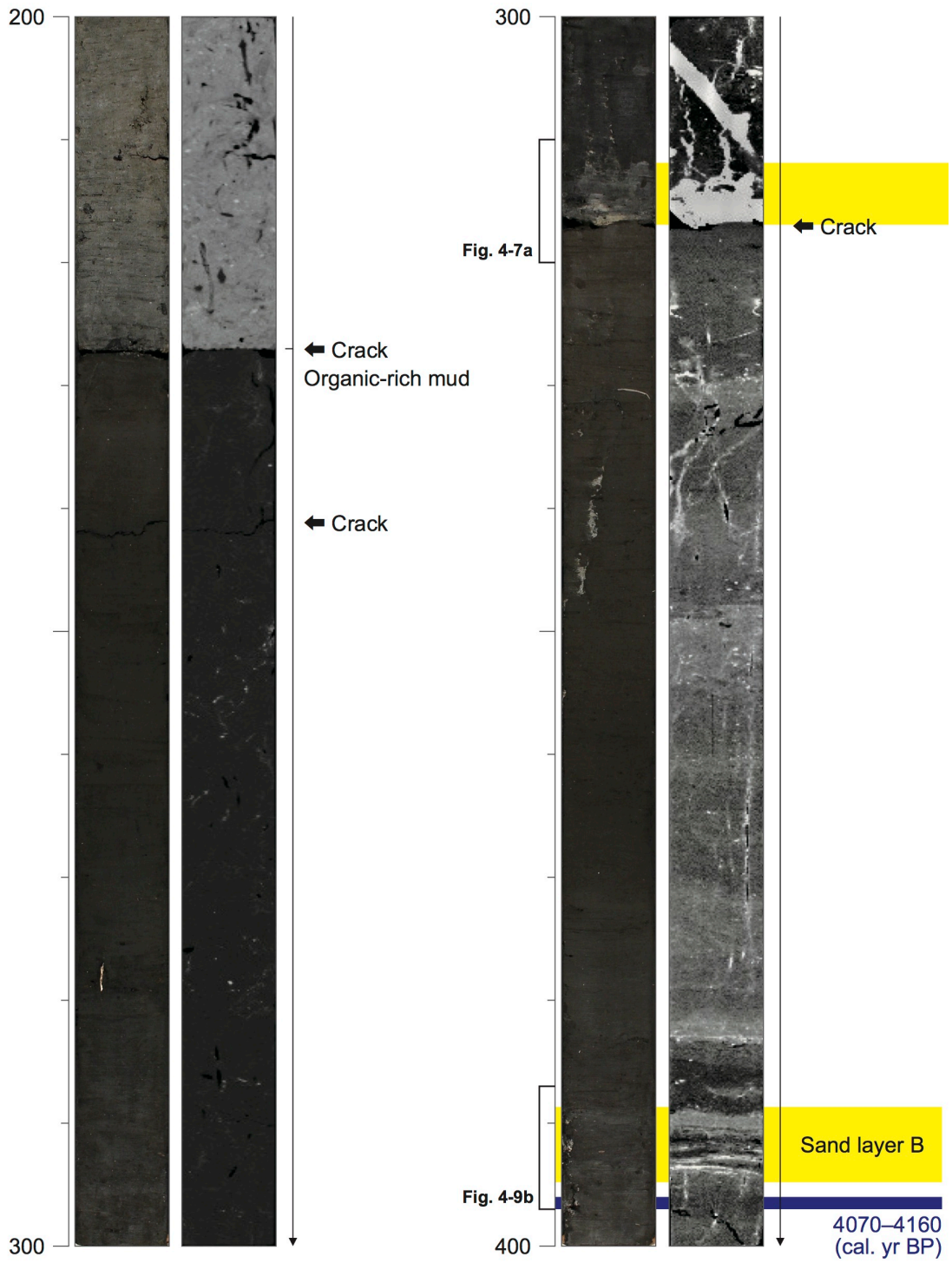


Fig. 4-4. (continued)



Fig. 4-4. (continued)

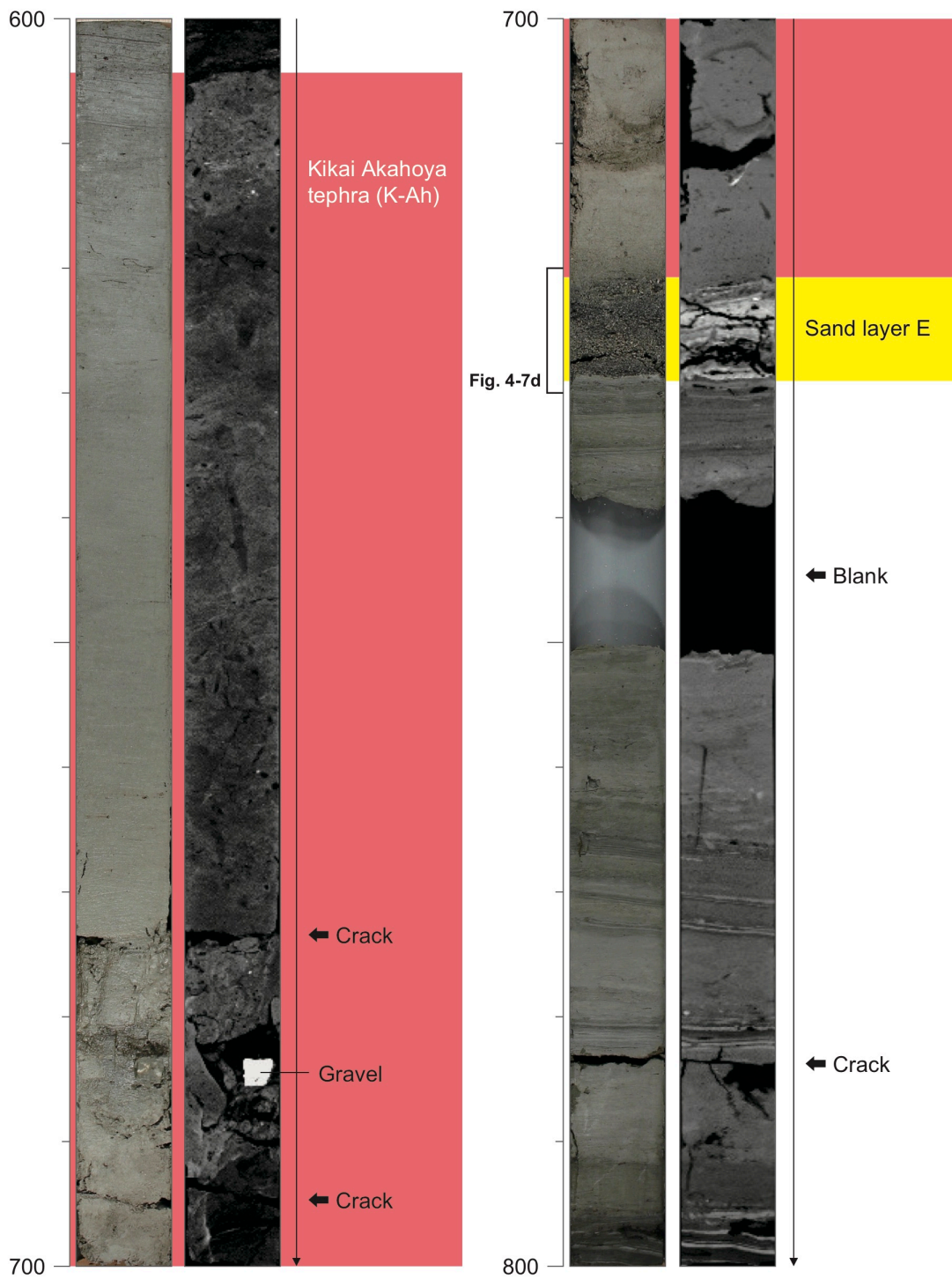
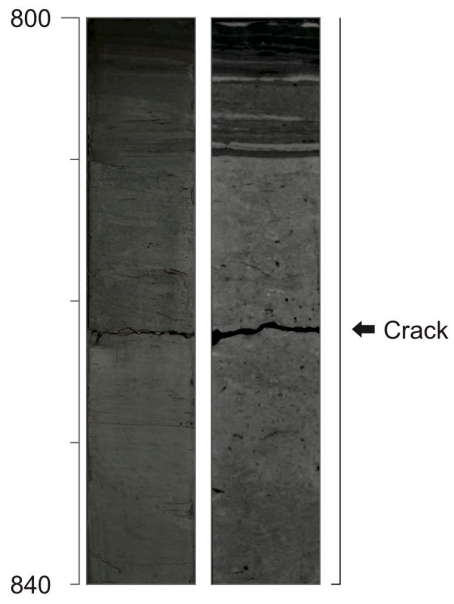


Fig. 4-4. (continued)



■ Sand ■ Tephra ■ Radiocarbon age (2 sigma)

Fig. 4-4. (continued)

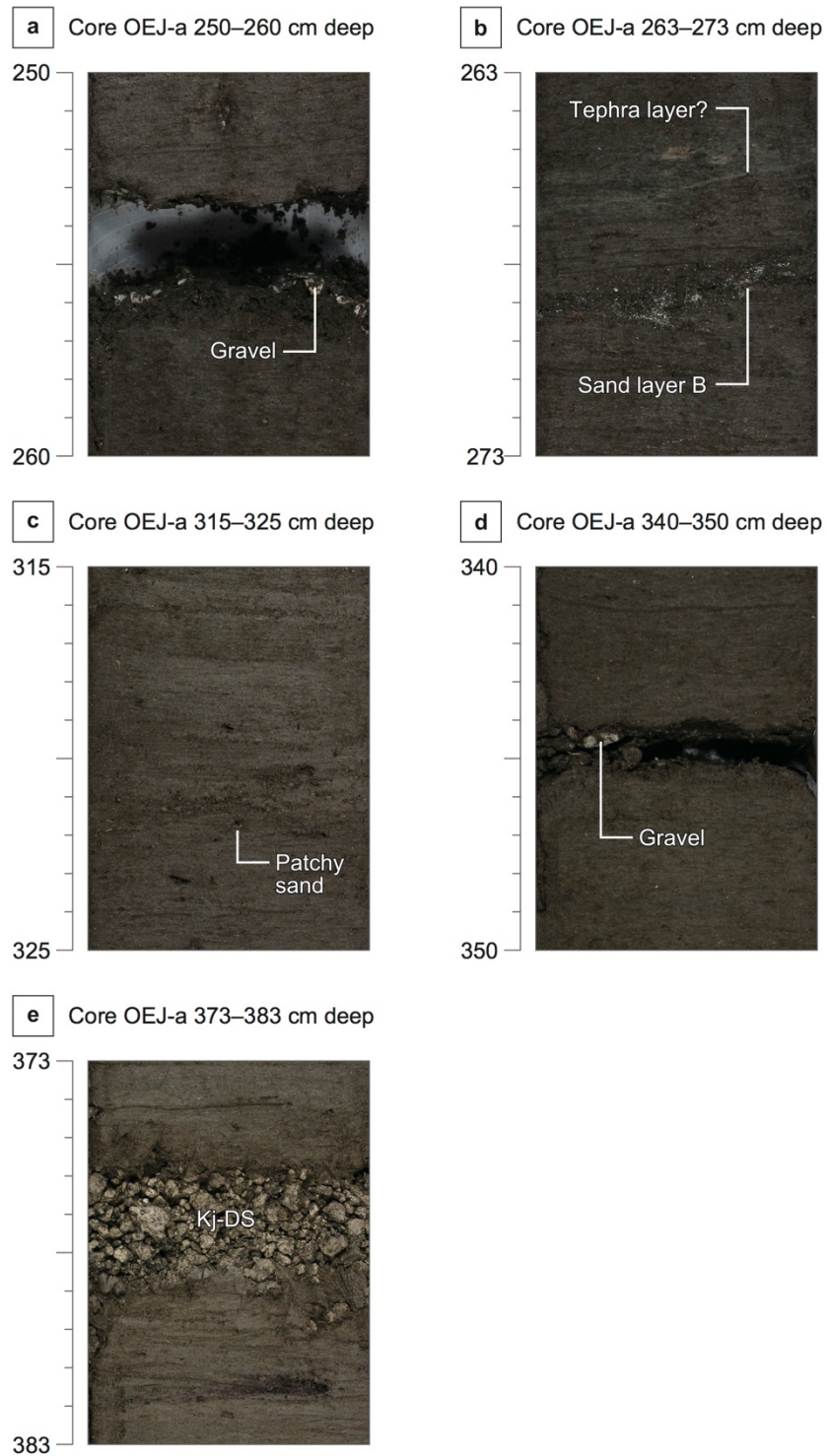


Fig. 4-5. Enlarged photographs of typical layers in the core OEJ-a. (a) 250–260 cm deep, (b) 263–273 cm deep, (c) 315–325 cm deep, (d) 340–350 cm deep, and (e) 373–383 cm deep.

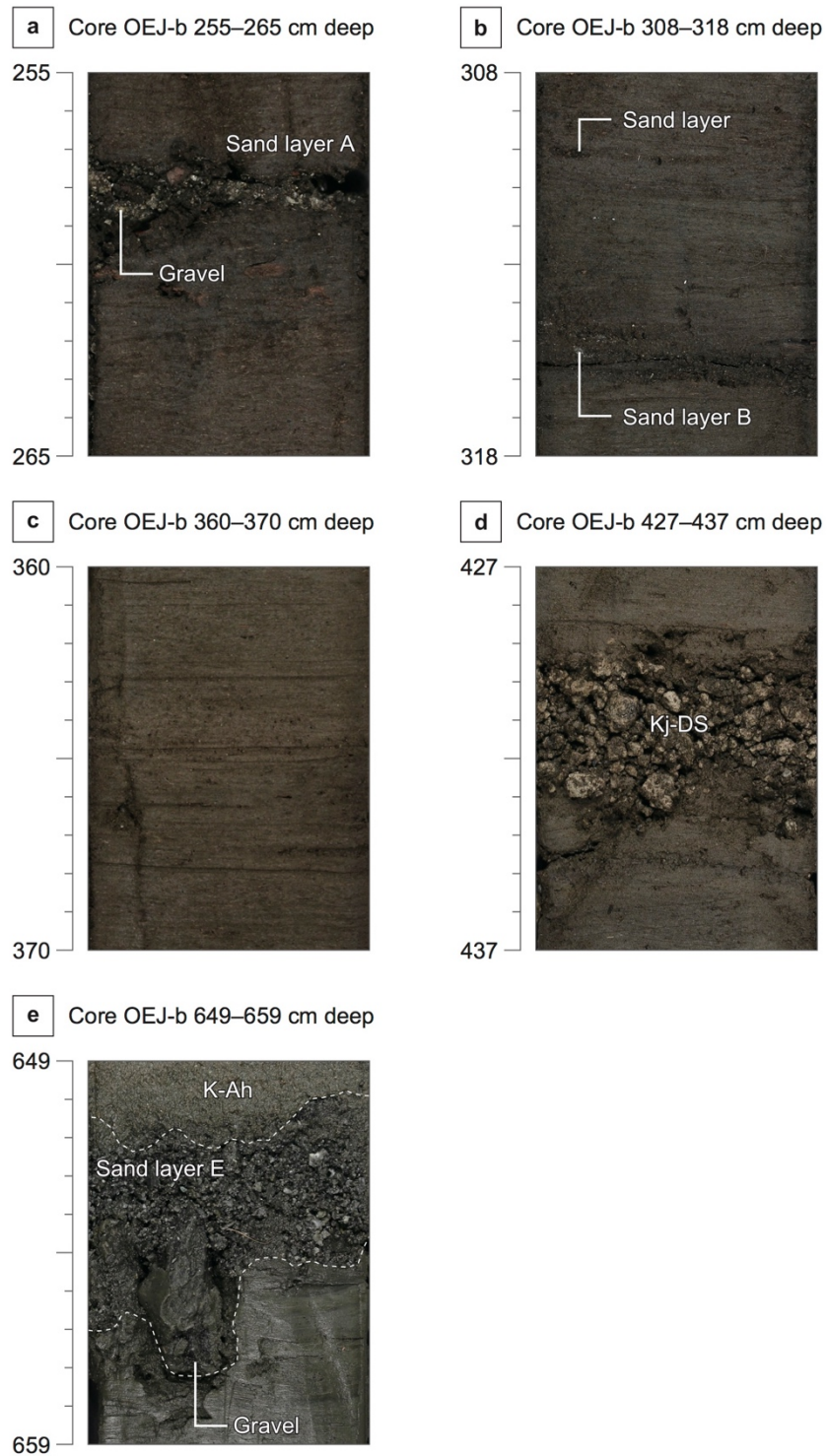


Fig. 4-6. Enlarged photographs of typical layers in the core OEJ-b. (a) 255–265 cm deep, (b) 308–318 cm deep, (c) 360–370 cm deep, (d) 427–437 cm deep, and (e) 649–659 cm deep.

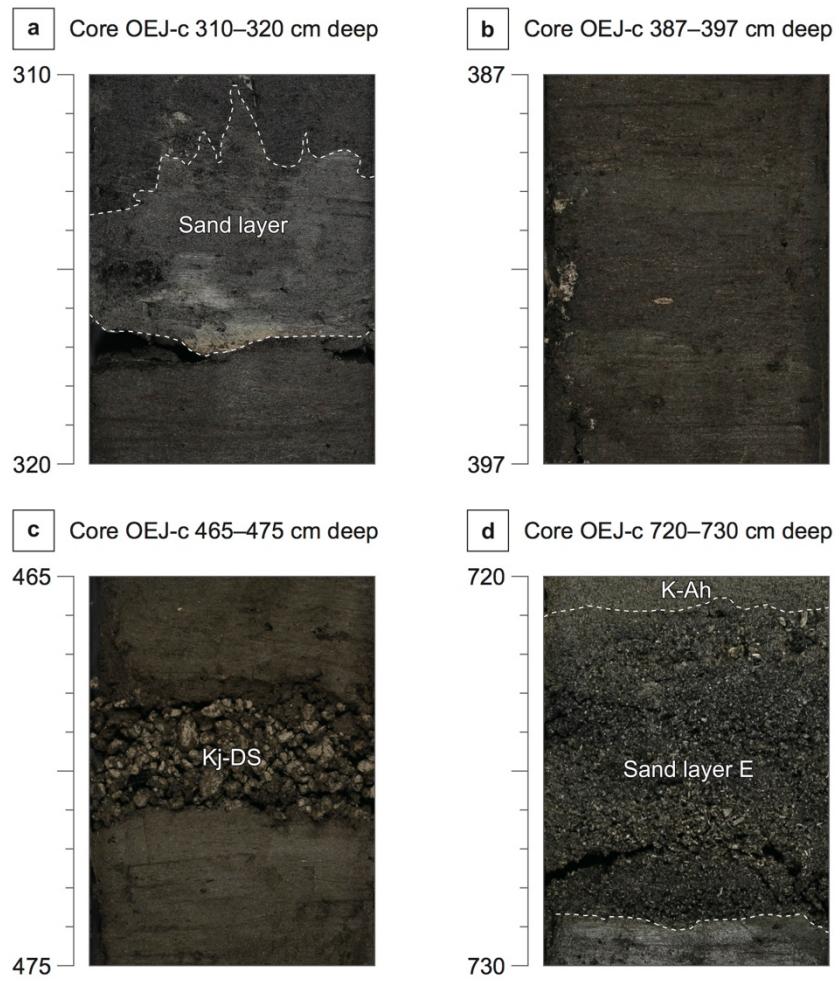


Fig. 4-7. Enlarged photographs of typical layers in the core OEJ-c. (a) 310–320 cm deep, (b) 387–397 cm deep, (c) 465–475 cm deep, and (d) 720–730 cm deep.

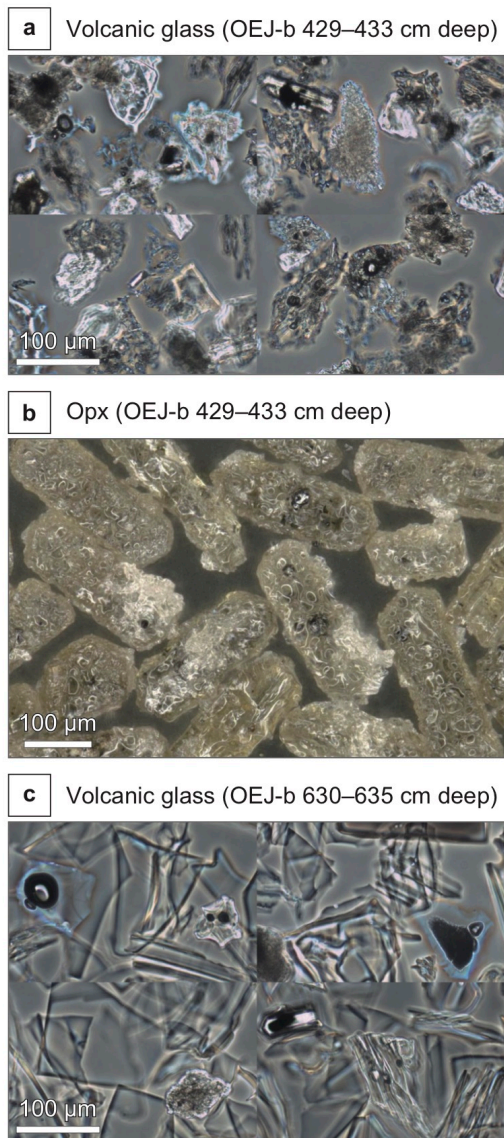


Fig. 4-8. Micrographs of (a) volcanic glass shards (429–433 cm deep), (b) orthopyroxene grains (429–433 cm deep), and (c) volcanic glass shards (630–635 cm deep) present in the core OEJ-b (conducted by Kyoto Fission-track Co. Ltd.).

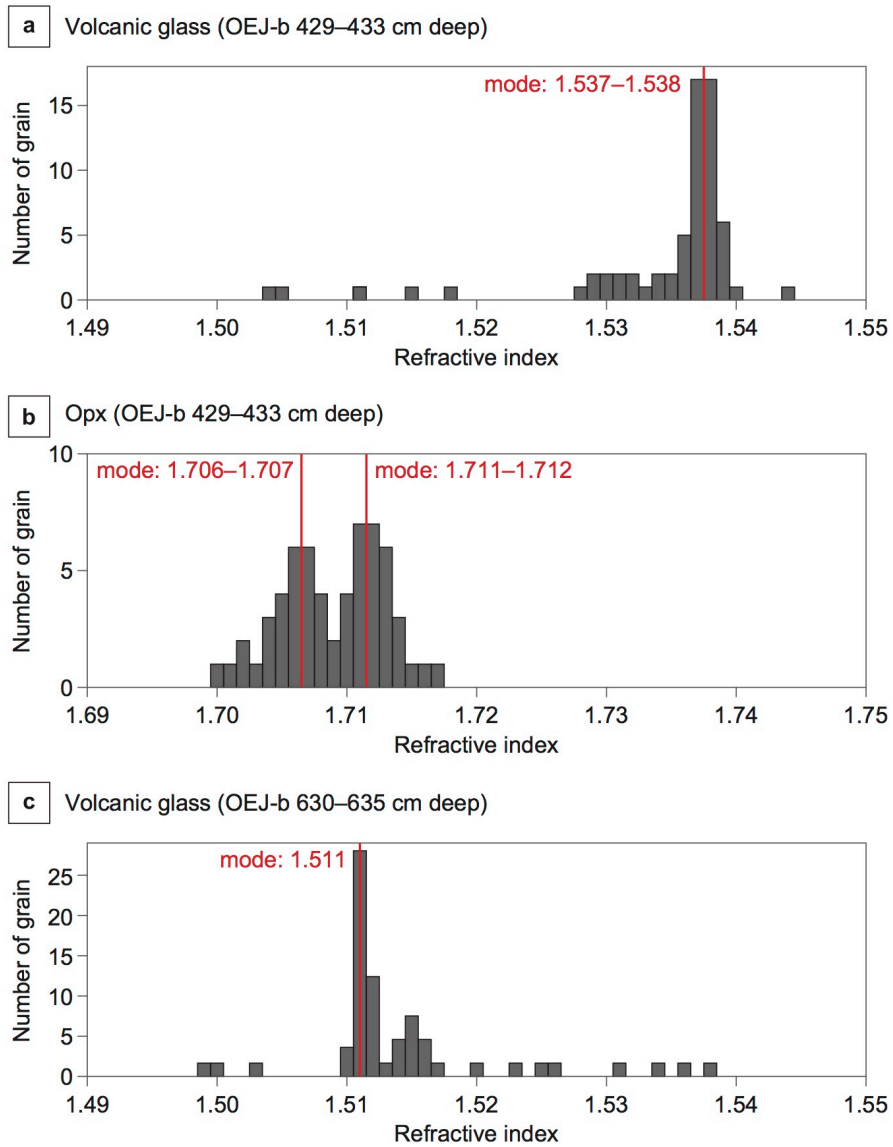


Fig. 4-9. Refractive index of (a) 66 shards of volcanic glass (429–433 cm deep), (b) 71 grains of orthopyroxene (429–433 deep), and (c) 71 shards of volcanic glass (630–635 cm deep) present in the core OEJ-b (conducted by Kyoto Fission-track Co. Ltd.).

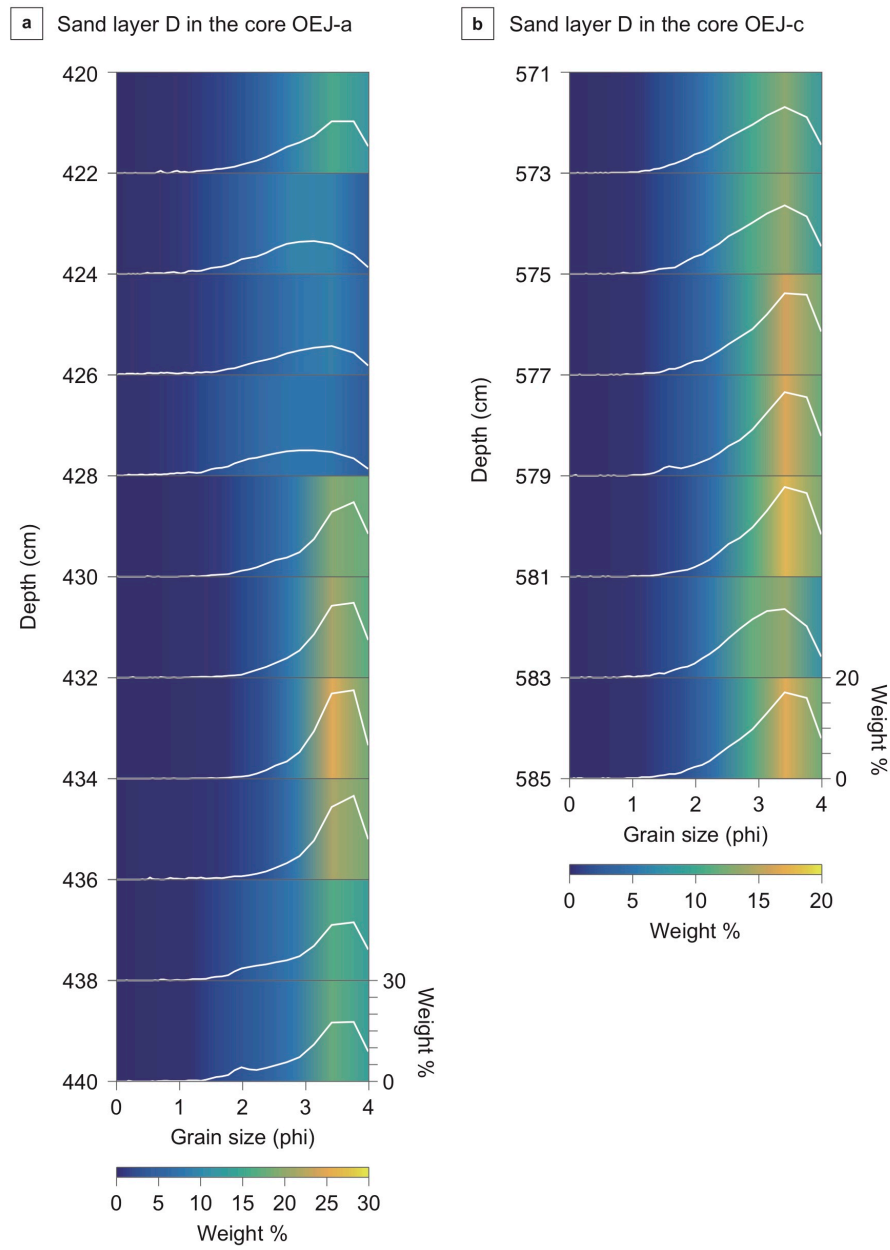


Fig. 4-11. Vertical variation in grain size distribution of the sand layer D at (a) 420–440 cm deep in the core OEJ-a and (b) 571–585 cm deep in the core OEJ-c.

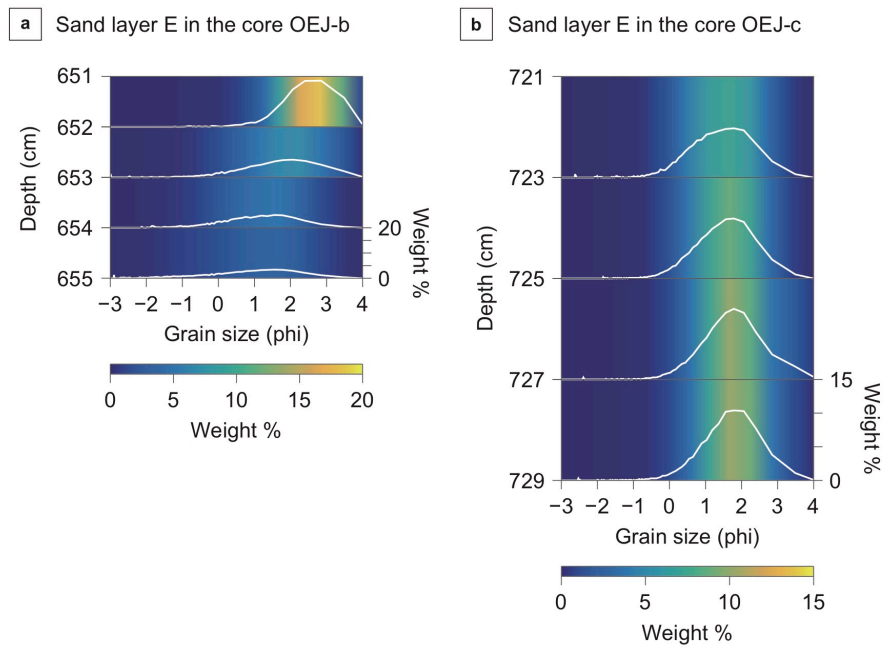


Fig. 4-12. Vertical variation in grain size distribution of the sand layer E at (a) 651–655 cm deep in the core OEJ-b and (b) 721–729 cm deep in the core OEJ-c.

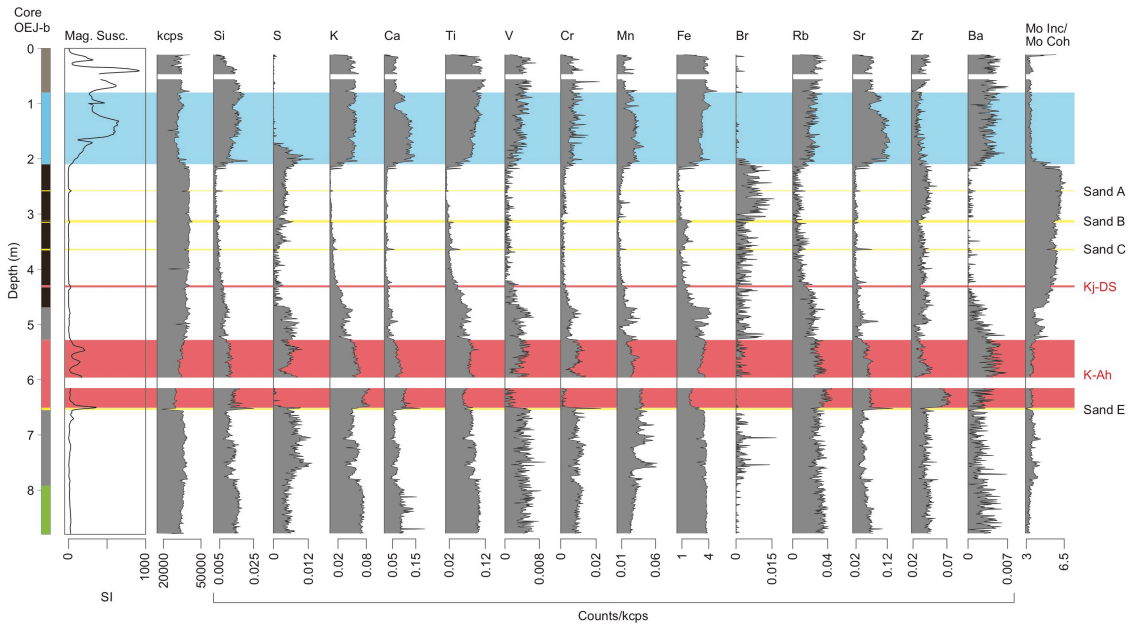


Fig. 4-13. Magnetic susceptibility (Mag. Susc.) and ITRAX data of the core OEJ-b. All ITRAX data, except for Mo Inc/Mo Coh, are normalized over kcps. A color coding of the column corresponds to that of Fig. 4-1.

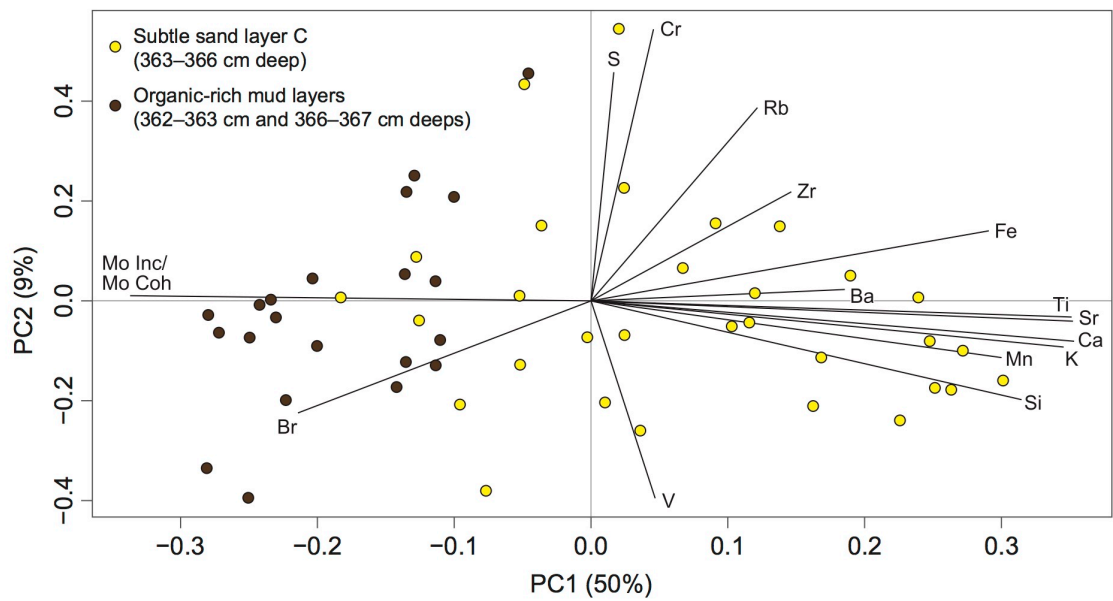


Fig. 4-14. Scores and loading of the PCA of normalized XRF data from 362–367 cm deep in the core OEJ-b. Yellow and brown dots show the subtle sand layer C (363–366 cm deep) and the surrounding organic-rich mud layers (362–363 cm and 366–367 cm deeps), respectively (provided by Dr. Catherine Chagué-Goff).

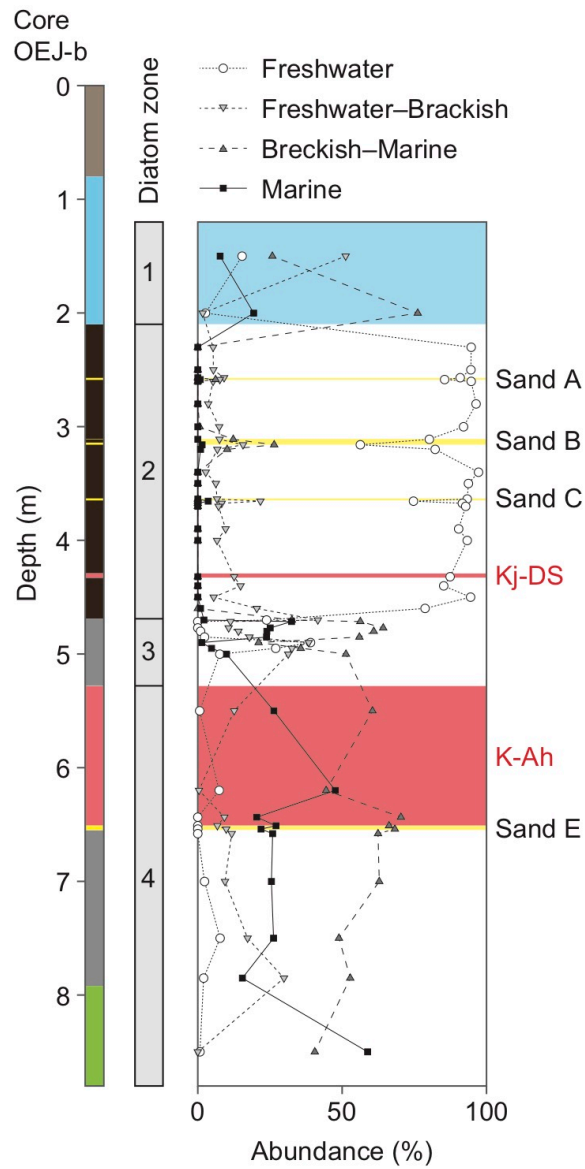


Fig. 4-16. Abundance of freshwater, freshwater-brackish, brackish-marine, and marine diatoms in the core OEJ-b (provided by Dr. Takashi Chiba). A color coding of the column corresponds to that of Fig. 4-1.

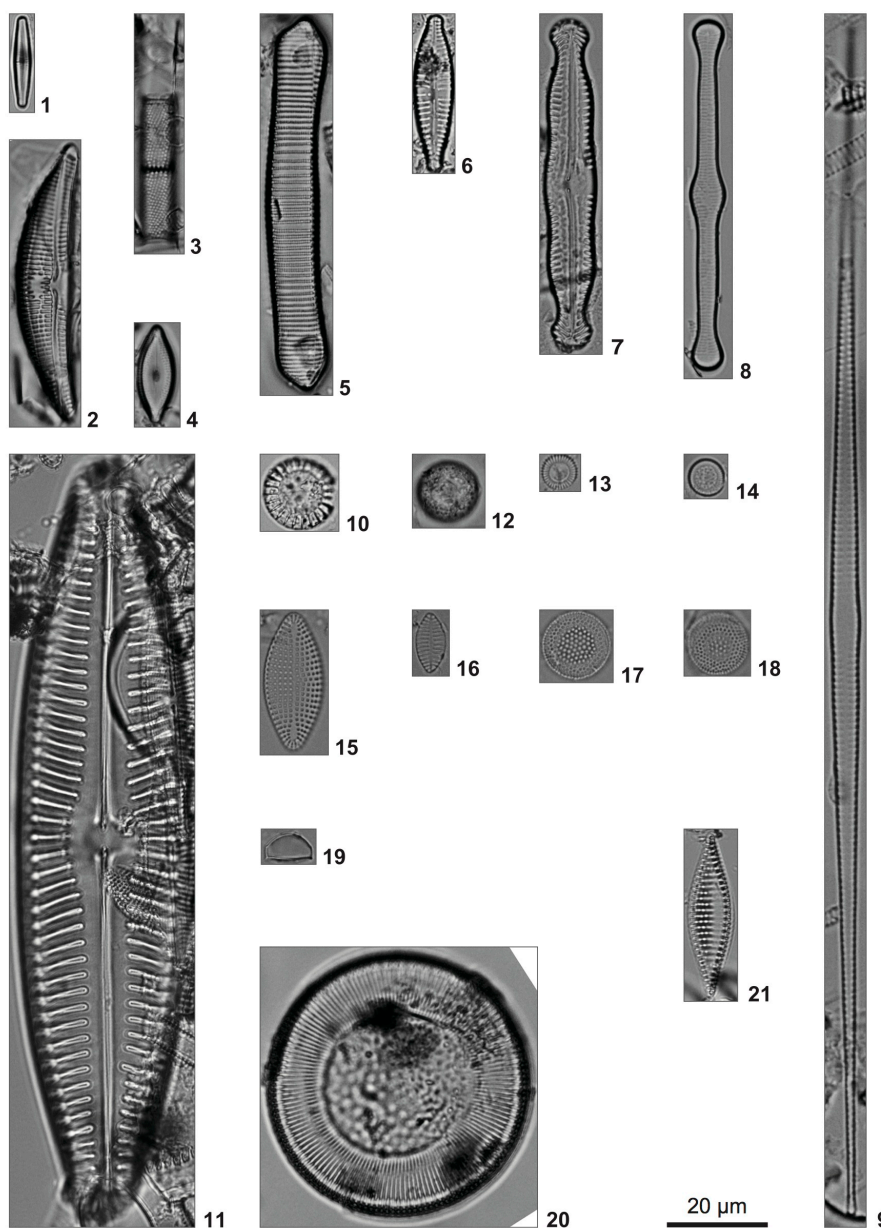


Fig. 4-17. Micrographs of typical diatoms in the core OEJ-b. 1–9: Freshwater species, 10–12: Freshwater–Brackish species, 13–18: Brackish–Marine species, and 19–21: Marine species; 1: *Achnantheidium minutissimum*, 2: *Amphora copulata*, 3: *Aulacoseira granulata*, 4: *Diadesmis confervacea*, 5: *Eunotia formica*, 6: *Gomphonema parvulum*, 7: *Pinnularia subnodosa*, 8: *Tabellaria fenestrata*, 9: *Ulnaria japonica*, 10: *Cyclotella meneghiniana*, 11: *Pinnunavis yarrensis*, 12: *Pseudopodosira kosugii*, 13: *Cyclotella* sp.1, 14: *Cyclotella* sp.2, 15: *Delphineis surirella*, 16: *Planothidium delicatulum*, 17–18: *Thalassiosira* spp.1, 19: *Chaetoceros* resting spore, 20: *Cyclotella litoralis*, and 21: *Tryblionella lanceola* (provided by Dr. Takashi Chiba).

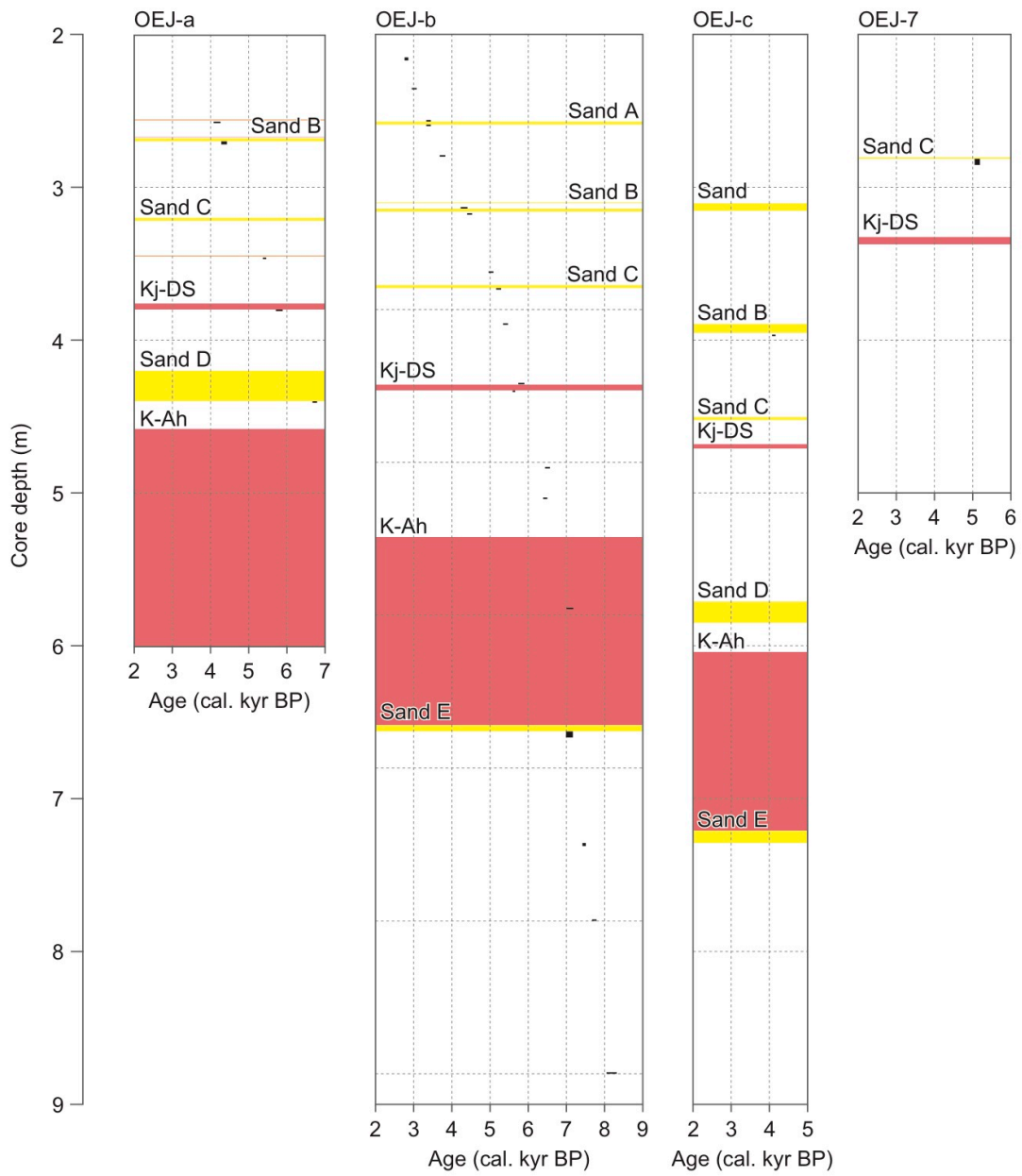


Fig. 4-18. Radiocarbon ages of leaves, seeds, insect remains, and shell fragments obtained from the cores in the Oh-enji marsh (conducted by the Geo Science Laboratory Co. Ltd.).

Table 4-1. Main mineral and range of refractive index of the volcanic glass shards and orthopyroxene grains of the samples collected at 430–433 cm and 630–635 cm deeps in the core OEJ-b (conducted by Kyoto Fission-track Co. Ltd.). The data of standard samples of K-Ah and Kj-DS are also shown (Machida and Arai, 1978; Kamata and Kobayashi, 1997; Furusawa and Umeda, 2000).

Core	Depth (cm)	Main material	Range of refractive index (mode)		Note
			Volcanic glass	Opx	
OEJ-b	430–433	Opx, Cpx, Opq	1.5042–1.5184	1.700–1.703	This study
			1.5283–1.5400 (1.537–1.538) 1.5441–1.5441	1.704–1.708 (1.706–1.707) 1.709–1.714 (1.711–1.712) 1.715–1.717	
OEJ-b	630–635	Opq, Opx, Cpx, Ap	1.4993–1.5029 1.5103–1.5166 (1.511) 1.5196–1.5378	N/A	This study
K-Ah*	N/A	Opx, Cpx	1.508–1.516	1.708–1.713	Machida and Arai (1978)
Kj-DS*	N/A	Opx, Cpx	1.5351–1.5417	N/A	Kamata and Kobayashi (1997) Furusawa and Umeda (2000)

*Standard sample

Table 4-2. Mud content, mean grain size, and sorting of the sand layers, gravel layers, and beach sand at the Oh-enji marsh.

Core	Depth (cm)	Sand no.	Mud content (%)	Mean grain size (phi)	Sorting
OEJ-a	255–256	N/A	N/A	-1.84	0.49
	268–269	Sand layer B	N/A	1.74	0.65
	320–322	Sand layer C	N/A	1.38	0.61
	344–345	N/A	N/A	-1.56	1.13
	420–422	Sand layer D	93.2	2.89	0.81
	422–424	Sand layer D	89.2	2.36	1.02
	424–426	Sand layer D	70.1	1.67	1.86
	426–428	Sand layer D	74.0	2.14	1.10
	428–430	Sand layer D	81.4	3.16	0.71
	430–432	Sand layer D	82.4	3.14	0.84
	432–434	Sand layer D	82.3	3.31	0.54
	434–436	Sand layer D	95.9	3.18	0.76
	436–438	Sand layer D	83.0	2.93	0.84
	438–440	Sand layer D	74.3	2.96	0.79
420–440	Sand layer D (bulk)	82.6	2.77	1.11	
OEJ-b	257–259	Sand layer A	N/A	-0.18	1.35
	315–316	Sand layer B	N/A	1.62	0.61
	363–366	Sand layer C	N/A	1.02	0.44
	651–652	Sand layer E	N/A	2.12	0.95
	652–653	Sand layer E	N/A	0.79	1.42
	653–654	Sand layer E	N/A	0.38	1.15
	654–655	Sand layer E	N/A	-0.24	1.44
	651–655	Sand layer E (bulk)	N/A	0.76	1.53
OEJ-c	314–317	N/A	N/A	-1.21	1.60
	392–394	Sand layer B	N/A	0.58	1.64
	450–452	Sand layer C?	N/A	1.59	0.77
	571–573	Sand layer D	30.9	2.76	0.78
	573–575	Sand layer D	30.5	2.80	0.75
	575–577	Sand layer D	41.9	2.95	0.79
	577–579	Sand layer D	47.8	2.93	0.78
	579–581	Sand layer D	32.0	3.02	0.70
	581–583	Sand layer D	28.0	2.79	0.72
	583–585	Sand layer D	61.9	2.98	0.74
	571–585	Sand layer D (bulk)	39.0	2.89	0.76
	721–723	Sand layer E	N/A	0.91	1.00
	723–725	Sand layer E	N/A	1.10	0.88
	725–727	Sand layer E	N/A	1.28	0.93
	727–729	Sand layer E	N/A	1.24	0.95
721–729	Sand layer E (bulk)	N/A	1.13	0.95	
Beach sand	N/A	N/A	N/A	1.82	0.57

Table 4-3. Mineral composition of the sand layers A–E and beach sand at the Oh-enji marsh. A total of 100 grains were measured in each sample.

Core	Depth (cm)	Sand no.	Quartz	Feldspar	Pyroxene	Hornblende	Magnetite	Rock fragment	Volcanic glass
OEJ-b	257–259	Sand layer A	24	58	N/A	6	1	11	N/A
	315–316	Sand layer B	27	57	5	N/A	1	10	N/A
	363–366	Sand layer C	1	4	3	N/A	N/A	92	N/A
	651–655	Sand layer E	1	14	N/A	N/A	1	13	71
OEJ-c	571–585	Sand layer D	5	21	3	3	N/A	65	3
Beach sand	N/A	N/A	26	27	14	3	N/A	30	N/A

Table 4-4. Radiocarbon ages of leaves, seeds, insect remains, and shell fragments obtained from the cores in the Oh-enji marsh (conducted by the Geo Science Laboratory Co. Ltd.).

Running no.	Core	Depth (cm)	Material	Conventional age (¹⁴ C yr BP)	Range of 2 sigma (cal. yr BP)*	Lab no. (Beta-)
1	OEJ-a	257–258	leaves, seeds	3790±30	4080–4260	427529
2	OEJ-a	270–272	leaves, seeds	3920±30	4280–4430	428317
3	OEJ-a	346–347	leaves, seeds	4640±30	5370–5460	427531
4	OEJ-a	380–381	leaves, seeds	5030±30	5710–5890	427532
5	OEJ-a	440–441	leaves, seeds	5910±30	6670–6790	427533
6	OEJ-b	215–217	leaves, seeds, insects	2710±30	2760–2860	428318
7	OEJ-b	235–236	seeds	2900±30	2950–3080	427535
8	OEJ-b	256–257	seeds	3150±30	3330–3450	427536
9	OEJ-b	259–260	leaves, seeds	3150±30	3330–3450	427537
10	OEJ-b	279–280	leaves	3460±30	3680–3830	427538
11	OEJ-b	313–314	leaves, seeds	3870±30	4230–4410	427539
12	OEJ-b	317–318	leaves, seeds	3980±30	4400–4530	427540
13	OEJ-b	355–356	seeds	4450±30	4960–5090	427541
14	OEJ-b	366–367	leaves, seeds	4470±30	5160–5290	431259
15	OEJ-b	389–390	leaves, seeds	4650±30	5340–5470	427542
16	OEJ-b	428–429	leaves	5060±30	5740–5900	427543
17	OEJ-b	433–434	leaves, seeds	4900±30	5590–5660	427544
18	OEJ-b	483–484	leaves, seeds	5720±30	6440–6570	427545
19	OEJ-b	503–504	leaves, seeds	5650±30	6390–6500	427546
20	OEJ-b	575–576	leaves, seeds	6200±30	7000–7180	427547
21	OEJ-b	656–660	leaves	6180±30	6990–7170	427548
22	OEJ-b	729–731	leaves, seeds	6530±30	7420–7510	427549
23	OEJ-b	779–780	leaves, seeds	6900±30	7670–7790	427550
24**	OEJ-b	879–880	shell fragments	7680±30	8050–8320	427551
25	OEJ-c	396–397	leaves, seeds	3750±30	4070–4160	447386
26	OEJ-7	281–285	leaves, seeds	4540±30	5050–5190	447385

*Ages were converted using the calibration program CALIB 7.1.

**Age was corrected in consideration of a local marine reservoir based on Hirabayashi et al. (2017).

4.2. Nokinoi lowland

4.2.1. Stratigraphy, sedimentary characteristics, and radiocarbon ages

The sediment cores of HJ-1, 2, and 7 collected at the seaward sites, are composed of a surface agricultural soil and a layer of muddy sand with gravels (Figs. 2-4 and 4-19). In contrast to them, up to 200 cm sediment cores (HJ-3, 4, 5, 6, 8, and 9) obtained at the landward side beyond the road are composed of four units of basal dark-gray muddy sand with gravels, brown silt, dark brown organic-rich mud, and upper agricultural soil, in ascending order (Figs. 4-19 and 4-20).

There is a sand layer at 104–116 cm deep in the core HJ-4 which is located at 679 m from shoreline (Figs. 4-19, 4-20, 4-21, and Table 3-2). The sand layer exhibits sharp upper and lower contacts with the surrounding mud layers, and the upper sediment is dark-brown organic-rich mud whereas the lower sediment is silt with few organic matters (Figs. 4-19, 4-20 and 4-21). There is a 2 cm diameters silt clast at the center of the sand layer which is similar to the silt below the sand layer (Fig. 4-21). The mud content of this 12-cm-thick sand layer is 58.9% in the average of 1 cm-interval samples, and the sand layer is composed mainly of very fine to fine sand showing grading structure at the lower part of the deposit (Fig. 4-22 and Table 4-5). While there is almost no variation in the middle part, the top section is characterized by relatively coarser sediments (Fig. 4-22 and Table 4-5). The grain size distribution of this sand layer is compared to sediments of modern tidal flat and beach that are potential source areas (Figs. 2-4, 4-22, and 4-23). The sand layer in the core HJ-4 is composed of poorly-sorted finer grains than those of beach and tidal flat (Figs. 4-22, 4-23, and Table 4-5). The mineral composition of the sand layer in the core HJ-4, consisting of feldspar, rock fragment, pyroxene, quartz, hornblende, and magnetite, is similar to that of modern tidal flat and beach sand (Table. 4-6).

The intersite comparison of the sand layer that occurs in the core HJ-4, is conducted by sedimentary

facies and appearance depths as well as radiocarbon ages. The radiocarbon ages are dated to 590–640 cal. yr BP at the top of the organic-rich mud layer and 1880–2000 cal. yr BP at immediately above the sand layer in the core HJ-4 (Figs. 4-19, 4-20, and Nos. 28 and 29 in Table 4-7). A sand layer characterized by a sub-layer structure is evident in the organic-rich mud layer in the core HJ-4 (138–139 cm deep). The upper and lower contacts of the sand layer are unclear, and patchy sand grains are included in the upper and lower mud layers. The radiocarbon age of 4520–4650 cal. yr BP is obtained at 139–141 cm deep (Figs. 4-19, 4-20, and No. 27 in Table 4-7). Sand layer is recognized at the boundary between the organic-rich mud and the silt layer in the cores HJ-5 (9 cm in thickness) and HJ-6 (2 cm in thickness), and this layer shows inland thinning trend, including that which is evident in the core HJ-4 (Figs. 4-19 and 4-20). Fragments of leaves collected at 94–96 cm deep in the core HJ-5 is dated to 3240–3390 cal. yr BP (Figs. 4-19, 4-20, and No. 30 in Table 4-7). There is a large difference in depositional age among each sand layer observed in the cores HJ-3–5. There is no sand layer in organic-rich mud in the cores obtained from the transect B–B' (Figs. 2-4, 4-19, and 4-20).

4.2.2. Magnetic susceptibility and geochemical signatures

The profiles of magnetic susceptibility, chemical compositions, and Mo Inc/Mo Coh ratio at 101–167 cm deep of the core HJ-4' are divided into four groups; sand with gravels and plant fragments at 161–167 cm depth, silt at 135–158 cm depth, sand at 116–135 cm depth, and organic-rich mud at 101–116 cm depth (Fig. 4-24). The sand at 116–135 cm depth is characterized by lower Mo Inc/Mo Coh ratio and higher magnetic susceptibility associated with higher counts of Ti and Fe, as well as Si, S, K, Ca, V, Mn, Sr, and Ba than in the overlying organic-rich mud and underlying silt (Fig. 4-24).

Although there is no significant difference in the profile of Mo Inc/Mo Coh ratio between the organic-

rich mud and silt, the magnetic susceptibility associated with higher counts of Ti and Fe is higher in the organic-rich mud than the silt. The profiles of S, K, Ca, Mn, and Sr display higher value in the organic-rich mud than the silt, while that of Cr, Rb, and Zr shows lower value (Fig. 4-24). The PCA result shows these trends more clearly with two principal components which explain 62% of the variance (PC1: 37% and PC2: 25%; Fig. 4-25). The muddy sand layer is characterized by higher counts of S and Br (Figs. 4-24 and 4-25).

4.2.3. Diatoms

The fossil diatom assemblages are examined at 89–170 cm depth of the core HJ-4 and indicate that the sediments at the lowland record an overall change from marine to freshwater environments (Figs. 4-26 and 4-27). The sandy mud at 148–175 cm depth is characterized by an appearance of brackish–marine and marine diatoms such as *Melosira moniliformis* (No. 8 in Fig. 4-28), *Nitzschia inconspicua*, *Planthidium delicatulum* (No. 9 in Fig. 4-28), and *Paralia sulcata* (No. 10 in Fig. 4-28), while freshwater and freshwater–brackish diatoms are uncommon. In the silt at 116–148 cm depth on the other hand, fossil diatom assemblages are mainly composed of freshwater and freshwater–brackish species with less than 10% of brackish–marine species such as *Bacillaria paxillifer* and *Melosira moniliformis* (Figs. 4-26, 4-27, and Nos. 6 and 8 in Fig. 4-28). The fossil diatom assemblage in the organic-rich mud layer is dominated by freshwater and freshwater–brackish, but few brackish–marine species are observed at 102–103 cm depth immediately above the sand layer. It is noteworthy that the freshwater diatoms *Rhopalodia operculata* (No. 1 in Fig. 4-28), *Staurosira construens* (No. 2 in Fig. 4-28), and *Staurosirella pinnata* (No. 3 in Fig. 4-28) occur in the organic-rich mud although they are absent in the silt (Fig. 4-26).

Focusing on the sand layer which lies between the organic-rich mud and silt, freshwater–brackish diatoms *Pseudostaurosira brevistriata* (No. 4 in Fig. 4-28), brackish–marine diatoms such as *Amphora*

arenicola (No. 5 in Fig. 4-28), *Bacillaria paxillifer* (No. 6 in Fig. 4-28), *Diploneis smithii* (No. 7 in Fig. 4-28), *Melosira moniliformis* (No. 8 in Fig. 4-28), *Planothidium delicatulum* (No. 9 in Fig. 4-28), and marine diatoms *Paralia sulcata* (No. 10 in Fig. 4-28) are characteristically observed despite that they are not observed at the overlying organic-rich mud and underlying silt except for some species which occur immediately above the sand layer (Fig. 4-26). The abundance of brackish–marine diatoms increases at the sand layer compared to the overlying organic-rich mud and underlying silt (Fig. 4-27).

4.2.4. Boulder distribution

Hundreds of boulders are mostly concentrated in southern part of the sandy beach (Fig. 2-5). About 90% of the measured 243 boulders are composed of andesite and 10% are conglomerate, and almost all boulders are rounded (Figs. 4-29, 4-30, and Table 4-8). The wet density of the andesite boulder HJ-B2 is 2.6 g/cm^3 (Fig. 4-30c). The heaviest rock boulder HJ-B1 is estimated to weigh approximately 119 t (4.0 m \times 3.8 m \times 3.0 m) (Fig. 4-30b), but the weight of the other boulders is less than 100 t (Fig. 4-29 and Table 4-8). The maximum boulder weight decreases with distance from the shoreline along P–P' (Fig. 4-29). The andesite boulder HJ-B2 is mainly composed of orthopyroxene, clinopyroxene, and plagioclase, with a vesicular texture in the groundmass (Fig. 4-31). These features are consistent with the Akisada pyroclastic flow deposits that is distributed behind of the boulder site (Fig. 2-5; Ishizuka et al., 2005).

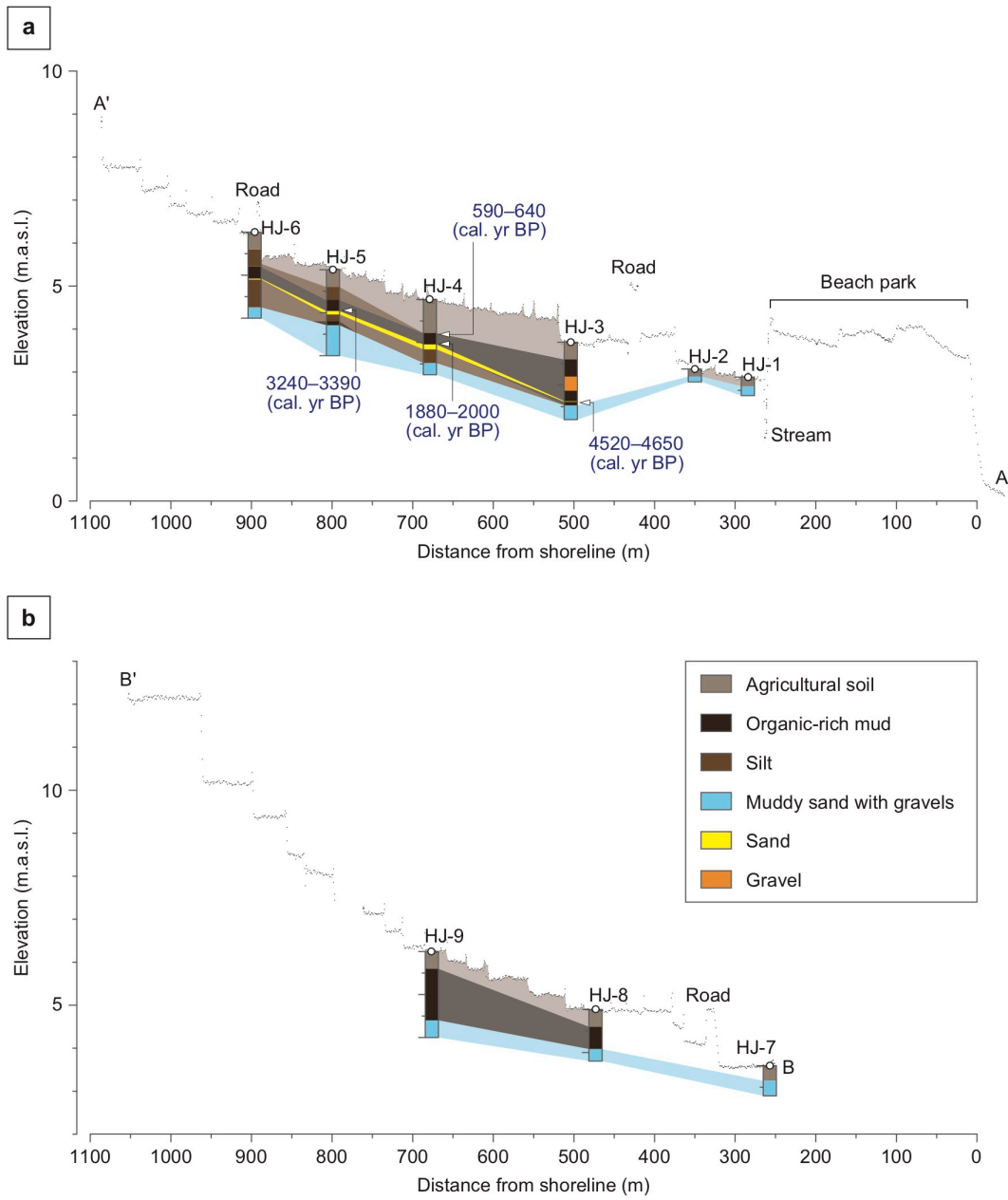


Fig. 4-19. Cross-sections of sedimentary columns along the transect A–A' and B–B' in the Nokinoi lowland. Radiocarbon ages are also shown (conducted by the Geo Science Laboratory Co. Ltd.).

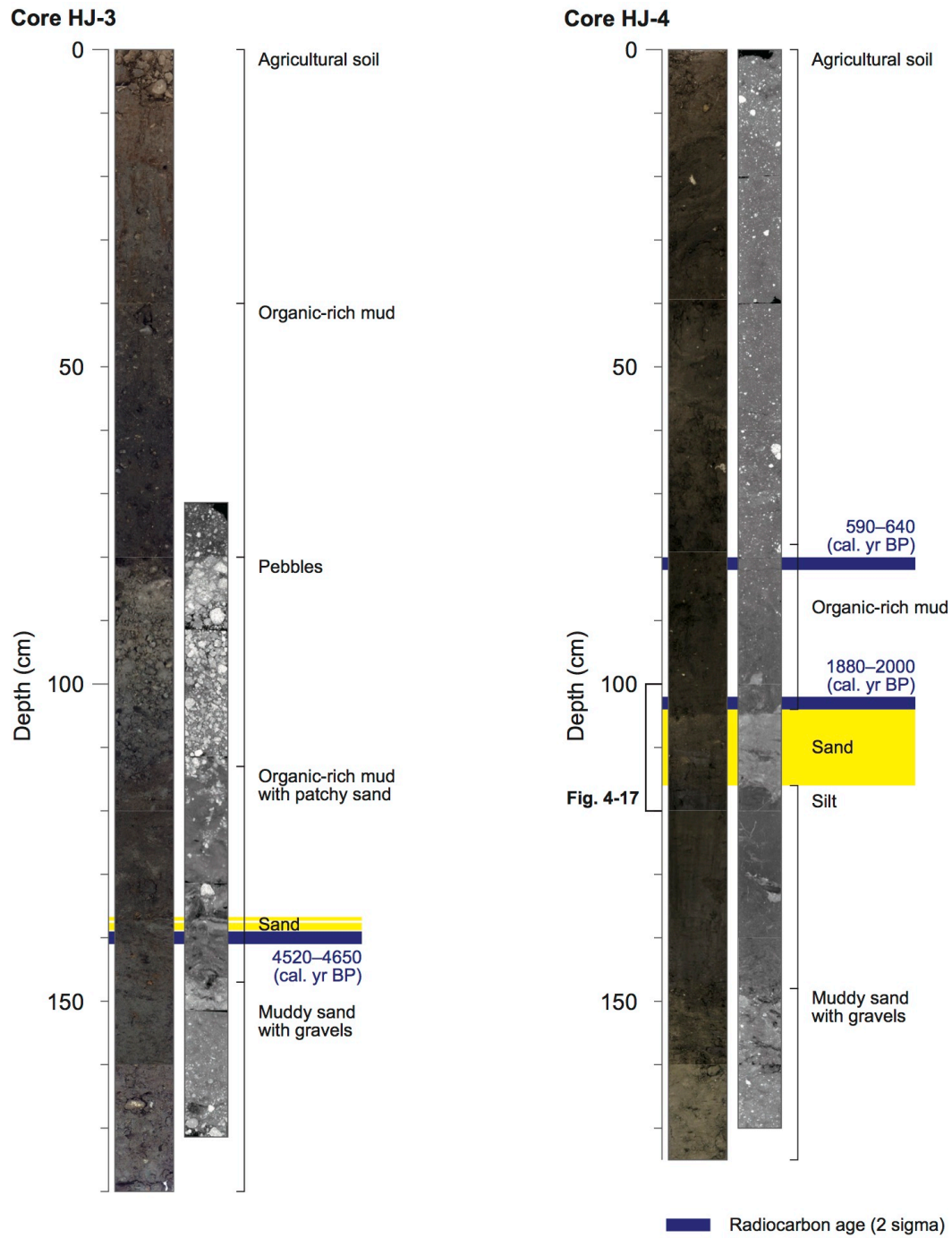


Fig. 4-20. Photograph and CT image of the sediment cores obtained from the Nokinoi lowland. Sedimentary facies, sand layers, and radiocarbon ages (conducted by the Geo Science Laboratory Co. Ltd.) are shown on the right side of the CT image or core photograph.

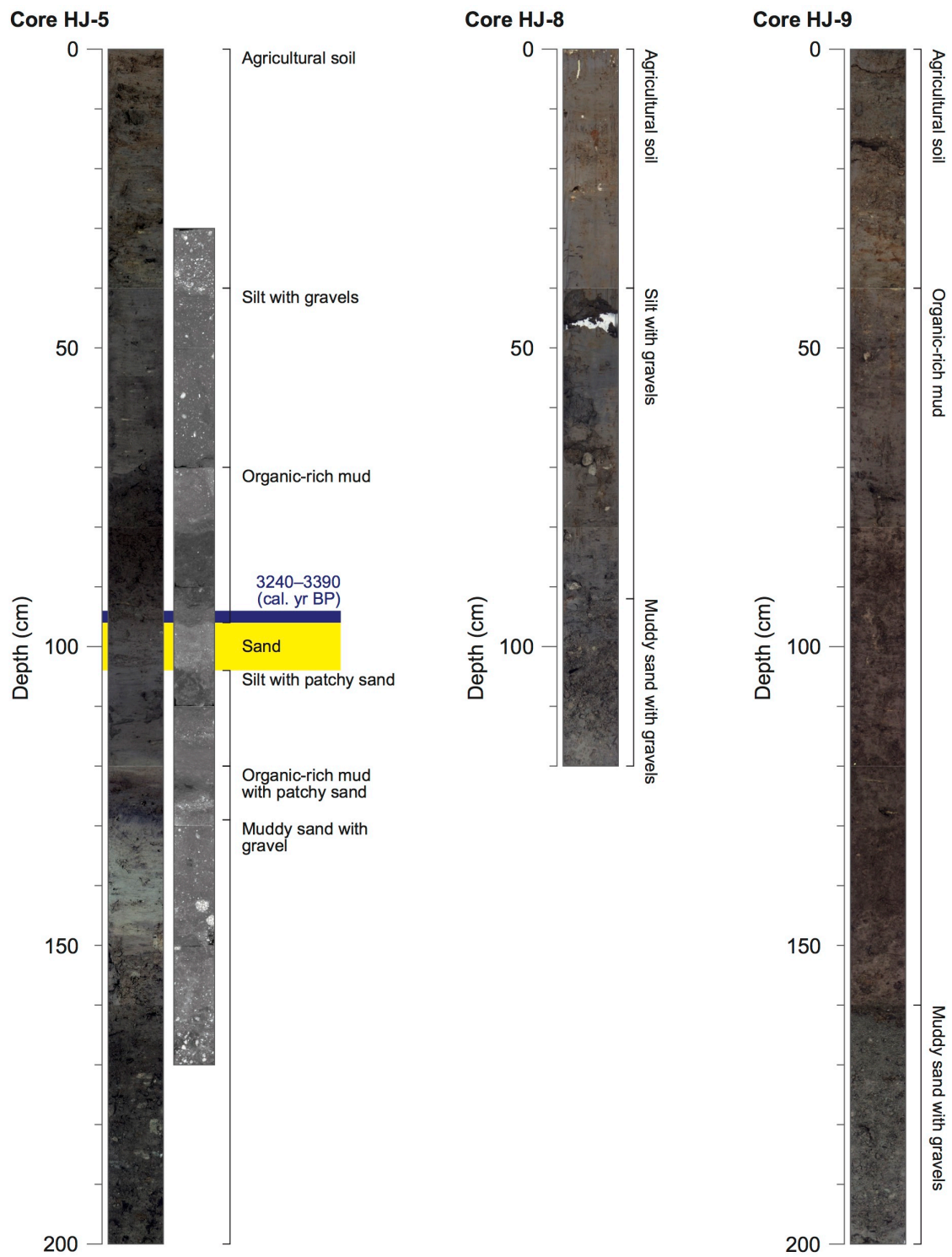


Fig. 4-20. (continued)

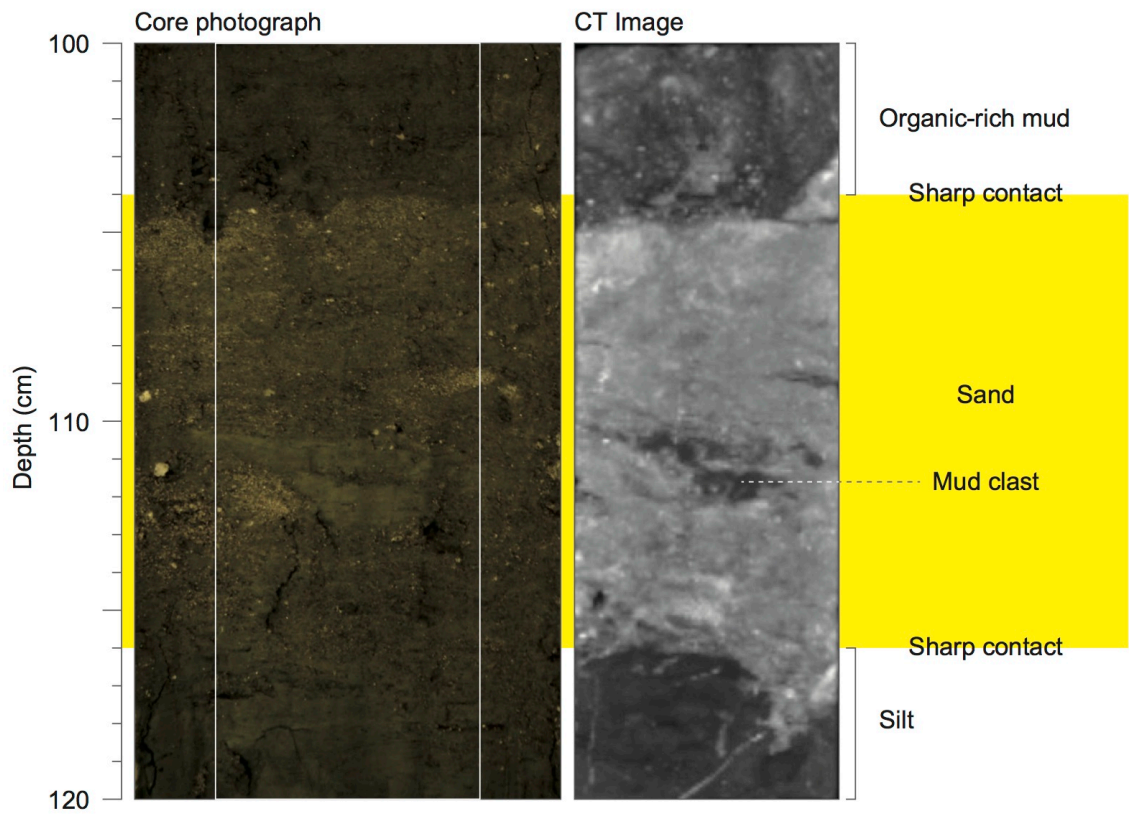


Fig. 4-21. Enlarged photograph and CT image of the sediments occur at 100–120 cm deep in the core HJ-4.

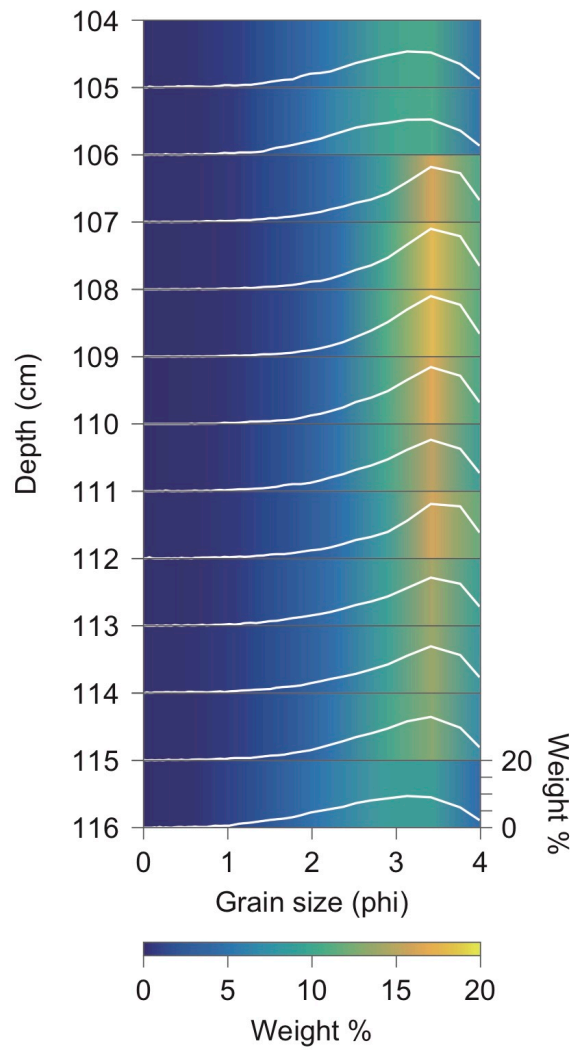


Fig. 4-22. Vertical variation in grain size distribution of the sand layer evident in 104–116 cm deep in the core HJ-4.

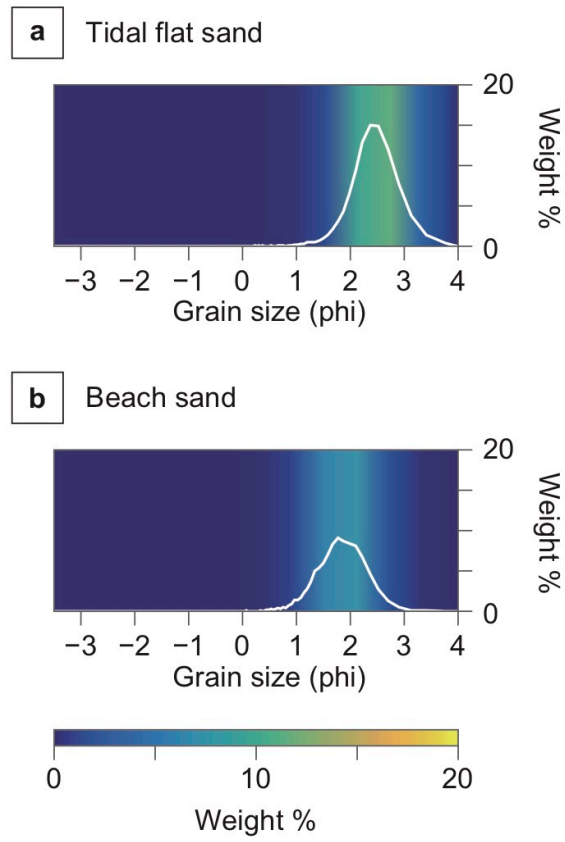


Fig. 4-23. Grain size distribution of the sand grains obtained from (a) tidal flat and (b) beach (see Fig. 2-4).

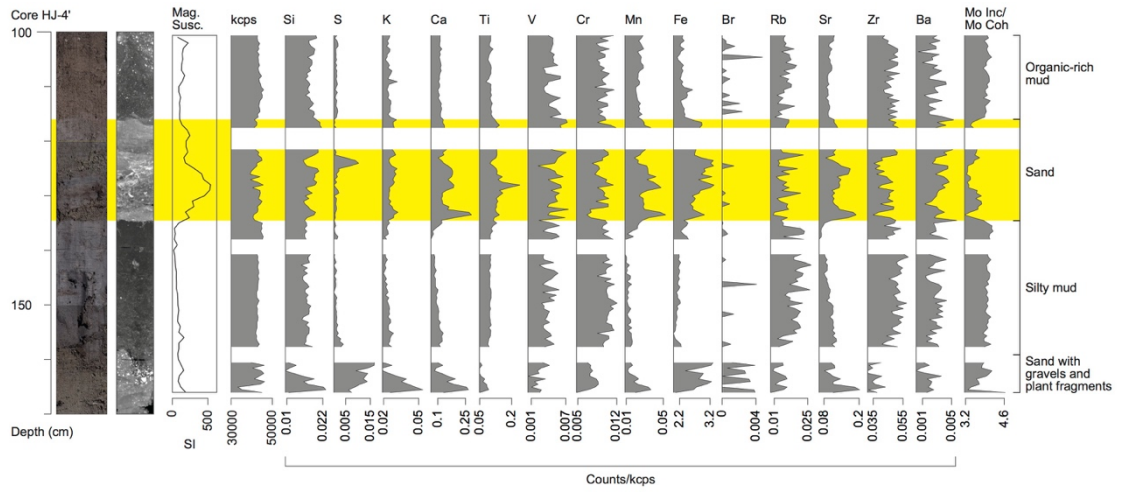


Fig. 4-24. Magnetic susceptibility (Mag. Susc.) and ITRAX data of the depth of 101–167 cm in the core HJ-4'. All ITRAX data, except for Mo Inc/Mo Coh, are normalized over kcps.

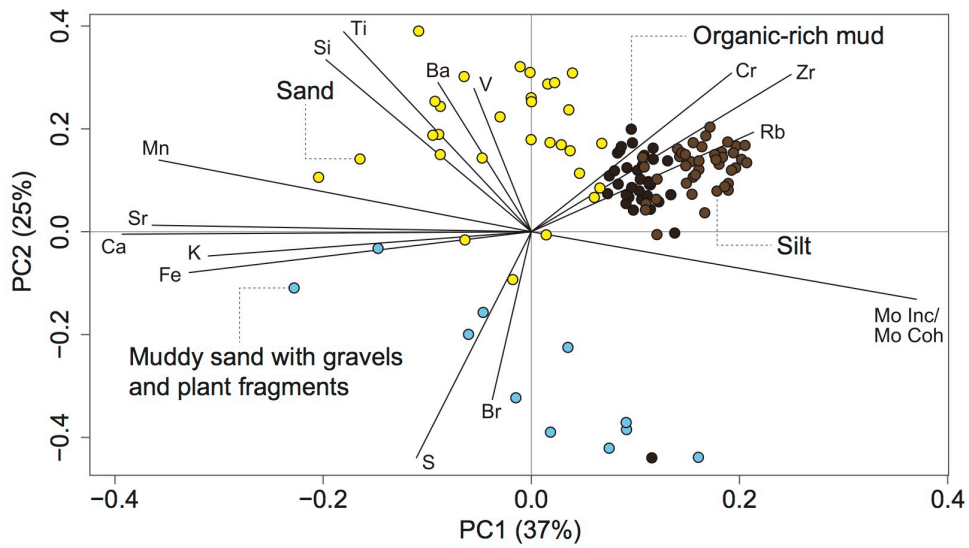


Fig. 4-25. Scores and loading of the PCA of normalized XRF data from 101–167 cm deep in the core HJ-4' (provided by Dr. Catherine Chagué-Goff). Each color of dot corresponds to that of Fig. 4-19; muddy sand with gravels and plant fragments (161–167 cm deep, blue), silt (135–158 cm deep, brown), sand (116–135 cm deep, sand), and organic-rich mud (101–116 cm deep, dark brown).

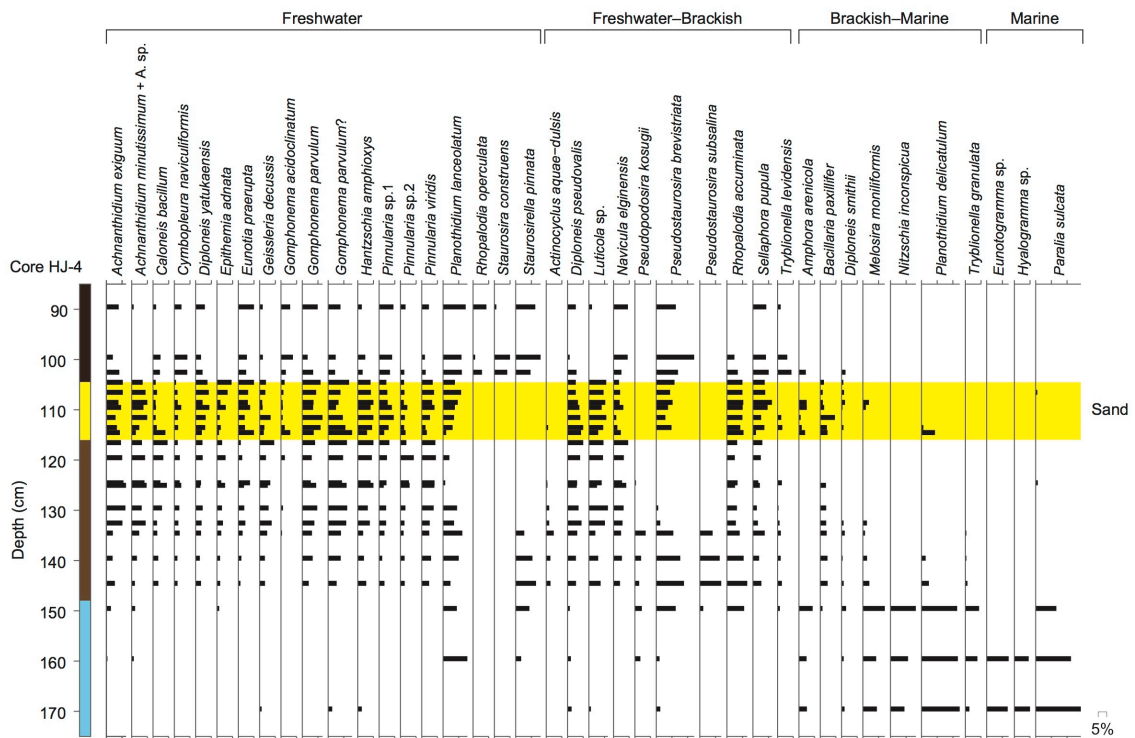


Fig. 4-26. Fossil diatom assemblages in the core HJ-4 (provided by Dr. Takashi Chiba). A color coding of the column corresponds to that of Fig. 4-19.

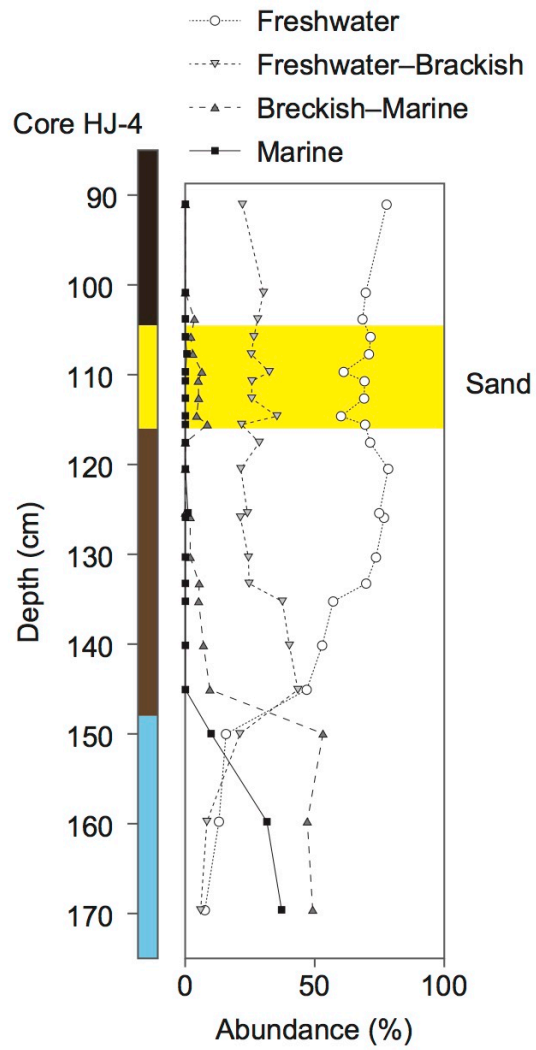


Fig. 4-27. Abundance of freshwater, freshwater-brackish, brackish-marine, and marine diatoms in the core HJ-4 (provided by Dr. Takashi Chiba). A color coding of the column corresponds to that of Fig. 4-19.

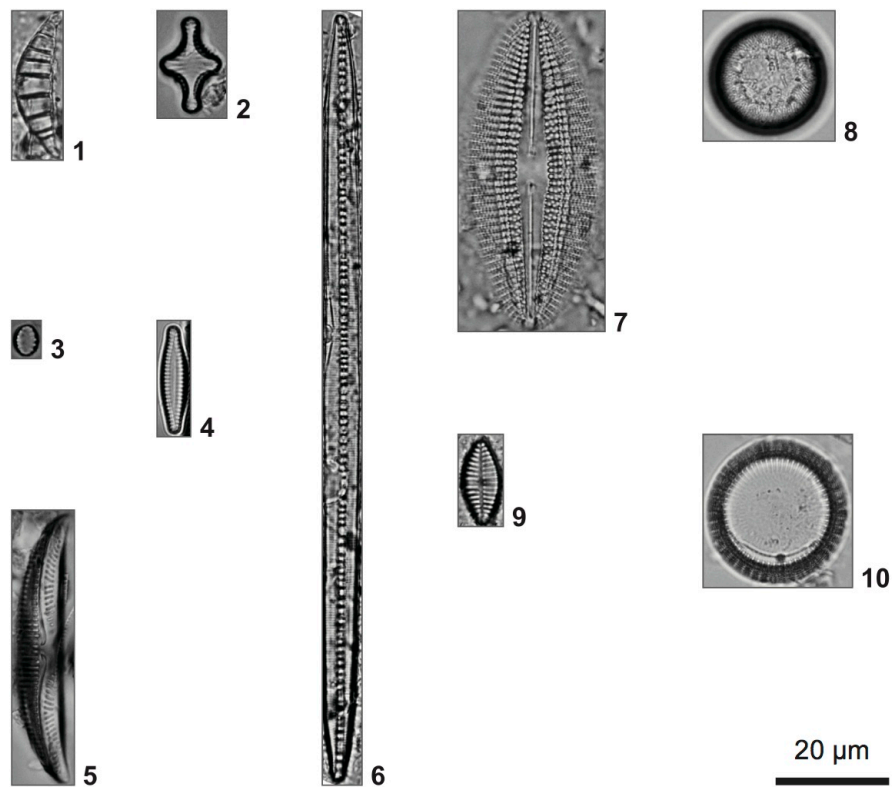


Fig. 4-28. Micrographs of typical diatoms in the core HJ-4. 1–3: Freshwater species, 4: Freshwater–Brackish species, 5–9: Brackish–Marine species, and 10: Marine species; 1: *Rhopalodia operculata*, 2: *Staurosira construens*, 3: *Staurosirella pinnata*, 4: *Pseudostaurosira brevistriata*, 5: *Amphora arenicola*, 6: *Bacillaria paxillifer*, 7: *Diploneis smithii*, 8: *Melosira moniliformis*, 9: *Planothidium delicatulum*, and 10: *Paralia sulcata* (provided by Dr. Takashi Chiba).

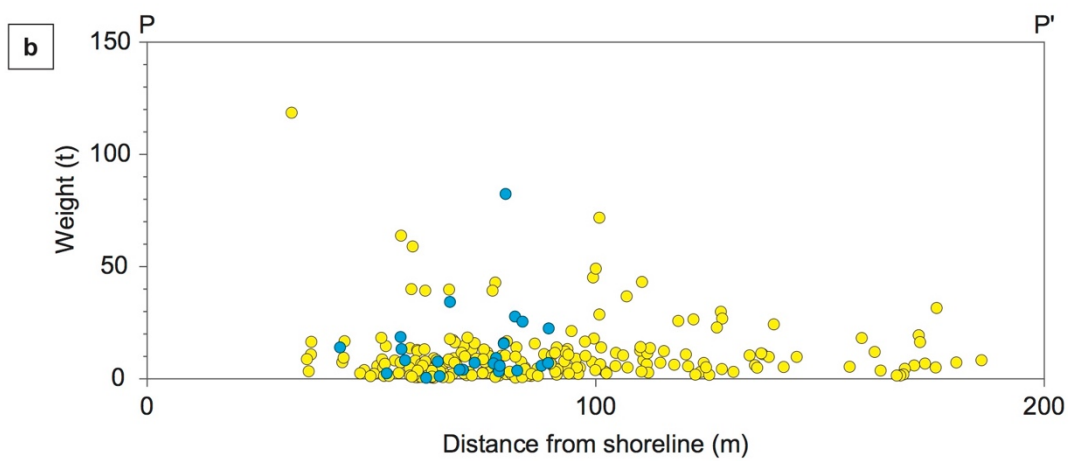
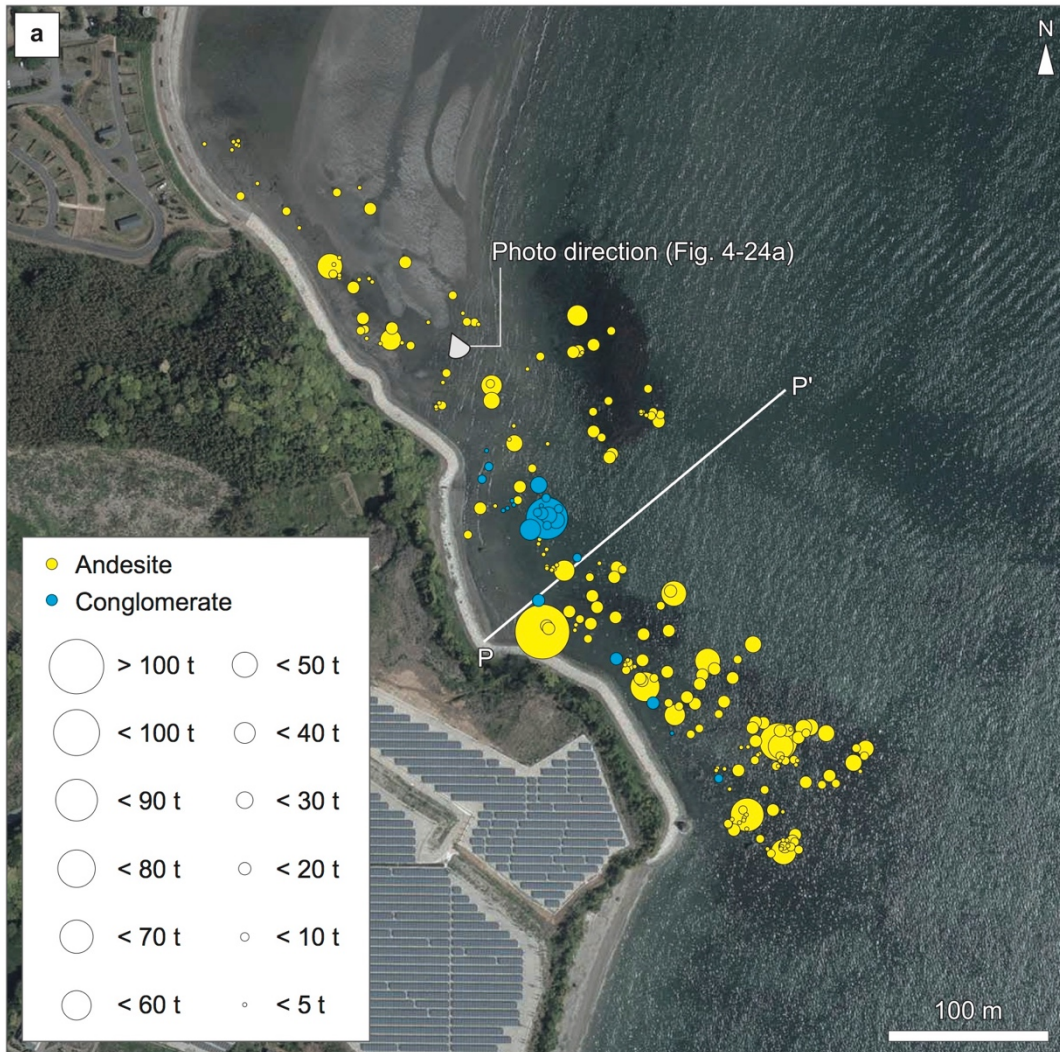


Fig. 4-29. (a) Locations, sizes, and types of the boulders in the study area. (b) Relationship between the distance from shoreline and boulder weight along P–P'.

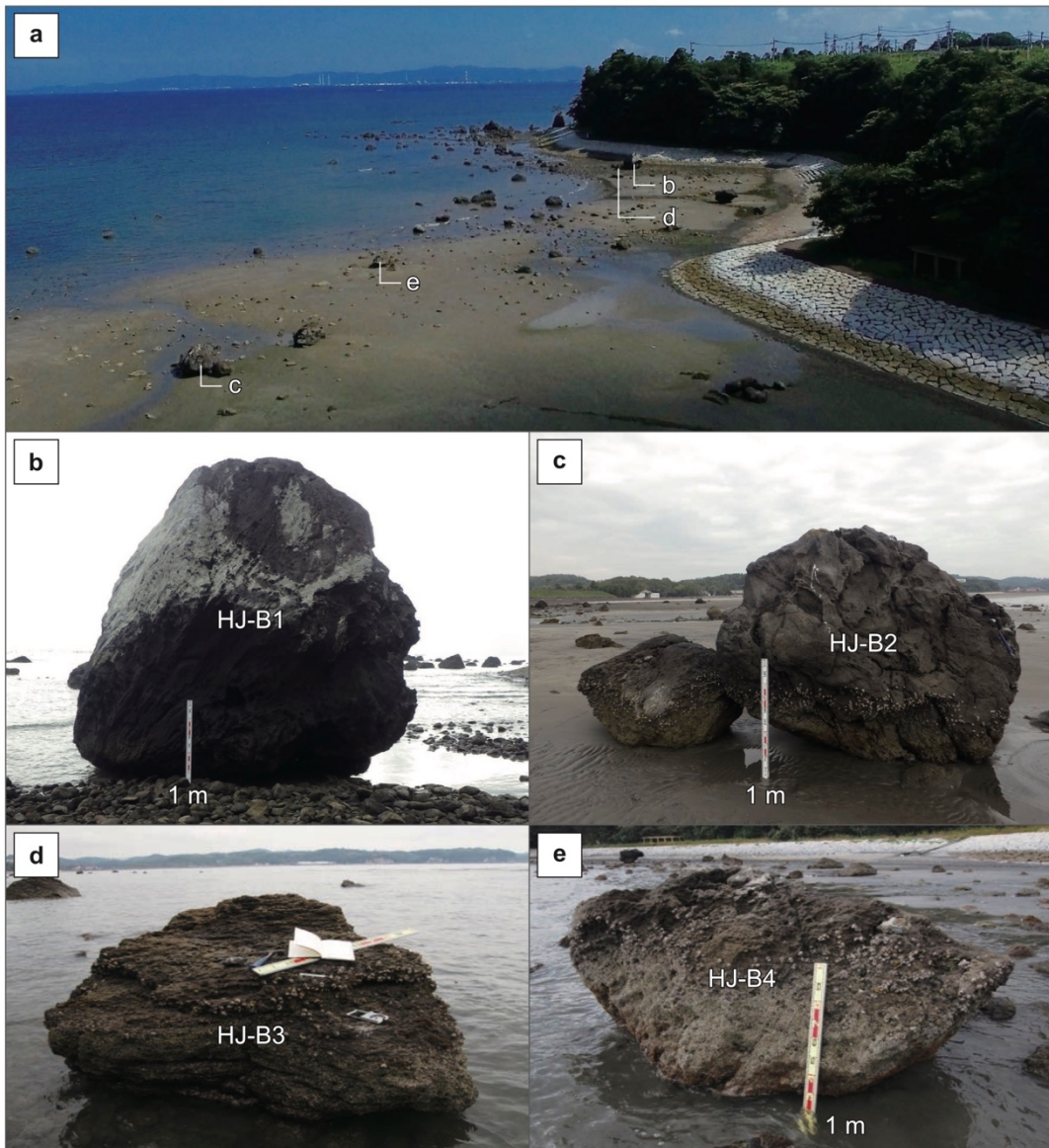


Fig. 4-30. (a) Photograph showing boulders on the sandy tidal flat at the shore of the Nokinoi lowland. (b) Andesite boulder HJ-B1 (4.0 m×3.8 m×3.0 m, 118.6 t, scale = 1 m). (c) Andesite boulder HJ-B2 (2.8 m×2.3 m×2.2 m, 36.8 t, scale = 1 m). (d) Andesite boulder HJ-B3 (2.4 m×2.2 m×1.2 m, 16.5 t, scale = 1 m). (e) Andesite boulder HJ-B4 (3.0 m×2.1 m×1.3 m, 21.3 t, scale = 1 m).

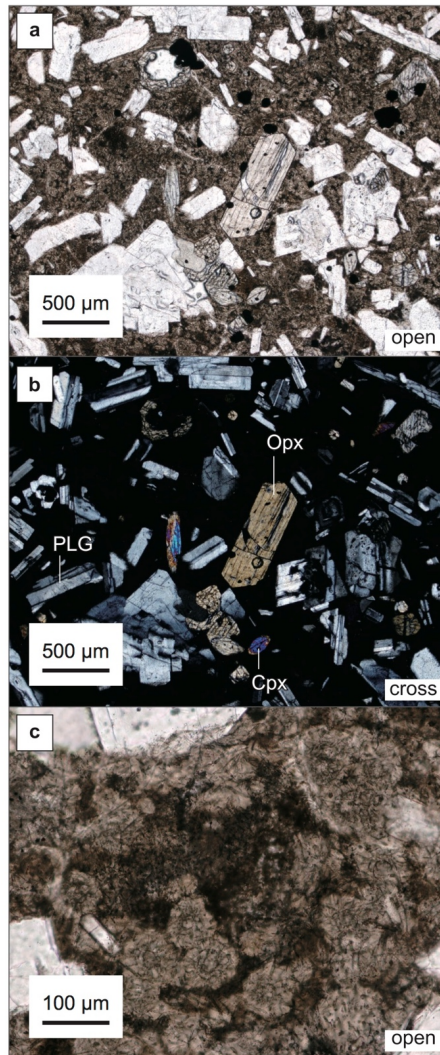


Fig. 4-31. Photomicrographs of the andesite boulder named HJ-B2 under (a) open nicol and (b) cross nicol. (c) Vesicular texture in the groundmass (open nicol). Opx, Cpx, and PLG are short of orthopyroxene, clinopyroxene, and plagioclase (provided by Kohei Tominaga).

Table 4-5. Mud content, mean grain size, and sorting of the sand layer in the core HJ-4, tidal flat sand, and beach sand at the Nokinoi lowland.

Core	Depth (cm)	Mud content (%)	Mean grain size (phi)	Sorting
HJ-4	104–105	66.6	2.47	0.90
	105–106	55.0	2.55	0.80
	106–107	57.2	2.81	0.88
	107–108	55.6	2.93	0.82
	108–109	56.3	2.96	0.76
	109–110	48.6	2.91	0.75
	110–111	66.6	2.78	0.85
	111–112	69.6	2.80	0.97
	112–113	51.4	2.73	0.89
	113–114	52.6	2.60	1.00
	114–115	59.1	2.61	0.91
	115–116	68.7	2.42	0.83
		104–116 (bulk)	58.9	2.72
Tidal flat sand	N/A	N/A	2.32	0.47
Beach sand	N/A	N/A	1.71	0.46

Table 4-6. Mineral composition of the sand layer in the core HJ-4, tidal flat sand, and beach sand at the Nokinoi lowland. A total of 100 grains were measured in each sample.

Core	Depth (cm)	Quartz	Feldspar	Pyroxene	Hornblende	Magnetite	Rock fragment	Volcanic glass
HJ-4	104-116	16	30	17	10	4	22	1
Tidal flat sand	N/A	10	33	13	N/A	1	43	N/A
Beach sand	N/A	25	24	3	N/A	N/A	47	1

Table 4-7. Radiocarbon ages of leaves and seeds obtained from the cores in Nokinoi lowland (conducted by the Geo Science Laboratory Co. Ltd.).

Running no.	Core	Depth (cm)	Material	Conventional age (¹⁴ C yr BP)	Range of 2 sigma (cal. yr BP)*	Lab no. (Beta-)
27	HJ-3	139-141	leaves	4090±30	4520-4650	426047
28	HJ-4	80-82	seeds	560±30	590-640	416766
29	HJ-4	102-104	seeds	1990±30	1880-2000	415768
30	HJ-5	94-96	leaves	3110±30	3240-3390	426046

*Ages were converted using the calibration program CALIB 7.1.

Table 4-8. Location, sizes, weight, and rock type of boulders.

Point no.	Latitude	Longitude	Long axis length (m)	Middle axis length (m)	Short axis length (m)	Volume (m ³)	Weight (t)	Rock type*
12	33.363305	131.595819	1.2	0.8	0.7	0.7	1.7	A
13	33.363272	131.596004	1.0	0.7	0.6	0.4	1.1	A
14	33.363300	131.596032	1.1	0.8	0.7	0.6	1.6	A
15	33.363294	131.596048	1.1	0.8	0.5	0.4	1.1	A
16	33.363317	131.596014	1.0	0.8	0.8	0.6	1.7	A
17	33.363323	131.596045	1.2	1.0	0.9	1.1	2.8	A
18	33.363083	131.596175	1.4	0.9	0.8	1.0	2.6	A
19	33.363012	131.596061	1.8	1.7	0.7	2.1	5.6	A
20	33.362927	131.596369	2.2	1.5	1.2	4.0	10.3	A
21	33.362833	131.596455	1.2	0.8	0.6	0.6	1.5	A
22	33.362941	131.596932	2.0	1.5	1.4	4.2	10.9	A
23	33.363059	131.596860	1.5	1.0	0.8	1.2	3.1	A
24	33.363032	131.596707	2.1	1.7	0.9	3.2	8.4	A
25	33.362665	131.596725	1.2	0.7	0.6	0.5	1.3	A
26	33.362626	131.596687	2.0	1.0	0.4	0.8	2.1	A
27	33.362617	131.596660	3.0	2.5	2.2	16.5	42.9	A
28	33.362573	131.596682	1.5	1.2	1.1	2.0	5.1	A
29	33.362565	131.596724	1.5	1.0	0.7	1.1	2.7	A
30	33.362552	131.596725	1.0	0.6	0.6	0.4	0.9	A
149 (HJ-B1)	33.360560	131.598086	4.0	3.8	3.0	45.6	118.6	A
150 (HJ-B3)	33.360579	131.598129	2.4	2.2	1.2	6.3	16.5	A
151	33.360593	131.598114	2.0	1.5	1.4	4.2	10.9	A
152	33.360561	131.598138	1.2	1.1	1.0	1.3	3.4	A
153	33.360674	131.598267	2.0	2.0	1.4	5.6	14.6	A
154	33.360599	131.598312	1.7	1.0	0.7	1.2	3.1	A
155	33.360631	131.598338	1.5	1.5	1.4	3.2	8.2	A
156	33.360569	131.598305	1.5	1.1	0.9	1.5	3.9	A
157	33.360606	131.598411	2.2	1.6	1.5	5.3	13.7	A
158	33.360521	131.598393	1.7	1.3	1.0	2.2	5.7	A
159	33.360737	131.598060	2.7	2.5	0.8	5.4	14.0	CG
160	33.361106	131.597586	1.8	1.7	1.1	3.4	8.8	A
161	33.361256	131.597669	2.4	2.1	1.4	7.1	18.3	A
162	33.361419	131.597682	1.8	1.5	1.1	3.0	7.7	CG
163	33.361490	131.597727	1.8	1.7	0.9	2.8	7.2	CG
164	33.361580	131.597712	1.8	0.9	0.8	1.3	3.4	CG
165 (HJ-B4)	33.361621	131.597898	3.0	2.1	1.3	8.2	21.3	A
166	33.361643	131.597865	1.4	1.2	1.1	1.8	4.8	A
167	33.361718	131.597895	1.8	1.3	0.7	1.6	4.3	A
168	33.361861	131.597745	3.0	2.3	1.6	11.0	28.7	A
169 (HJ-B2)	33.361946	131.597745	2.8	2.3	2.2	14.2	36.8	A
170	33.361956	131.597738	1.8	1.1	1.0	2.0	5.1	A
171	33.362039	131.597986	1.7	1.0	0.7	1.2	3.1	A
172	33.362109	131.598073	1.7	1.1	1.1	2.1	5.3	A
173	33.362290	131.597658	1.0	1.0	0.7	0.7	1.8	A
174	33.362301	131.597631	2.1	1.3	1.0	2.7	7.1	A
175	33.362304	131.597579	1.7	1.4	0.9	2.1	5.6	A
176	33.362353	131.597552	1.2	1.0	0.6	0.7	1.9	A
177	33.362453	131.597485	1.8	1.4	0.8	2.0	5.2	A
178	33.362301	131.597321	1.4	1.1	0.8	1.2	3.2	A
179	33.362170	131.597202	2.0	1.1	0.9	2.0	5.1	A

*A: andesite, CG: conglomerate

Table 4-8. (continued)

180	33.362016	131.597443	1.8	1.4	0.9	2.3	5.9	A
181	33.361963	131.597419	1.2	0.8	0.6	0.6	1.5	A
182	33.361848	131.597393	1.8	1.0	0.6	1.1	2.8	A
183	33.361826	131.597373	1.6	1.2	0.6	1.2	3.0	A
184	33.361834	131.597414	2.0	1.8	0.8	2.9	7.5	A
185	33.361816	131.597374	1.3	0.7	0.7	0.6	1.7	A
186	33.362186	131.597144	1.2	1.1	0.6	0.8	2.1	A
187	33.362203	131.597068	3.0	2.4	2.1	15.1	39.3	A
188	33.362269	131.597076	2.4	1.6	1.4	5.4	14.0	A
189	33.362182	131.596999	1.4	1.0	0.7	1.0	2.5	A
190	33.362210	131.596907	1.3	1.0	0.8	1.0	2.7	A/CG
191	33.362262	131.596896	1.9	1.4	0.9	2.4	6.2	A
192	33.362254	131.596866	1.7	1.6	1.0	2.7	7.1	A
193	33.362324	131.596882	2.8	1.5	1.2	5.0	13.1	A
194	33.362497	131.596817	3.0	1.8	1.2	6.5	16.8	A
195	33.362541	131.596856	1.7	1.0	0.5	0.9	2.2	A
196	33.362547	131.596923	1.1	1.1	0.6	0.7	1.9	A
197	33.362528	131.596945	1.8	1.0	0.9	1.6	4.2	A
198	33.362640	131.597166	2.3	1.6	1.3	4.8	12.4	A
214	33.362339	131.598321	2.7	2.5	1.8	12.2	31.6	A
215	33.362253	131.598548	2.0	1.6	1.0	3.2	8.3	A
216	33.362175	131.598430	2.2	2.0	1.7	7.5	19.4	A
217	33.362131	131.598354	2.0	1.2	0.6	1.4	3.7	A
218	33.362139	131.598328	2.2	2.1	1.0	4.6	12.0	A
219	33.362133	131.598293	2.5	2.0	1.4	7.0	18.2	A
220	33.361928	131.598795	1.8	1.3	1.2	2.8	7.3	A
221	33.361797	131.598829	1.7	1.4	1.1	2.6	6.8	A
222	33.361782	131.598878	1.5	1.3	1.0	2.0	5.1	A
223	33.361743	131.598867	3.0	1.5	1.4	6.3	16.4	A
224	33.361775	131.598817	1.7	1.5	0.9	2.3	6.0	A
225	33.361778	131.598784	1.3	1.2	1.1	1.7	4.5	A
226	33.361798	131.598760	1.2	0.9	0.7	0.8	2.0	A
227	33.361800	131.598748	1.3	0.9	0.5	0.6	1.5	A
228	33.361787	131.598750	1.1	0.9	0.6	0.6	1.5	A
229	33.361860	131.598529	1.9	1.1	1.0	2.1	5.4	A
230	33.361798	131.598426	1.9	1.8	1.1	3.8	9.8	A
231	33.361688	131.598429	1.8	1.8	1.3	4.2	11.0	A
232	33.361654	131.598484	2.1	1.5	1.2	3.8	9.8	A
233	33.361561	131.598553	2.1	1.9	1.1	4.4	11.4	A
234	33.361541	131.598536	1.7	1.7	1.4	4.0	10.5	A
235	33.360790	131.598947	2.3	1.5	1.4	4.8	12.6	A
236	33.360775	131.598968	3.5	2.5	1.9	16.6	43.2	A
237	33.360707	131.598880	1.7	1.7	1.0	2.9	7.5	A
238	33.360546	131.598765	2.2	2.0	1.4	6.2	16.0	A
239	33.360408	131.598583	3.0	1.7	1.0	5.1	13.3	CG
240	33.360490	131.599500	2.5	2.3	2.0	11.5	29.9	A
241	33.360396	131.599195	2.9	2.5	2.4	17.4	45.2	A
242	33.360352	131.599241	2.4	1.8	1.6	6.9	18.0	A
243	33.360301	131.599362	2.0	1.6	1.4	4.5	11.6	A
244	33.360405	131.599396	2.2	1.4	0.9	2.8	7.2	A
245	33.359823	131.600174	2.5	2.3	1.8	10.4	26.9	A
246	33.359775	131.600220	1.7	1.1	0.9	1.7	4.4	A

Table 4-8. (continued)

247	33.359706	131.600055	1.9	1.2	1.1	2.5	6.5	A
248	33.359750	131.600013	2.1	1.6	1.3	4.4	11.4	A
249	33.359700	131.599963	1.7	1.3	1.0	2.2	5.7	A
250	33.359714	131.599854	2.0	2.0	1.6	6.4	16.6	A
251	33.359835	131.599716	1.7	1.4	0.8	1.9	5.0	A
252	33.361135	131.598005	3.1	2.5	1.7	13.2	34.3	CG
253	33.361231	131.598053	2.2	1.8	0.9	3.6	9.3	CG
254	33.361270	131.598080	1.8	1.0	0.8	1.4	3.7	CG
255	33.361314	131.598112	1.9	1.5	0.8	2.3	5.9	CG
256	33.361386	131.598062	2.9	2.3	1.3	8.7	22.5	CG
257	33.361480	131.598018	1.8	1.4	1.2	3.0	7.9	A
258	33.361376	131.597936	2.0	2.0	1.0	4.0	10.4	A
259	33.361301	131.597922	2.1	1.5	1.1	3.5	9.0	A
260	33.361298	131.597883	2.0	1.3	0.6	1.6	4.1	CG
261	33.361274	131.597895	2.0	1.3	0.6	1.6	4.1	CG
262	33.361255	131.597852	1.3	0.7	0.5	0.5	1.2	CG
263	33.361243	131.597823	1.0	0.7	0.3	0.2	0.5	CG
264	33.361268	131.597770	1.0	0.7	0.4	0.3	0.7	A
265	33.361226	131.598082	2.4	2.1	1.2	6.0	15.7	CG
266	33.361233	131.598112	1.1	0.5	0.4	0.2	0.6	A
267	33.361244	131.598122	1.0	0.6	0.5	0.3	0.8	A
268	33.361252	131.598196	3.0	1.3	0.7	2.7	7.1	CG
269	33.361216	131.598127	3.5	1.8	1.7	10.7	27.8	CG
270	33.361198	131.598116	4.8	3.0	2.2	31.7	82.4	CG
271	33.361189	131.598179	3.5	2.0	1.4	9.8	25.5	CG
272	33.361159	131.598118	2.0	1.2	1.1	2.6	6.9	CG
273	33.361115	131.598094	1.1	0.8	0.7	0.6	1.6	A
274	33.361081	131.598068	1.2	1.0	0.7	0.8	2.2	A
275	33.361055	131.598061	1.1	0.9	0.6	0.6	1.5	A
276	33.361024	131.598114	1.0	0.7	0.4	0.3	0.7	A
277	33.360995	131.598095	1.0	0.7	0.3	0.2	0.5	A
278	33.360929	131.598116	1.3	0.8	0.6	0.6	1.6	A
279	33.360917	131.598116	1.0	0.6	0.5	0.3	0.8	A
280	33.360908	131.598148	1.1	0.7	0.5	0.4	1.0	A
281	33.360915	131.598167	1.0	0.9	0.3	0.3	0.7	A
282	33.360921	131.598158	1.0	0.8	0.4	0.3	0.8	A
283	33.360936	131.598182	1.0	0.6	0.5	0.3	0.8	A
284	33.360905	131.598233	3.0	3.0	1.7	15.3	39.8	A
285	33.360977	131.598319	2.0	1.4	0.8	2.2	5.8	CG
286	33.360946	131.598469	2.0	1.1	0.8	1.8	4.6	A
287	33.360867	131.598569	2.2	1.6	1.2	4.2	11.0	A
288	33.360923	131.598586	2.0	1.7	1.5	5.1	13.3	A
289	33.360910	131.598625	1.7	1.7	1.2	3.5	9.0	A
290	33.360698	131.598454	3.0	1.7	1.3	6.6	17.2	A
291	33.360763	131.598422	2.4	1.8	1.3	5.6	14.6	A
292	33.360868	131.598405	1.8	1.5	1.3	3.5	9.1	A
293	33.360642	131.598577	2.3	1.9	1.4	6.1	15.9	A
294	33.360566	131.598935	3.0	1.3	1.2	4.7	12.2	A
295	33.360019	131.599496	2.3	2.0	0.9	4.1	10.8	A
296	33.360052	131.599516	2.0	1.4	1.4	3.9	10.2	A
297	33.360048	131.599569	3.0	1.5	1.2	5.4	14.0	A
298	33.359946	131.599517	2.4	1.4	1.2	4.0	10.5	A

Table 4-8. (continued)

299	33.359941	131.599670	4.0	3.0	2.3	27.6	71.8	A
300	33.359915	131.599686	4.5	2.1	2.0	18.9	49.1	A
301	33.359965	131.599805	2.4	2.0	1.1	5.3	13.7	A
302	33.360012	131.599752	1.5	1.2	0.6	1.1	2.8	A
303	33.360007	131.599733	2.3	1.7	1.4	5.5	14.2	A
304	33.360004	131.599682	1.8	1.5	1.5	4.1	10.5	A
305	33.359991	131.599855	1.7	1.3	1.1	2.4	6.3	A
306	33.360019	131.599839	2.7	2.3	1.6	9.9	25.8	A
307	33.360023	131.599883	3.0	2.0	1.7	10.2	26.5	A
308	33.359989	131.599991	2.5	2.2	1.6	8.8	22.9	A
309	33.359906	131.600193	1.5	1.3	1.2	2.3	6.1	A
310	33.359902	131.600256	3.0	2.6	1.2	9.4	24.3	A
311	33.359861	131.600246	1.6	1.2	1.0	1.9	5.0	A
312	33.359836	131.599798	1.2	1.0	0.8	1.0	2.5	A
313	33.359840	131.599775	1.6	1.3	1.2	2.5	6.5	A
314	33.359812	131.599787	1.4	1.2	0.9	1.5	3.9	A
315	33.359851	131.599695	1.2	1.0	0.7	0.8	2.2	A
316	33.359861	131.599681	1.8	1.2	0.9	1.9	5.1	A
317	33.359835	131.599681	1.3	1.0	0.7	0.9	2.4	A
318	33.359804	131.599670	1.6	1.1	0.7	1.2	3.2	A
319	33.359805	131.599654	1.7	1.3	1.2	2.7	6.9	A
327	33.361618	131.598121	1.6	1.0	0.8	1.3	3.3	A
328	33.360298	131.598742	2.3	1.8	1.2	5.0	12.9	A
329	33.360286	131.598755	2.1	1.9	1.2	4.8	12.4	A
330	33.360251	131.598776	3.5	2.7	2.4	22.7	59.0	A
331	33.360400	131.598758	2.2	1.9	1.5	6.3	16.3	A
332	33.360364	131.598706	1.2	1.1	0.8	1.1	2.7	A
333	33.360365	131.598670	1.6	1.5	1.3	3.1	8.1	A
334	33.360344	131.598649	1.7	1.4	1.2	2.9	7.4	A
335	33.360374	131.598642	1.7	1.1	1.0	1.9	4.9	A
336	33.360389	131.598663	1.5	1.4	1.2	2.5	6.6	A
337	33.360401	131.598659	1.0	1.0	0.7	0.7	1.8	A
338	33.360401	131.598658	1.0	0.8	0.8	0.6	1.7	A
339	33.360301	131.598837	1.8	1.5	1.1	3.0	7.7	A
340	33.360334	131.598925	2.5	1.4	1.3	4.6	11.8	A
341	33.360318	131.599159	2.0	1.8	1.5	5.4	14.0	A
342	33.360267	131.599142	3.1	1.5	1.3	6.0	15.7	A
343	33.360167	131.599305	1.9	1.8	1.3	4.4	11.6	A
344	33.360097	131.599270	2.0	1.2	1.2	2.9	7.5	A
345	33.360156	131.599111	2.0	1.5	1.3	3.9	10.1	A
346	33.360193	131.599057	2.1	2.0	1.2	5.0	13.1	A
347	33.360141	131.599004	2.4	1.4	1.0	3.4	8.7	A
348	33.360091	131.598975	3.0	2.4	2.1	15.1	39.3	A
349	33.360160	131.598932	1.9	1.7	1.1	3.6	9.2	A
350	33.360160	131.598829	2.7	1.9	1.4	7.2	18.7	CG
351	33.359989	131.598957	1.2	1.0	0.8	1.0	2.5	CG
352	33.359984	131.599082	2.1	1.3	1.1	3.0	7.8	A
353	33.360016	131.599140	2.0	1.6	1.1	3.5	9.2	A
354	33.359913	131.599466	1.5	1.4	0.8	1.7	4.4	A
355	33.359910	131.599421	1.4	1.1	0.8	1.2	3.2	A
356	33.359837	131.599512	2.1	1.4	1.3	3.8	9.9	A
357	33.359868	131.599532	1.4	1.0	0.6	0.8	2.2	A

Table 4-8. (continued)

358	33.359876	131.599544	1.0	0.9	0.6	0.5	1.4	A
359	33.359780	131.599401	2.4	1.7	1.1	4.5	11.7	A
360	33.359789	131.599308	1.1	0.9	0.7	0.7	1.8	A
361	33.359793	131.599261	1.0	0.7	0.5	0.4	0.9	A
362	33.359780	131.599252	1.0	0.9	0.7	0.6	1.6	A
363	33.359735	131.599269	2.0	1.6	1.0	3.2	8.3	CG
364	33.359676	131.599343	1.2	0.8	0.6	0.6	1.5	A
365	33.359671	131.599577	2.0	1.3	1.3	3.4	8.8	A
366	33.359557	131.599634	2.0	1.6	1.2	3.8	10.0	A
367	33.359547	131.599700	1.8	0.8	0.7	1.0	2.6	A
368	33.359418	131.599782	2.6	1.7	1.6	7.1	18.4	A
369	33.359382	131.599764	2.4	1.9	1.5	6.8	17.8	A
370	33.359387	131.599727	1.3	1.1	0.9	1.3	3.3	A
371	33.359388	131.599702	1.9	0.9	0.8	1.4	3.6	A
372	33.359356	131.599704	1.6	1.3	1.1	2.3	5.9	A
373	33.359352	131.599693	1.3	1.1	1.0	1.4	3.7	A
374	33.359352	131.599713	2.3	1.7	1.3	5.1	13.2	A
375	33.359321	131.599704	3.0	2.7	1.9	15.4	40.0	A
376	33.359339	131.599688	1.1	0.9	0.4	0.4	1.0	A
377	33.359355	131.599734	1.0	1.0	0.4	0.4	1.0	A
378	33.359350	131.599754	2.1	1.4	1.1	3.2	8.4	A
379	33.359334	131.599807	2.0	1.4	1.2	3.4	8.7	A
380	33.359379	131.599780	1.8	1.4	1.1	2.8	7.2	A
381	33.359339	131.599597	1.6	1.3	0.9	1.9	4.9	A
382	33.359313	131.599621	2.0	1.4	1.2	3.4	8.7	A
383	33.359395	131.599547	2.2	1.3	0.9	2.6	6.7	A
384	33.359451	131.599457	1.4	0.9	0.7	0.9	2.3	A
385	33.359445	131.599371	2.4	1.8	1.5	6.5	16.8	A
386	33.359475	131.599333	2.0	1.3	1.1	2.9	7.4	A
387	33.359481	131.599332	2.2	1.5	1.1	3.6	9.4	A
388	33.359505	131.599359	1.2	1.0	0.8	1.0	2.5	A
389	33.359501	131.599438	1.0	0.7	0.7	0.5	1.3	A
390	33.359487	131.599409	1.0	0.8	0.6	0.5	1.2	A
391	33.359514	131.599440	1.1	0.7	0.7	0.5	1.4	A
392	33.359558	131.599433	1.8	1.3	1.2	2.8	7.3	A
393	33.359530	131.599455	1.3	1.1	0.7	1.0	2.6	A
394	33.359531	131.599461	3.3	3.1	2.4	24.6	63.8	A

CHAPTER 5. Discussion

5.1. Depositional environments of the study sites

5.1.1. Oh-enji marsh

The sediment cores from the Oh-enji marsh encompass a record after 8050–8320 cal. yr BP (Figs. 4-3, 4-18, and Table 4-4). The depositional environment of the Oh-enji marsh can be reconstructed from the sedimentary facies as well as the profiles of chemical components and fossil diatom assemblages. It is suggested from the sedimentary facies of poorly sorted silt and alternations of sand and mud that the depositional environment of the silt (gray layer in Fig. 4-1) is an inner bay or a tidal flat. This interpretation is supported by the higher counts/kcps of S and Ca, which occur in higher concentration in seawater than freshwater (e.g. Wedepohl, 1971; Chagué-Goff et al., 2016), as well as a low Mo Inc/Mo Coh ratio which corresponds with an amount of organic matter (Fig. 4-13). The abundance of the brackish–marine and marine diatoms in this layer (diatom zones 3 and 4 in Figs. 4-15 and 4-16) also indicates that this layer had been formed under such environments.

In the organic-rich mud (diatom zone 2), marine species are rare while freshwater species are dominant in the assemblages, indicating that the environment of this zone is estimated to be without major effect from seawater (Figs. 4-15 and 4-16). The sharp decline of the brackish–marine and marine taxa and the significant change of geochemical profile at 470 cm deep in the core OEJ-b (Figs. 4-13, 4-15, and 4-16), between the boundary of the silt (diatom zone 3) and the upper organic-rich mud (diatom zone 2), are probably due to a formation of the barrier spit that fringes seaward side of the study site.

In contrast to the organic rich mud, the depositional environment of the muddy sand ~210 cm deep (diatom zone 1) returns back to an inner bay and a tidal flat again as the sediments are composed of the poorly sorted muddy sand without any sedimentary structures (Figs. 4-1, 4-2, 4-3, and 4-4). This

interpretation is also supported by the element profiles which are similar to those of zones 3 and 4 (Fig. 4-13) and the appearance of brackish–marine and marine diatoms (Figs. 4-15 and 4-16).

5.1.2. Nokinoi lowland

The sedimentary record younger than 590–640 cal. yr BP is lost due to a cultivation at this lowland (Fig. 4-19). The depositional environment of the Nokinoi lowland is also reconstructed by the sedimentary facies as well as the profiles of chemical components and fossil diatom assemblages. The appearance of brackish–marine and marine diatoms in the muddy sand (148–175 cm deep in the core HJ-4) suggests that this layer had been deposited under a marine environment, whereas the organic-rich mud and the silt had been deposited under a non-marine environment since there are very few or no brackish–marine and marine diatoms (Figs. 4-26 and 4-27). The higher concentrations of S and Br in the muddy sand layer deeper than 161 cm of the core HJ-4' also imply this interpretation since these elements exhibit higher concentration in seawater than freshwater (e.g. Wedepohl, 1971; Chagué-Goff et al., 2016; Figs. 4-24 and 4-25). In contrast to the bottom muddy sand, the organic-rich mud and the silt layer had been deposited under a non-marine environment because of a higher Mo Inc/Mo Coh ratio as well as a lower concentration for S, Ca, and Br than the muddy sand (Figs. 4-24 and 4-25).

At the cores HJ-4, 5, and 6, given that the sand layer is overlain by the organic-rich mud and underlain by the silt, the depositional environment in the Nokinoi lowland changed after the deposition of the sand layer (Figs. 4-19, 4-20, and 4-21). The difference in the depositional environment between organic rich mud and silt is also apparent in chemical components and fossil diatom assemblages. There is a small difference in chemical components such as S, K, Ca, Cr, Mn, Rb, Sr, and Zr between the organic-rich mud and silt (Figs. 4-24 and 4-25), and the freshwater and freshwater–brackish diatoms such as *Rhopalodia*

operculata, *Staurosira construens*, *Staurosirella pinnata* and *Pseudostaurosira brevistriata* are observed in the organic-rich mud, but not in the silt (Fig. 4-26).

5.2. Identification of prehistoric tsunami deposits

5.2.1. Sand layers in the Oh-enji marsh

Two thin sand layers A and B in the organic-rich mud at the Oh-enji marsh exhibit sharp contacts with the overlying and underlying muds (Figs. 4-2, 4-3, 4-5b, and 4-6a, b), implying that they were most probably deposited by sudden events. It is widely known that event deposits have sharp erosional bases (e.g. Nanayama et al., 2007; Yamada et al., 2016a). Although sharp upper and lower contacts with the surrounding organic-rich muds are not observed at the subtle sand layer C, considering that the overlying and underlying muds in CT images contain no sand grains, the sand layer C was formed by a sudden event (Figs. 4-2, 4-3, and 4-4). A continuity of the sand layers especially in the seaward side is one of the evidences that these sand layers were formed by seawater inundations (Fig. 4-1).

The sand layers A–C are characterized by higher magnetic susceptibility associated with higher counts of Ti and Fe, as well as higher counts of K, Ca, Mn, and Sr (Fig. 4-13), suggesting that the sand grains were transported from some environments other than the coastal marsh. As the subtle sand layer C in the core OEJ-b consists of a small amount of patchy sand grains in the organic-rich mud, it is difficult to identify that by bare-eye (Figs. 4-2, 4-3, 4-4, 4-5c, and 4-6c), but there is a clear difference in chemical distribution by PCA between the sand layer C (363–366 cm deep) and surrounding organic-rich muds (362–363 cm and 366–367 cm deeps) (Fig. 4-14). In addition to that, an existence of the brackish–marine and marine diatom species in the sand layers implies that the sand was supplied from sea bottom and/or shore (Figs. 4-15 and 4-16).

The sand layers A–C were not likely formed by past flood events since there is no large river which can form sandy sediments on entire lowland (Fig. 2-1). Existences of brackish–marine and marine diatoms in the sand layers also support this explanation (Figs. 4-15 and 4-16). It is difficult to classify the sand layers into tsunami deposits and wash over deposits of storm surges completely, since both are formed by seawater inundation. The Kyushu Island has been damaged by typhoons (e.g. 1945 Makurazaki typhoon, 1951 Ruth typhoon, 1954 Typhoon No. 12, and 1999 Typhoon No. 18; Kyushu Regional Construction Association, 2014). For example, wind set-ups of the Typhoon No. 18 in 1999 caused seawater inundation at coastal lowlands in Kumamoto Prefecture (west coast of Kyushu; e.g. Takikawa, 2000; Goto et al., 2015) and Yamaguchi Prefecture (north coast of Seto Inland Sea; e.g. Mitsunaga et al., 2003), but there is no record that the coastal area of Beppu Bay was inundated by past storm surges in historic ages. It is unlikely that storm surges overtopped the 5-m-high sandbar and inundated the marsh widely (Fig. 4-1). It is difficult to reconstruct the accurate elevation of the marsh and sea level at the time when the sand layers deposited, but the elevation of the sandbar has probably not changed a lot after the formation. Thus, given that the height of the AD 1596 Keicho Bungo tsunami is estimated to be more than 5-m-high (Hatori, 1985a), the sand layers A–C were highly likely deposited by prehistoric tsunamis.

Although there is no strong evidence to identify the sand layer D as a tsunami deposit, their facies are critically different from the other alternations of sand and mud that occur in the marine silt sediments (Figs. 4-2 and 4-4). Considering that the sand layer D is observed at two cores 90 m away each other, it may have been formed by a prehistoric tsunami since tsunami deposit usually spreads across a wide area (e.g. Goto et al., 2011).

The sand layer E, occurring immediately beneath the K-Ah tephra, is characterized by higher magnetic susceptibility, as well as higher counts of Si, Ca, Cr, and Sr (Fig. 4-13). This probably reflects a difference

in the component material between the sand layer E and underlying silt (Figs. 4-3, 4-4, 4-6e, and 4-7d). The sand layer E that consists of very fine to very coarse sand and a pebble, exhibits a grading structure (Fig. 4-12a), suggesting that the layer was deposited by fall-out of sand grains from suspension. In contrast, the subtle inverse grading structure is observed at the sand layer E in the core OEJ-c (Fig. 4-12b). This is probably resulted from a contamination of very coarse- to granule-sized pumices in the upper layer. Given that the sand layer E includes not only sand particles but also volcanic glass shards of K-Ah tephra (Table 4-3), this layer was probably formed at the same time as the falling of K-Ah tephra associated with an eruption of the Kikai caldera c.a. 7300 years ago (e.g. Machida and Arai, 1978). Previous studies about this eruption indicate that the collapse of the caldera generated a huge tsunami based on the geologic records and tsunami simulation (Maeno et al., 2006; Maeno and Imamura, 2007). Actually, a probable tsunami deposit caused by the Akahoya eruption is observed at the Oita City located south coast of Beppu Bay (Fujiwara et al., 2010). Considering these facts, the sand layer E was most likely deposited by a tsunami associated with the Akahoya eruption.

5.2.2. Sand layers in the Nokinoi lowland

Sharp contacts between sand and surrounding muds at the Nokinoi lowland imply that the sand layer was formed by a sudden event (Figs. 4-20 and 4-21). Existence of a rip-up clast in the sand layer indicates erosion of ground surface (Fig. 4-21). These sedimentological features have been reported by recent tsunami studies (e.g. Bondevik et al., 2003; Gelfenbaum and Jaffe, 2003; Nanayama and Shigeno, 2006). During run-up, a tsunami produces various sedimentary structures, such as sharp erosional bases and rip-up clasts.

The sand layer at the Nokinoi lowland exhibits higher magnetic susceptibility associated with higher counts of Ti and Fe, as well as higher counts of Si, S, K, Ca, Mn, Sr, and Ba than in the overlying and

underlying muds (Fig. 4-24). This suggests that the sand grains were supplied from some environments other than freshwater wetland. The PCA also exhibits clear difference between the plotted areas of the sand layer and the other layers of organic-rich mud, silt, and bottom muddy sand with gravels (Fig. 4-25). There are no brackish–marine diatoms in the organic-rich mud and silt layers, but they account for 5–6% of the total within the sand layer, indicating that the sand grains are partially supplied from brackish–marine environment (Figs. 4-26 and 4-27). The differences in grain size and sorting between the sand layer and sediments of modern tidal flat and beach probably imply that the sand layer in the core HJ-4 partly contains the onshore sediments eroded during inundation process (Figs. 4-22, 4-23, and Table 4-6).

5.2.3. Boulders in the Nokinoi lowland

The andesite and conglomerate boulders are mostly concentrated in an area in front of the outcrop of the Akisada pyroclastic flow deposits, but they are rare in other places of the tidal flat (Fig. 2-5; Ishizuka et al., 2005). In addition to their locations, given that the andesite boulder HJ-B2 mainly consists of orthopyroxene, clinopyroxene, and plagioclase, with a vesicular texture in the groundmass (Fig. 4-31), the boulders were supplied from the outcrop of the Akisada pyroclastic flow deposits which are composed of andesite lapilli with volcanic rock.

The maximum boulder weight becomes lighter with distance from the shoreline to seaward along P–P' (Fig. 4-29), suggesting the possibility that some boulders, that dropped down from the outcrop, were reworked seaward by reflected flows of past tsunamis or storm surges. In fact, the boulders transported by the 2004 Indian Ocean tsunami in Pakarang Cape, Thailand, are observed only at seaward side of the high-tide line, and the boulder weight becomes lighter with distance from the shoreline (Goto et al., 2007). The boulders transported to inland by recent tsunamis often show landward finning to reflect a wane of flow

energy (e.g. Spiske and Bahlburg, 2011; Yamada et al., 2014), while landward coarsening is sometimes observed due to a reworking of small boulders seaward by backwash flows (Goto et al., 2012).

Considering that the boulders are moved easily and further by tsunamis than storm surges due to a difference in wavelength (e.g. Goto et al., 2009, 2010), and almost all of boulders have not been reworked for 40 years based on the observation of satellite images (Geospatial Information Authority of Japan, 1975, 2015b), some boulders observed in the Nokinoi lowland might have been reworked seaward by backwash flow of past tsunamis although their reworked ages have not been determined.

5.3. Possible source and chronology of prehistoric tsunamis in Beppu Bay

Given that faulting in Beppu Bay have occurred repeatedly (Fig. 1-3; e.g. Shimazaki et al., 1986; Oita Prefecture, 2002; HERP, 2005) and the tsunami associated with the AD 1596 Keicho Bungo earthquake inundated extensive range of coastal area of the bay (Fig. 1-2a; Hatori, 1985a), the prehistoric tsunami deposits at the study sites were highly likely deposited by tsunamis associated with intraplate earthquakes which occurred at the submarine active faults in the bay. This interpretation is also supported by the previous studies which suggest that the past earthquakes in Nankai Trough, Hyuga-nada, and Median Tectonic Line had a low or no impact to the coastal area of the bay (Fig. 1-2b; Hatori, 1985a, b; Nakanishi, 2002).

It is difficult to unravel an accurate rupture zone of each earthquake associated with the prehistoric tsunami deposits due to a lack of broad geological evidence which encompasses the entire coast of the bay. The height of a tsunami generated by an intraplate earthquake in the bay was calculated based on alternative fault models (Ishibe and Shimazaki, 2005). The calculated maximum wave heights based on the model that assumes ruptures of the all faults in the bay fit to the maximum wave heights of the AD 1596 Keicho Bungo

earthquake tsunami reconstructed by Hatori (1985a). On the other hand, the model that assumes ruptures of the faults only in the central area of the bay shows much lower maximum heights.

The non-marine organic-rich mud at the Oh-enji marsh includes three probable prehistoric tsunami deposits in 3300–3450 cal. yr BP (sand layer A), 4230–4530 cal. yr BP (sand layer B), and 5160–5290 cal. yr BP or later (sand layer C) (Figs. 4-1, 4-18, and 5). The sand layer B is probably formed by an event that occurred during 3600–4600 years ago (e.g. HERP, 2005), and it is possible that the sand layers A and C also correspond to the other faulting that occurred during 3600–4600 and 5300–6000 years ago although their ages are slightly afiel from each other (e.g. HERP, 2005; Figs. 1-2 and 5). The ages of sand layers A and B indicate that the faulting 3600–4600 years ago probably includes at least two activities that are not known from the previous seabed studies (e.g. Oita Prefecture, 2000, 2001, 2002). The sand layer D, evident in the marine silt layer, is dated to 6670–6790 cal. yr BP or later (Fig. 4-18), and this age corresponds with the age of the faulting which occurred during 5800–7300 years ago (e.g. HERP, 2005; Figs. 1-2, 4-18, and 5). The sand layer observed at the Nokinoi lowland was deposited before 1880–2000 cal. yr BP associated with the faulting which occurred 1700–2200 years ago (Figs. 4-19 and 5). The seismic or tsunami turbidite in 1893 is probably formed by this faulting because its age is consistent with the faulting age (Kuwaie et al., 2013; Yamada et al., 2016b).

An interval between the latest tsunami deposit and the AD 1596 Keicho Bungo earthquake is about 1500 years or longer (Fig. 5). Since there is no record relevant to faulting and tubidite between these ages, the faulting approximately 2000 years ago is the latest event before AD 1596. The sand layer A was also deposited about 1500 years ago before the faulting which occurred 2000 years ago. The ages of sand layers A and B are completely determined by plant material obtained immediately above and below the sand layers (Fig. 4-18 and Table 4-4), and the interval between them is estimated to be approximately 800–1200 years

(Fig. 5). The sand layer C with the age of 5160–5290 cal. yr BP is formed 600–1000 years before the deposition of the sand layer B, and an interval between sand layers C and D is about 1500 years (Fig. 5).

This study identified four probable prehistoric tsunami deposits, and their recurrence interval is estimated to be approximately 850–1500 years (Fig. 5). However, this interval is not necessarily the same as the interval of the faulting of the submarine active faults, as faulting are not always generate tsunamis.

5.4. Past faultings estimated from the sedimentary record

The thick inner bay or tidal flat sediments (~210 cm deep in the core OEJ-b) at the Oh-enji marsh was not likely deposited a seawater inundation, because layers more than 100 cm thick were rarely deposited by modern major tsunamis such as the 2011 Tohoku-oki tsunami and the 2004 Indian Ocean tsunami (e.g. Hori et al., 2007; Goto et al., 2011; Yamada and Fujino, 2013). Another possible cause of deposition of the thick sediments is sea-level change, but the abrupt increase of brackish–marine and marine taxa in the muddy sand layer (zone 1) conflicts with the sea level lowering from ca. 6000 years ago (Yokoyama et al., 1996). As far as the facies change from non-marine to marine sediments is not able to be explained by the sea level change, the most likely interpretation is a local subsidence associated with faulting at south of the Oh-enji marsh (Saganoseki fault; Fig. 1-3).

The hypothesis of the subsidence is also supported by an occurrence elevation of the organic-rich mud which is evident between –3 and 0 m.a.s.l. (Fig. 4-1). This indicates that the Oh-enji marsh has secularly subsided, because non-marine organic-rich mud is deposited on a freshwater marsh of more than 0 m.a.s.l. Although the accurate timing and single amount of faulting are not revealed, the Oh-enji marsh must have repeatedly subsided over the long term.

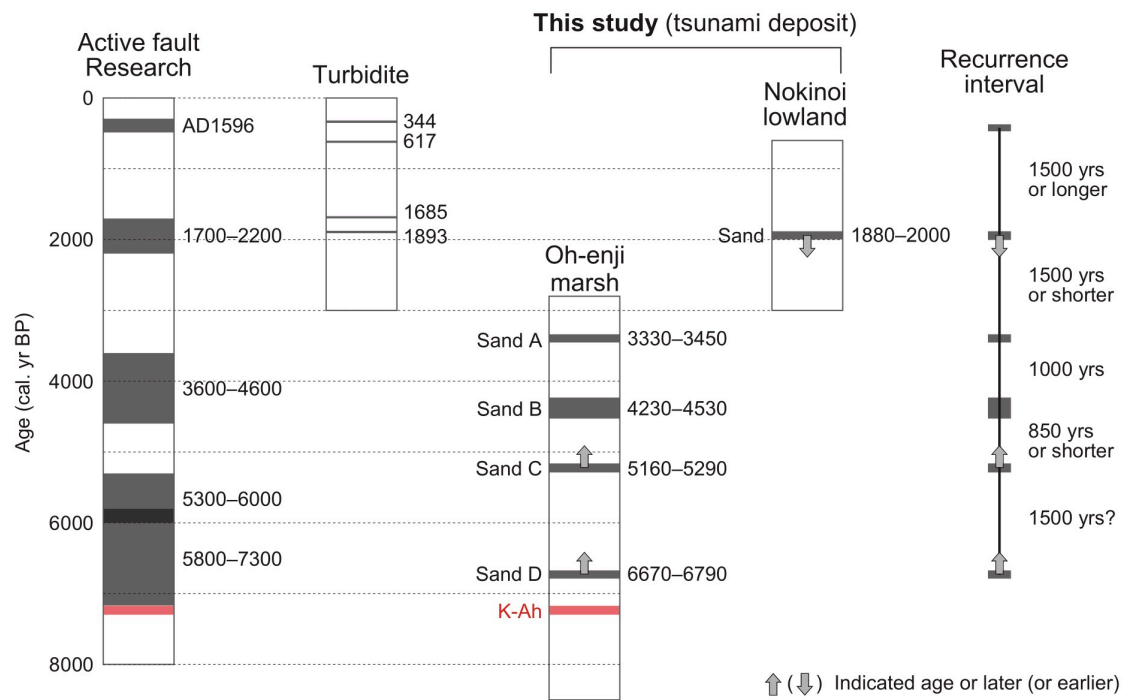


Fig. 5. Comparison of the age of prehistoric tsunami deposits with the faulting history of the submarine active faults in the bay (modified after Oita Prefecture, 2000, 2001, 2002; HERP, 2005; Kuwae et al., 2013; Yamada et al., 2016b) with the recurrence interval of the prehistoric tsunami deposits as well as the AD 1596 Keicho Bungo earthquake.

CHAPTER 6. Conclusion

In this study, onshore sediment cores were obtained from the coastal lowlands of Beppu Bay to establish a detailed chronology of tsunamigenic intraplate earthquakes in prehistoric age. A total of five probable prehistoric tsunami deposits associated with intraplate earthquakes were identified and dated to 1880–2000 cal. yr BP or earlier, 3300–3450 cal. yr BP, 4230–4530 cal. yr BP, 5160–5290 cal. yr BP or later, and 6670–6790 cal. yr BP or later. Based on these ages as well as the AD 1596 Keicho Bungo earthquake, a recurrence interval of the prehistoric tsunamis is estimated to be approximately 850–1500 years.

At the Oh-enji marsh, south coast of the bay, the sediments abruptly changed from a non-marine organic-rich mud to an inner bay or tidal flat muddy sand at around 200 cm deep. This is probably explained by a local subsidence associated with intraplate earthquakes which occurred at the active fault located south of the Oh-enji marsh as this environmental change cannot be explained by the sea level lowering since ca. 6000 years ago. The evidence for the subsidence can also be seen in the difference between present elevation (< 0 m.a.s.l.) and the elevation at the depositional time (> 0 m.a.s.l.) of the non-marine organic-rich mud.

This study provides the accurate ages of prehistoric tsunami inundations as well as the possibility that the easternmost area of the Oita plain has secularly subsided by the faulting of the Saganoseki fault. Further studies collaborating with active fault researches will unravel a detailed faulting history of the highly complex active faults in Beppu Bay.

Acknowledgments

I am greatly indebted to Associate professor Shigehiro Fujino, Professor Ken-ichiro Hisada, Professor Norikazu Matsuoka (University of Tsukuba), and Associate professor Kazuhisa Goto (Tohoku University) for providing valuable and constructive comments. I would like to thank Professor Norihiro Nakamura, Tetsuro Sato (Tohoku University), Associate professor Jonathan Woodruff (University of Massachusetts), Dr. Takashi Chiba (Hokkaido University), Assistant professor Tetsuya Shinozaki, Ryo Okuwaki, Kohei Tominaga (University of Tsukuba) for supporting field surveys. I thank Dr. Takashi Chiba (Hokkaido University) for conducting diatom analysis, Kohei Tominaga (University of Tsukuba) for creating a thin-section of a boulder, and Shogo Ishii (University of Tsukuba) for his assistance in grain size analysis. I also would like to thank Associate professor Catherine Chagué-Goff (University New South Wales) for conducting PCA with R studio and providing valuable comments to the geochemical results.

This study was supported by Program to Disseminate Tenure Tracking System, MEXT, Japan (S. Fujino), Japan Nuclear Energy Safety Organization currently known as Secretariat of Nuclear Regulation Authority (T. Takahashi), and JSPS KAKENHI Grant Number 14J00107 (M. Yamada). The Oita Environmental Protection Forum and the Nokinoi Agricultural Association consented to my field surveys. The CT image scanning and measurements of magnetic susceptibility and geochemical signature (ITRAX) were performed under the cooperative research program of the Center for Advanced Marine Core Research, Kochi University (Accept Nos. 15A018, 15B015, and 16B008). The cores OEJ-a–c were collected by use of the mechanical thin-wall sampler by Oyo Corporation. The radiocarbon dating and tephra analysis were conducted at the Geo Science Laboratory Co. Ltd. and Kyoto Fission-track Co. Ltd., respectively. Many figures were generated with use of the Generic Mapping Tools (Wessel and Smith, 1998).

References

- Altinok, Y., Alpar, B., Ersoy, S., Yalciner, A.C., 1999. Tsunami generation of the Kocaeli Earthquake (August 17th 1999) in the Izmit Bay; coastal observations, bathymetry and seismic data. *Turkish Journal of Marine Science* **5**, 131–148.
- Altinok, Y., Tinti, S., Alpar, B., Yalciner, A.C., Ersoy, S., Bortolucci, E., Armigliato, A., 2001. The Tsunami of August 17, 1999 in Izmit Bay, Turkey. *Natural Hazards* **24**, 133–146.
- Awata, Y., Yoshioka, T., Tsukuda, E., Emre, O., Duman, T.Y., Dogan, A., 2001. Segment structure of the surface ruptures associated with the 1999 Izmit earthquake, North Anatolian fault system, Turkey. *Annual Report on Active Fault and Paleearthquake Researches* **1**, 325–338 (in Japanese with English abstract).
- Barka, A., Akyuz, H.S., Altunel, E., Sunal, G., Calir, Z., Dikbas, A., Yerli, B., Armijo, R., Meyer, B., de Chabaliere, J.B., Rockwell, T., Dolan, J.R., Hartleb, R., Dawson, T., Christofferson, S., Tucker, A., Fumal, T., Langridge, R., Stenner, H., Lettis, W., Bachhuber, J., Page, W., 2002. The Surface Rupture and Slip Distribution of the 17 August 1999 Izmit Earthquake (M 7.4), North Anatolian Fault. *Bulletin of the Seismological Society of America* **92**, 43–60.
- Bondevik, S., Mangerud, J., Dawson, S., Dawson, A., Lohne, O., 2003. Record-breaking height for 8000-year-old tsunami in the North Atlantic. *Eos Transactions American Geophysical Union* **84**, 289–300.
- Bouchard, F., Francus, P., Pienitz, R., Laurion I., 2011. Sedimentology and geochemistry of thermokarst ponds in discontinuous permafrost, subarctic Quebec, Canada. *Journal of Geophysical Research: Biogeosciences* **116**, G00M04.
- Chagué-Goff, C., Chi Hang Chan, J., Goff, J., Gadd, P., 2016. Late Holocene record of environmental

- changes, cyclones and tsunamis in a coastal lake, Mangania, Cook Island. *Island Arc* **25**, 333–349.
- Chagué-Goff, C., Goff, J., Nichol, S.L., Dudley, W., Zawadzki, A., Bennett, J.W., Mooney, S.D., Fierro, D., Heijnis, H., Dominey-Howes, D., Courtney, C., 2012. Multi-proxy evidence for trans-Pacific tsunamis in the Hawai'ian Islands. *Marine Geology* **299–302**, 77–89.
- Chagué-Goff, C., Szczuciński, W., Shinozaki, T., 2017. Applications of geochemistry in tsunami research: A review. *Earth-Science Reviews* **165**, 203–244.
- Chiba, T., Sawai, Y., 2014. Reexamination and updating of diatom species for paleoenvironmental reconstructions. *Diatom* **30**, 17–30 (in Japanese with English abstract).
- Cisternas, M., Atwater, B.F., Torrejón, F., Sawai, Y., Machuca, G., Lagos, M., Eipert, A., Youlton, C., Salgado, I., Kamataki, T., Shishikura, M., Rajendran, C.P., Malik, J.K., Rizal, Y., Husni, M., 2005. Predecessors to the giant 1960 Chile earthquake. *Nature* **437**, 404–407.
- Danhara, T., Yamashita, T., Iwano, H. and Kasuya, M., 1992, An improved system for measuring refractive index using the thermal immersion method. *Quaternary International* **13/14**, 89–91.
- Folk R.L. 1966. A review of grain-size parameters. *Sedimentology* **6**, 73–93.
- Fujino, S., Naruse, H., Matsumoto, D., Jarupongsakul, T., Sphawajruksakul, A., Sakakura, N., 2009. Stratigraphic evidence for pre-2004 tsunamis in southwestern Thailand. *Marine Geology* **262**, 25–28.
- Fujino, S., Naruse, H., Matsumoto, D., Sakakura, N., Sphawajruksakul, A., Jarupongsakul, T., 2010. Detailed measurements of thickness and grain size of a widespread onshore tsunami deposit in Phang-nga Province, southwestern Thailand. *Island Arc* **19**, 389–398.
- Fujisawa, Y., Ueno, H., Kobayashi, T., 2001. 2.2 ka eruption study on the emplacement temperature of pyroclastic deposits of Yufu Volcano, Japan. *Kazan* **46**, 187–203 (in Japanese with English abstract).
- Fujiwara, O., Machida, H., Shiochi, J., 2010. Tsunami deposit from the 7,300 cal BP Akahoya eruption

preserved in the Yokoo midden, north Kyushu, West Japan. *The Quaternary Research* **49**, 23–33 (in Japanese with English abstract).

Furumura, T., Imai, K. and Maeda, T., 2011, A revised tsunami source model for the 1707 Hōei earthquake and simulation of tsunami inundation of Ryūjin Lake, Kyushu, Japan. *Journal of Geophysical Research* **116**, B02308.

Furusawa, A., Umeda, K., 2000. Tephra stratigraphy of piston cores in Beppu Bay during the past 7000 years –correlation of the core tephra with Aso and Kuju Volcano–. *Journal of Geological Society of Japan* **106**, 31–49 (in Japanese with English abstract).

Gelfenbaum, G., Jaffe, B., 2003. Erosion and sedimentation from the 17 July 1998 Papua New Guinea tsunami. *Pure and Applied Geophysics* **160**, 1969–1999.

Geospatial Information Authority of Japan, 1947. A browse service of maps and aerial photographs. <<http://mapps.gsi.go.jp/maplibSearch.do#1>> (in Japanese).

Geospatial Information Authority of Japan, 1975. A browse service of maps and aerial photographs. <<http://mapps.gsi.go.jp/maplibSearch.do#1>> (in Japanese).

Geospatial Information Authority of Japan, 2007. A browse service of maps and aerial photographs. <<http://mapps.gsi.go.jp/maplibSearch.do#1>> (in Japanese).

Geospatial Information Authority of Japan, 2015a. A download service of the Fundamental Geospatial Data. <<http://fgd.gsi.go.jp/download/mapGis.php>> (in Japanese).

Geospatial Information Authority of Japan, 2015b. A browse service of maps and aerial photographs. <<http://mapps.gsi.go.jp/maplibSearch.do#1>> (in Japanese).

Goff, J., Chagué-Goff, C., Nichlo, S., Jaffe, B., Dominey-Howes, D., 2012. Progress in paleotsunami research. *Sedimentary Geology* **243–244**, 70–88.

- Goff, J., McFadgen, B.G., Chagué-Goff, C., 2004. Sedimentary differences between the 2002 Easter storm and the 15th-century Okoropunga tsunami, southeastern North Island, New Zealand. *Marine Geology* **204**, 235–250.
- Goto, K., Chagué-Goff, C., Fujino, S., Goff, J., Jaffe, B., Nishimura, Y., Richmond, B., Sugawara, D., Szczuciński, W., Tappin, D. R., Witter, R. C., Yulianto, E., 2011. New insights of tsunami hazard from the 2011 Tohoku-oki event. *Marine Geology* **290**, 46–50.
- Goto, K., Chavanich, S.A., Imamura, F., Kunthasap, P., Matsui, T., Minoura, K., Sugawara, D., Yanagisawa, H., 2007. Distribution, origin and transport process of boulders deposited by the 2004 Indian Ocean tsunami at Pakarang Cape, Thailand. *Sedimentary Geology* **202**, 821–837.
- Goto, K., Kawana, T., Imamura, F., 2010. Historical and geological evidence of boulders deposited by tsunamis, southern Ryukyu Islands, Japan. *Earth-Science Reviews* **102**, 77–99.
- Goto, K., Okada, K. and Imamura, F., 2009. Characteristics and hydrodynamics of boulders transported by storm waves at Kudaka Island, Japan. *Marine Geology* **262**, 14–24.
- Goto, K., Sugawara, D., Ikema, S., Miyagi, T., 2012. Sedimentary processes associated with sand and boulder formed by the 2011 Tohoku-oki tsunami at Sabusawa Island, Japan. *Sedimentary Geology* **282**, 188–198.
- Goto, K., Goto, T., Nmor, J.C., Minematsu, K., Gotoh K., 2015. Evaluating salinity damage to crops through satellite data analysis: application to typhoon affected areas of southern Japan. *Natural Hazards* **75**, 2815–2828.
- Hahn, A., Kliem, P., Oehlerich, M., Ohlendorf, C., Zolitschka, B., the PASADO Science Team, 2014, Elemental composition of the Laguna Potrok Aike sediment sequence reveals paleoclimatic changes over the past 51 ka in southern Patagonia, Argentina. *Journal of Paleolimnology* **52**, 349–366.

- Hatori, T., 1985a. Field investigation of the 1596 Bungo tsunami along the coast of Beppu Bay, Kyushu. *Bulletin of the Earthquake Research Institute, University of Tokyo* **60**, 429–438 (in Japanese with English abstract).
- Hatori, T., 1985b. Field investigation of historical tsunamis along the east coast of Kyushu, west Japan. *Bulletin of the Earthquake Research Institute, University of Tokyo* **60**, 439–459 (in Japanese with English abstract).
- Hatori, T., 1988. Tsunami behaviors in the Seto Inland Sea and Bungo Channel caused by the Nankaido earthquakes in 1707, 1854 and 1946. *Journal of the Seismological Society of Japan* **41**, 215–221 (in Japanese with English abstract).
- Headquarters for Earthquake Research Promotion (HERP), 2005. The evaluation of Beppu–Haneyama Fault Zone. pp. 1–73 (in Japanese).
- Headquarters for Earthquake Research Promotion (HERP), 2016. The long-term evaluation of Suo-nada Fault Zone (Suo-nada and Ube-oki fault complexes). pp. 1–28 (in Japanese).
- Hirabayashi, S., Yokoyama, Y., Suzuki, A., Miyairi, Y., Aze, T., 2017. Short-term fluctuations in regional radiocarbon reservoir age recorded in coral skeletons from the Ryukyu Islands in the north-western Pacific. *Journal of Quaternary Science* **32**, 1–6.
- Hori, K., Kuzumoto, R., Hirouchi, D., Umitsu, M., Janjirawuttikul, N., and Patanakanog, B., 2007. Horizontal and vertical variation of 2004 Indian tsunami deposits: An example of two transects along the western coast of Thailand. *Marine Geology*, **239**, 163–172.
- Hyodo, M., Hori, T., 2013. Re-examination of possible great interplate earthquake scenarios in the Nankai Trough, southwest Japan, based on recent findings and numerical simulations. *Tectonophysics* **600**, 175–186.

- Idei, M., Osada, K., Sato, S., Toyoda, K., Nagumo, T., Mann, D.G., 2012. Gametogenesis and auxospore development in *Actinocyclus* (Bacillariophyta). *PLoS One* **7**, e41890.
- Inoue, T., Sugiyama, Y., Murakami, F., Sakamoto, I., Takino, Y., Nagata, T., Hosoya, T., Usami, T., 2014. Latest Pleistocene-Holocene activity of the A fault system, an offshore segment of the Mikata Fault Zone, off Hiruga, Mihama Town, Fukui Prefecture, central Japan. *Annual Report on Active Fault and Paleoseismicity Researches* **14**, 109–156 (in Japanese with English abstract).
- Ishibe, T., Shimazaki, K., 2005. Estimation of the source of tsunami accompanied by the 1596 Keicho-Bungo earthquake. *Historical Earthquakes* **20**, 119–131 (in Japanese with English abstract).
- Ishizuka, Y., Mizuno, K., Matsuura, H., Hoshizumi, H., 2005. Geology of the Bungo-Kitsuki district. *Quadrangle Series, 1:50,000, Geological Survey of Japan, AIST*, 83pp (in Japanese).
- Itoh, Y., Kusumoto, S., Takemura, K., 2014. Evolutionary process of Beppu Bay in central Kyushu, Japan: a quantitative study of the basin-forming process controlled by plate convergence modes. *Earth Planets Space* **66**, 1–14.
- Itoh, Y., Takemura, K., Kamata, H., 1998. History of basin formation and tectonic evolution at the termination of a large transcurrent fault system: deformation mode of central Kyushu, Japan. *Tectonophysics* **284**, 135–150.
- Iwabuchi, Y., 2000. Active structures in Osaka Bay and Ise Bay. *The Quaternary Research* **39**, 303–314 (in Japanese with English abstract).
- Jankaew, K., Atwater, B., Sawai, Y., Choowong, M., Charoentitirat, T., Martin, M., Prendergast, A., 2008. Medieval forewarning of the 2004 Indian Ocean tsunami in Thailand. *Nature* **455**, 1228–1231.
- Japan Hydrographic Association, 2015. M7000 Digital Bathymetric Chart (M7003: off the south coast of Shikoku–Bungo-suido).

- Kamata, H., Danhara, T., Hayashida, A., Hoshizumi, H. and Yamashita, T., 1994, Correlation of the Imaichi pyroclastic-flow deposit to the similar pyroclastic-flow deposits in central Kyushu, Japan, and estimation of their source vent. *Journal of Geological Society of Japan* **100**, 279–291 (in Japanese with English abstract).
- Kamata, H., Kobayashi, T., 1997. The eruptive rate and history of Kuju volcano in Japan during the past 15,000 years. *Journal of Volcanology and Geothermal Research* **76**, 163–171.
- Kobayashi, H., Idei, M., Mayama, S., Nagumo, T., Osada, K., 2006. H. Kobayashi's atlas of Japanese diatoms based on electron microscopy 1. 531pp. Uchida Rokakuho, Tokyo (in Japanese).
- Kozak, L., Niedzielski, P., 2013. The evolution of December 2004 tsunami deposits: temporal and spatial distribution of potentially toxic metalloids. *Chemosphere* **93**, 1856–1865.
- Krammer, K., 2000. The genus *Pinnularia*. 703 pp. In: Lange-Bertalot, H. (Ed.) *Diatoms of Europe: Diatoms of the European Inland Waters and Comparable Habitats 1*. A.R.G. Gantner Verlag K.G., Ruggell.
- Krammer, K., Lange-Bertalot, H., 1986. *Bacillario-phyceae 2/1. Naviculales*. In: Ettl, H., Gerloff, J., Heynig, H., Mollenhauser, D. (Eds.), *Susswasserflora von Mitteleuropa*. Gustav Fischer Verlag, Stuttgart.
- Krammer, K., Lange-Bertalot, H., 1988. *Bacillario-phyceae 2/2. Basillariaceae, Epithemiaceae, Surirellaceae*. In: Ettl, H., Gerloff, J., Heynig, H., Mollenhauser, D. (Eds.), *Susswasserflora von Mitteleuropa*. Gustav Fischer Verlag, Stuttgart.
- Krammer, K., Lange-Bertalot, H., 1991a. *Bacillario-phyceae 2/3. Centrales, Fragilariaceae, Eunotiaceae*. In: Ettl, H., Gerloff, J., Heynig, H., Mollenhauser, D. (Eds.), *Susswasserflora von Mitteleuropa*. Gustav Fischer Verlag, Stuttgart.

- Krammer, K., Lange-Bertalot, H., 1991b. Bacillaro-phyceae 2/4. Achnanthaceae, Kritische Ergänzungen zu *Navicula* (Lineolatae) und *Gomphonema*. In: Ettl, H. (Ed.), *Pascher's Süßwasserflora von Mitteleuropa*, vol. 2, part 4. Gustav Fischer Verlag, Stuttgart.
- Kumaki, Y., Ota, M., Iida, M., Shioya, F., 1986. A submarine active fault found in northern Suo-nada sea. *Active Fault Research* **2**, 73–76 (in Japanese).
- Kuwae, M., Yamamoto, M., Ikehara, K., Irino, T., Takemura, K., Sagawa, T., Sakamoto, T., Ikehara, M., Takeoka, H., 2013. Stratigraphy and wiggle-matching-based age-depth model of late Holocene marine sediments in Beppu Bay, southwest Japan. *Journal of Asian Earth Science* **69**, 133–148.
- Kyushu Regional Construction Association, 2014. Information database of disaster history in Kyushu. <<http://saigairireki.qscpua2.com>> (in Japanese).
- Loveless, J.P., Meade, B.J., 2010. Geodetic imaging of plate motions, slip rates, and partitioning of deformation in Japan. *Journal of Geophysical Research: Solid Earth* **115**, B02410.
- Machida, H., Arai, F., 1978. Akahoya ash –A Holocene widespread tephra erupted from the Kikai caldera, south Kyushu, Japan. *The Quaternary Research* **17**, 143–163 (in Japanese with English abstract).
- Maeno, F., Imamura, F., 2007. Numerical investigations of tsunamis generated by pyroclastic flows from the Kikai caldera, Japan. *Geophysical Research Letters* **34**, L23303.
- Maeno, F., Imamura, F., Taniguchi, H., 2006. Numerical simulation of tsunamis generated by caldera collapse during the 7.3 ka Kikai eruption, Kyushu, Japan. *Earth Planets Space* **58**, 1013–1024.
- Matsumoto, D., Sawai, Y., Yamada, M., Namegaya, Y., Shinozaki, T., Takeda, D., Fujino, S., Tanigawa, K., Nakamura, A., Pilarczyk, J., 2016. Erosion and sedimentation during the September 2015 flooding of the Kinu River, central Japan. *Scientific Reports* **6**, 34168.
- Minoura, K., Imamura, F., Sugawara, D., Kono, Y., Iwashita, T., 2001. The 869 Jōgan tsunami deposit and

- recurrence interval of large-scale tsunami on the Pacific coast of northeast Japan. *Journal of Natural Disaster Science* **23**, 83–88.
- Minoura, K., Nakata, T., 1994. Discovery of an ancient tsunami deposit in coastal sequences of southwest Japan: Verification of a large historic tsunami. *Island Arc* **3**, 66–72.
- Mitsunaga, T., Hiraishi, T., Utsunomiya, Y., Mihara, M., Okawa, I., Nakagawa, K., 2003. Characteristics of storm surge damages caused by Typhoon 9918 in Suo-nada Sea. *Doboku Gakkai Ronbunshuu* **726**, 131–143 (in Japanese with English abstract).
- Miyazaki, K., Yoshioka, T., 1994. Geology of Saganoseki district. *With Geological Sheet Map at 1:50,000, Geological Survey of Japan, AIST*, 40pp (in Japanese with English abstract).
- Morton, R.A., Gelfenbaum, G., Jaffe, B.E., 2007. Physical criteria for distinguishing sandy tsunami and storm deposits using modern examples. *Sedimentary Geology* **200**, 184–207.
- Nagumo, T., 2003. Taxonomic studies of the subgenus *Amphora* Cleve of the genus *Amphora* (Bacillariophyceae) in Japan. *Bibliotheca Diatomologica* **49**, 1–265.
- Nanayama, F., Furukawa, R., Shigeno, K., Makino, A., Soeda, Y., Igarashi Y., 2007. Nine unusually large tsunami deposits from the past 4000 years at Kiritappu marsh along the southern Kuril Trench. *Sedimentary Geology* **200**, 275–294.
- Nanayama, F., Satake, K., Furukawa, R., Shimokawa, K., Atwater, B. F., Shigeno, K., Yamaki, S., 2003. Unusually large earthquakes inferred from tsunami deposits along the Kuril trench. *Nature* **424**, 660–663.
- Nanayama, F., Shigeno, K., 2006. Inflow and outflow facies from the 1993 tsunami in southwest Hokkaido. *Sedimentary Geology* **187**, 139–158.
- Nakamura, K., Kuwatani, T., Kawabe, Y., Komai, T., 2016. Extraction of heavy metals characteristics of

- the 2011 Tohoku tsunami deposits using multiple classification analysis. *Chemosphere* **144**, 1241–1248.
- Nakanishi, I., 2002. Historical material showing disasters due to the September 1, 1596 earthquake in the Northwestern Shikoku Island, Japan. *Journal of the Seismological Society of Japan* **55**, 311–316 (in Japanese).
- Nakata, T., Shimazaki, K., 1993. Investigation of submarine sources of earthquakes. *Kagaku* **63**, 593–599 (in Japanese).
- Nakata, T., Shimazaki, K., 1997. Geo-slicer, a newly invented soil sampler, for high-resolution active fault studies. *Journal of Geography* **106**, 59–69 (in Japanese with English abstract).
- National Institute of Advanced Industrial Science and Technology (AIST), 2012. Active Fault Database of Japan, February 28, 2012 Version. <https://gbank.gsj.jp/activefault/index_gmap.html>.
- Oita Prefecture, 2000. A research report of Beppu-Haneyama Fault Zone (part of offshore survey). <<http://www.hp1039.jishin.go.jp/danso/Oita6Efrm.htm>> (in Japanese).
- Oita Prefecture, 2001. A research report of Beppu-Haneyama Fault Zone (part of offshore survey). <<http://www.hp1039.jishin.go.jp/danso/Oita6Afrm.htm>> (in Japanese).
- Oita Prefecture, 2002. A research report of Beppu-Haneyama Fault Zone (part of offshore survey). <<http://www.hp1039.jishin.go.jp/danso/Oita8Bfrm.htm>> (in Japanese).
- Okada, A., Toyokura, I., Makinouchi, T., Fujiwara, Y., Ito, T., 2000, The Ise Bay Fault off the Chita Peninsula, Central Japan. *Journal of Geography* **109**, 10–26 (in Japanese with English abstract).
- Okamura, M., Shimazaki, K., Nakata, T., Chida, N., Miyatake, T., Maemoku, H., Tsutsumi, H., Nakamura, T., Yamaguchi, C., Ogawa, M., 1992. Submarine active faults in the northwestern part of Beppu Bay, Japan –On a new technique for submarine active fault survey–. *The memoirs of the Geological*

Society of Japan **40**, 65–74 (in Japanese with English abstract).

- Reimer, P.J., Bard, E., Bayliss, A., Beck, J.W., Blackwell, P.G., Ramsey, C.B., Buck, C.E., Cheng, H., Edwards, R.L., Friedrich, M., Grootes, P.M., Guilderson, T.P., Haflidason, H., Hajdas, I., Hatté, C., Heaton, T.J., Hoffmann, D.L., Hogg, A.G., Hughen, K.A., Kaiser, K.F., Kromer, B., Manning, S.W., Niu, M., Reimer, R.W., Richards, D.A., Scott, E.M., Southon, J.R., Staff, R.A., Turney, C.S.M., Plicht, J.v.d., 2013. IntCal13 and Marine13 radiocarbon age calibration curves 0–50,000 years cal BP. *Radiocarbon* **55**, 1869–1887.
- Round, F.E., Crawford, R.M., Mann, D.G., 1990. The diatoms. Biology & morphology of the genera. 747pp. Cambridge University Press, Cambridge.
- Sakuna, D., Szczuciński, W., Feldens, P., Schwarzer, K., Khokiattiwong, S., 2012. Sedimentary deposits left by the 2004 Indian Ocean tsunami on the inner continental shelf offshore of Khao Lak, Andaman Sea (Thailand). *Earth Planets Space* **64**, 931–943.
- Sawai, Y., 2012. Study on paleotsunami deposits in geologic stratum. *Journal of Geological Society of Japan* **118**, 535–558 (in Japanese with English abstract).
- Sawai, Y., Fujii, Y., Fujiwara, O., Kamataki, T., Komatsubara, J., Okamura, Y., Satake, K., Shishikura, M., 2008. Marine incursions of the past 1500 years and evidence of tsunamis at Suijin-numa, a coastal lake facing the Japan Trench. *Holocene* **18**, 517–528.
- Sawai, Y., Kamataki, T., Shishikura, M., Nasu, H., Okamura, Y., Satake, K., Thomson, K.H., Matsumoto, D., Fujii, Y., Komatsubara, J., Aung, T.T., 2009. Aperiodic recurrence of geologically recorded tsunamis during the past 5500 years in eastern Hokkaido, Japan. *Journal of Geophysical Research* **114**, B01319.
- Sawai, Y. and Nagumo, T., 2003a. Diatoms (Bacillariophyceae) flora of salt marshes along the Pacific coast

- of eastern Hokkaido, Northern Japan. *Bulletin of the Nippon Dental University* **32**, 93–108.
- Sawai, Y. and Nagumo, T., 2003b. Diatoms from Alsea Bay, Oregon, USA. *Diatom* **19**, 33–46.
- Sawai, Y., Satake, K., Kamataki, T., Nasu, H. Shishikura, M., Atwater, B.F., Horton, B.P., Kelsey, H.M., Nagumo, T., Yamaguchi, M., 2004. Transient uplift after a 17th-century earthquake along the Kuril subduction zone. *Science* **306**, 1918–1920.
- Schneider, J-L., Chagué-Goff, C., Bouchez, J-L., Goff, J., Sugawara, D., Goto, K., Jaffe, B., Richmond, B., 2014, Using magnetic fabric to reconstruct the dynamics of tsunami deposition on the Sendai Plain, Japan –The 2011 Tohoku-oki tsunami. *Marine Geology* **358**, 89–106.
- Seno, T., Stein, S., Gripp, A.E., 1993. A model for the motion of the Philippine Sea Plate consistent with NUVEL-1 and geological data. *Journal of Geophysical Research* **98**, 17941–17948.
- Shimazaki, K., Matsuoka, H., Okamura, M., Chida, N., Nakata, T., 2000. A distribution of submarine active faults in Beppu Bay. *Chikyū Monthly Symposium* **28**, 79–84 (in Japanese).
- Shimazaki, K., Nakata, T., Chida, N., Miyatake, T., Okamura, M., Shiragami, H., Maemoku, H., Matsuki, H., Tsuji, M., Kiyokawa, S., Hirata, K., 1986, A preliminary report on the drilling project of submarine active faults beneath Beppu Bay; Southwest Japan, for longterm earthquake prediction. *The Quaternary Research* **2**, 83–88 (in Japanese).
- Smith, V.C., Staff, R.A., Blockley, S.P.E., Bronk Ramsey, C., Nakagawa, T., Mark, D.F., Takemura, K., Danhara, T., 2013. Identification and correlation of visible tephra in the Lake Suigetsu SG06 sedimentary archive, Japan: chronostratigraphic markers for synchronising of east Asian/west Pacific palaeoclimatic records across the last 150 ka. *Quaternary Science Reviews* **67**, 121–137.
- Spiske, M., Bahlburg, H., 2011. A quasi-experimental setting of coarse clast transport by the 2010 Chile tsunami (Bucalemu, Central Chile). *Marine Geology* **289**, 72–85.

- Sugiyama, Y., Inoue, T., Murakami, F., Sakamoto, I., Takino, Y., Nagata, T., Hosoya, T., Usami, T., 2014. Latest Pleistocene-Holocene activity of the offshore segment of the Nosaka fault, off Sugahama, Mihama Town, Fukui Prefecture, central Japan. *Annual Report on Active Fault and Paleoearthquake Researches* **14**, 57–108 (in Japanese with English abstract).
- Takada, K., Nakata, T., Miyagi, T., Haraguchi, T., Nishitani, Y., 2002. Handy geoslicer –new soil sampler for Quaternary geologist. *Chishitsu News* **579**, 12–18 (in Japanese with English abstract).
- Takikawa, K., 2000. Tidal wave disaster by Typhoon 9918 in the Shiranui Sea. *Civil Engineering* **85**, 41–45 (in Japanese).
- Umeda, K., Furusawa, A., Ui, T., 1996. Holocene eruptive activity of Yufu-Tsurumi Volcano Group found from piston cores in Beppu Bay, central Kyushu. *Bulletin of the Volcanological Society of Japan* **41**, 61–71 (in Japanese with English abstract).
- Usami, M., 2002. Distribution of the Osaka-wan fault estimated from the existing multi-channel seismic profiles. *Active Fault Research* **22**, 111–114 (in Japanese with English abstract).
- Watanabe, T., Asai, K., Ohtsuka, T., Tuji, A., Houki, A., 2005. Picture Book and Ecology of Freshwater Diatoms. 784pp. Uchida Rokakuho, Tokyo (in Japanese).
- Wedepohl, K.H., 1971. Environmental influences on the chemical composition of shales and clays. *Physics and Chemistry of the Earth* **8**, 305–333.
- Wessel, P., Smith, W.H.F., 1998. New, improved version of the Generic Mapping Tools released. *Eos Transactions American Geophysical Union* **79**, 579.
- Witkowski, A., Lange-Bertalot, H., Metzeltin, D., 2000. Iconographia Diatomologica 7,925pp. In Lange-Bertalot, H., (Ed.), Diatom Flora of Marine Coasts 1, A. R. Gantner Verlag, Liechtenstein.
- Yamada, M., Fujino, S., 2013. Sedimentary characteristics of the onshore tsunami deposits formed by the

- 2011 Tohoku-oki tsunami in coastal lowlands, Ibaraki and Chiba prefectures. *Journal of Sedimentological Society of Japan* **72**, 13–25 (in Japanese with English abstract).
- Yamada, M., Fujino, S., Goff, J., Chagué-Goff, C., 2016a. Large-scale erosion and overbank deposition caused by the July 2013 flood of the Abu River, Yamaguchi City, Japan. *Island Arc* **25**, 386–399.
- Yamada, M., Fujino, S., Goto, K., 2014. Deposition of sediments of diverse sizes by the 2011 Tohoku-oki tsunami at Miyako City, Japan. *Marine Geology* **358**, 67–78.
- Yamada, K., Takemura, K., Kuwae, M., Ikehara, K., Yamamoto, M., 2016b. Basin filling related to the Philippine Sea Plate motion in Beppu Bay, southwest Japan. *Journal of Asian Earth Science* **117**, 13–22.
- Yokoyama, T., Danhara, T., Yamashita, T., 1986. A new refractometer for volcanic glass. *The Quaternary Research* **25**, 21–30 (in Japanese with English abstract).
- Yokoyama, Y., Nakada, M., Maeda, M., Nagaoka, S., Okuno, J., Matsumoto, E., Sato, H., Matsushima, Y., 1996. Holocene sea-level change and hydro-isostasy along the west coast of Kyushu, Japan. *Palaeogeography, Palaeoclimatology, Palaeoecology* **123**, 29–47.
- Yusa, Y., Takemura, K., Kitaoka, K., Kamiyama, K., Horie, S., Nakagawa, I., Kobayashi, Y., Kubotera, A., Sudo, Y., Ikawa, T., Asada, M., 1992. Subsurface structure of Beppu Bay (Kyushu, Japan) by seismic reflection and gravity survey. *Journal of the Seismological Society of Japan* **45**, 199–212 (in Japanese with English abstract).